Systematic study of the phase behavior of *f*-block oxides irradiated with swift heavy ions

by

Cameron Lee Tracy

A dissertation submitted in partial fulfillment
of the requirements for the degree of
Doctor of Philosophy
(Materials Science and Engineering)
in the University of Michigan
2015

Doctoral Committee:

Professor Rodney C. Ewing, Chair
Professor Udo Becker
Assistant Professor Maik K. Lang, University of Tennessee, Knoxville
Professor Steven M. Yalisove

Acknowledgements

The research described in this dissertation was carried out in collaboration with Maik Lang, John McLain Pray, Fuxiang Zhang, Jiaming Zhang, Christina Trautmann, Daniel Severin, Markus Bender, Vladimir Skuratov, Changyong Park, Dmitry Popov, Zhongwu Wang, and Rodney Ewing. I thank my advisor, Rodney Ewing, for scientific and professional guidance. I am grateful to committee members Udo Becker, Maik Lang, and Steven Yalisove for their valuable insight and comments, as well as for their contributions to a number of collaborative research efforts. I am also grateful for the help given to me by the many colleagues with whom I have worked, including Sulgiye Park, Raul Palomares, Ke Yuan, Sandra Taylor, Alex Cusick, Zhongrui Li, Anton Romanenko, Christian Hubert, Dylan Rittman, Katlyn Turner, Jacob Shamblin, Brandon Perlov, Marcel Toulemonde, Siegfried Klaumünzer, Erik Luther, Phi Thanh, and Joanna Groza. Finally, I thank my parents, Rosemarie Tracy and Robert Tracy, for their support, along with Justin Tracy and Sarah Moir.

This work was supported by the Energy Frontier Research Center *Materials Science of Actinides* funded by the U.S. Department of Energy, Office of Science, Office of Basic Energy Sciences (DE-SC0001089). This material is based upon work supported by the National Science Foundation Graduate Research Fellowship Program under Grant No. DGE-1256260. Any opinions, findings, and conclusions or recommendations expressed in this material are those of the author and do not necessarily reflect the views of the National Science Foundation. The use of the National Synchrotron Light Source at X17C station is supported by NSF COMPRES EAR01-35554 and by US-DOE contract DE-AC02- 10886. Portions of this work were

performed at HPCAT (Sector 16), Advanced Photon Source (APS), Argonne National Laboratory. HPCAT operations are supported by DOE-NNSA under Award No. DE-NA0001974 and DOE-BES under Award No. DE-FG02-99ER45775, with partial instrumentation funding by NSF. This research used resources of the Advanced Photon Source, a U.S. Department of Energy (DOE) Office of Science User Facility operated for the DOE Office of Science by Argonne National Laboratory under Contract No. DE-AC02-06CH11357. HPCAT beamtime was granted by the Cargnegie/DOE Alliance Center (CDAC). This work is based upon data collected at the Cornell High Energy Synchrotron Source (CHESS), which is supported by the National Science Foundation and the National Institutes of Health/National Institute of General Medical Sciences under NSF award DMR-0936384. TEM instrumentation at the Electron Microbeam Analysis Laboratory at the University of Michigan is supported by NSF grants DMR-9871177 and DMR-0723032.

Table of Contents

List of Figures

Abstract

Particles with specific energies of approximately 1 MeV/u or greater interact with matter primarily through the excitation of electrons. Swift heavy ions, with high masses and velocities in this electronic excitation regime, are encountered by materials in the form of nuclear fission fragments, cosmic rays, and ion accelerator beams. The dense ionization resulting from ion-solid interactions in this regime can produce diverse, material-dependent structural and chemical modifications in insulators. This dissertation reports investigation of swift heavy ion-induced phase and valence modifications to oxides of the *f*-block (lanthanide and actinide) elements. Dependence of these modifications on the variations in ionic radius (due to the lanthanide/actinide contraction) and accessible oxidation states (due to the effects of *f*-orbital localization) characteristic of the elements in this system is discussed.

Lanthanides typically exhibit a single stable, trivalent oxidation state, such that they form sesquioxides. The phase systematics of these compounds varies across the lanthanide series due to the influence of lanthanide ionic radius on phase stability. In response to swift heavy ion irradiation, a number of transformations to polymorphic and non-equilibrium phases were observed. These transformations were caused by atomic displacement and point defect formation during relaxation of an irradiation-induced electron-hole plasma, such that their composition-dependence could be attributed to the influence of cation size on the collective atomic reorganization mechanisms associated with phase transformations.

In contrast to the lanthanides, most of which are chemically uniform, the actinide elements have more itinerant *f*-electrons and are typically multivalent. Swift heavy ion irradiation of several actinide and lanthanide dioxides resulted in no phase transformations, but caused cation valence reduction in those materials incorporating cations with stable trivalent oxidation states. Coupling between these chemical modifications and structural distortions, due to associated changes in the ionic radii and bonding of cations, were observed. In *f*-block trioxides, this valence reduction caused changes in stoichiometry, with accompanying redox-coupled phase transformations.

Ternary lanthanide stannate complex oxides exhibited both amorphization and disordering in response to swift heavy ion irradiation. Their susceptibility to irradiation-induced amorphization decreased with the ionic radius of the constituent lanthanide cation. Compounds that were resistant to amorphization instead exhibited disordering in the form of mixing of the two cations (Ln and Sn) onto a single sublattice, via cation antisite formation.

Chapter 1

Introduction

1.1 Energy deposition by swift heavy ions

Heavy ions of high velocity, known as swift heavy ions and possessing specific energies above ~1 MeV/u, interact with insulating materials by exciting nearby core and valence electrons to the conduction band [1]. As they deposit energy to a target material in this manner, the energy of the ion is reduced, as is its velocity, in a process known as electronic stopping. The energy loss of a swift heavy ions as it traverses condensed matter was first modelled by Bethe [2] and is expressed by the equation:

$$-\frac{dE}{dx} = \left(\frac{4\pi}{m_e c^2}\right)\left(\frac{nz^2}{\beta^2}\right)\left(\frac{e^2}{4\pi\varepsilon_0}\right)\left[\ln\left(\frac{2m_e c^2\beta^2}{I(1-\beta^2)}\right) - \beta^2\right] \qquad \text{(Eq. 1)}$$

where dE/dx is the linear electronic energy loss of the ion, m_e is the electron rest mass, c is the speed of light, n is the target electron number density, z is the particle charge, β = ion velocity/c, e is the charge of an electron, and I is the mean ionization potential of the target material. From this equation, it is seen that below a certain ion specific energy (*i.e.* once the ion velocity and β drop below a certain value) the linear electronic energy loss begins to decrease. Concomitantly, the cross section for elastic collisions of the ion with atomic nuclei increases, reaching a maximum at ion specific energies of around ~1 keV/u. Thus, the energy deposited to a material and the dominant mechanism through which it is deposited, varies as the ion is slowed (*i.e.* with increasing penetration depth into a target material). This variation in energy loss with ion energy is illustrated schematically in Figure 1.

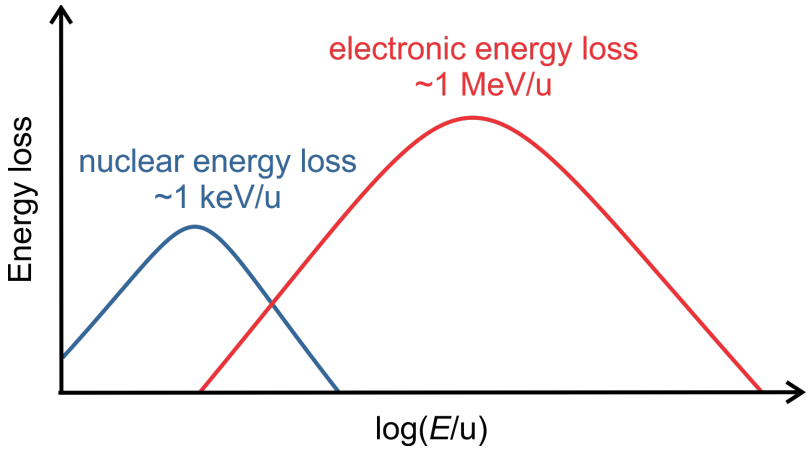

Figure 1: A schematic representation of ion energy loss to a material as a function of ion specific energy, which is proportional to ion velocity. At high specific energy, the electronic energy loss (corresponding to ionization of the target) of a swift heavy ion is typically several orders of magnitude higher than the nuclear energy loss (corresponding to elastic collisions between nuclei). At low specific energies, the reverse holds true. This figure is adapted from [3].

Ions of high velocity deposit the majority of their energy to materials via electronic energy loss. The resulting dense electronic excitation within the ion-solid interaction volume occurs over a few femtoseconds and produces a cylindrical region along the path of the energetic ion, typically hundreds of nanometers in diameter, within which a high temperature electron-hole plasma coexists with a relatively low temperature solid comprised of ionized atoms [1,4,5]. Resulting electron temperatures near the core of this cylindrical region, generally within a few nanometers of the ion path, are ~10^4 K, such that the state of this ion-solid interaction volume can be considered warm dense matter [6,7]. The excitation of electrons from bonding valence orbitals to antibonding conduction band orbitals modifies atomic interactions and weakens bonds. After thermalization of this electron cascade, electron-hole recombination moves the electronic and atomic subsystems towards equilibrium. There are various processes through which energy is exchanged between charge carriers, during thermalization, and from charge carriers to the atomic subsystem, during relaxation of the electron cascade to an equilibrium state. These mechanisms are shown schematically in Figure 2.

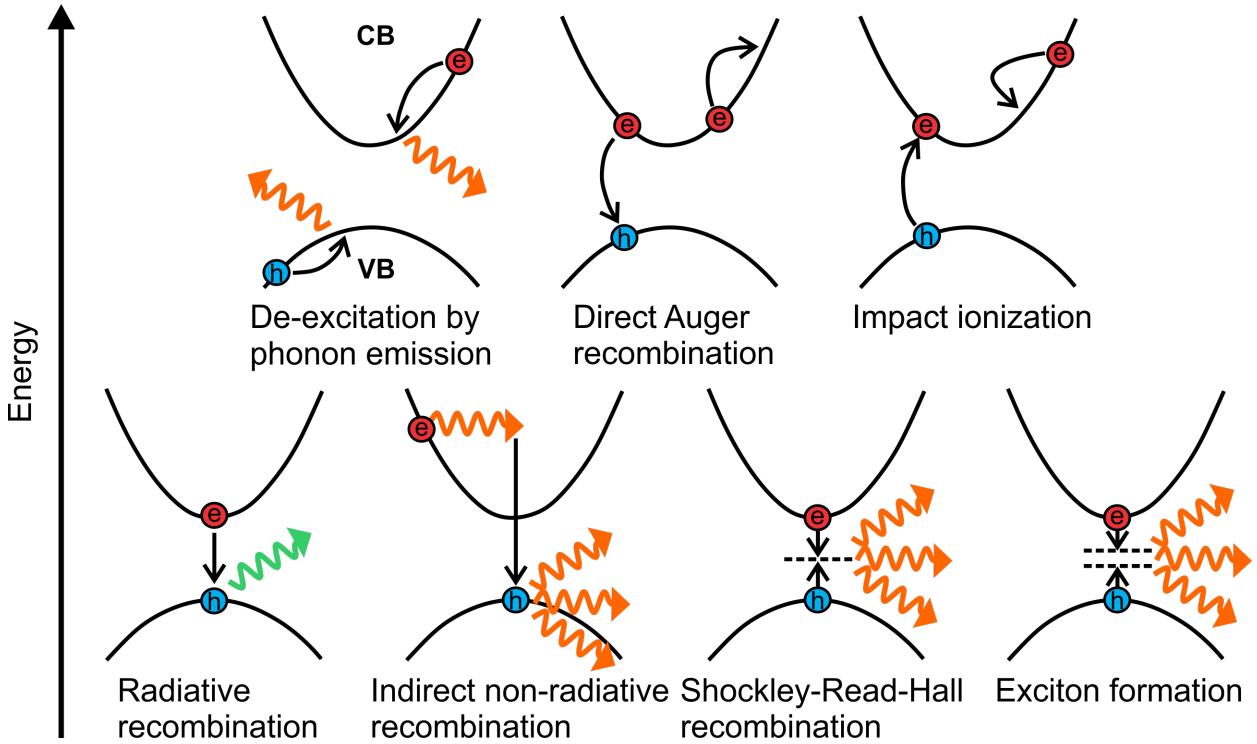

Figure 2: A schematic diagram of various process through which an excited electron-hole plasma thermalizes and relaxes to the bottom of the conduction band (upper row), as well as mechanisms for the recombination of excited electrons with holes and their relaxation to mid-band states (bottom row). Orange arrows represent emitted phonons, while green arrows represent emitted photons. The extent to which each process contributes to energy transfer is material-specific. This figure is adapted from [4,5].

The precise mechanisms through which energy transfer from the electronic subsystem to the atomic subsystem induces material modifications are not well understood. The fastest process that can cause excitation of the atomic subsystem is the modification of interatomic forces due to the excitation of electrons to antibonding orbitals. This changes the potential energy surface that governs the spatial arrangement of atoms, and can lead to atomic displacement [1,5,8,9]. For sufficiently high densities of electronic excitation (promotion of ~10% of electrons to the conduction band in semiconductors [8,9]), nonthermal melting can be induced, in which sufficient kinetic energy is deposited to the atoms to cause a complete loss of local crystallinity. At lower electronic excitation densities, other phase transformations might be induced [5,10].

This process, which takes place on the order of 100 fs in Si [8], for example, is illustrated in Figure 3.

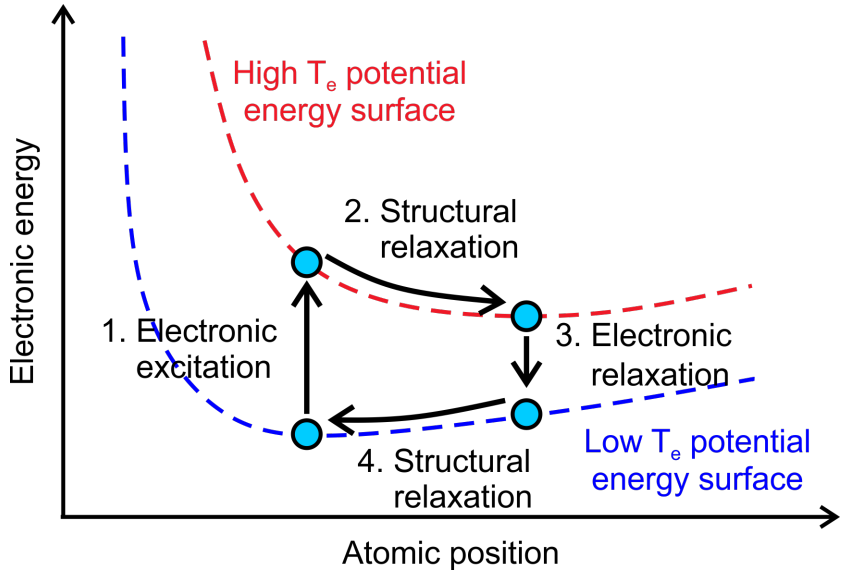

Figure 3: A schematic representation of the atomic transport induced by changes to the potential energy landscape of a material associated with the excitation of electrons from bonding orbitals to antibonding orbitals. When the interatomic forces are modified in this way, atomic motion results to minimize the lattice energy of a material. This process typically occurs on the order of 100 fs. If electrons relax to their initial distribution through recombination with holes, the atomic subsystem will be driven towards its initial spatial configuration. This figure is adapted from [5,10].

Energy transfer to the atomic subsystem also occurs during electron-hole recombination. Many of the charge carrier relaxation and recombination processes involve the emission of phonons (*i.e.* electron-phonon coupling), which involve atomic motion and can induce atomic displacements (see Figure 2). For example, the decay of self-trapped excitons produced following electronic excitation is known to produce Frenkel pairs in some materials [3]. Because these phonon emission processes are largely confined to a nanometric region along the ion path, they generate a thermal spike, which can further modify the structure of a material through thermally induced phase transformations, including melting [5]. Typically, energy is transferred by phonon emission from the excited electron-hole cascade to the atomic subsystem few

picoseconds after ion impact, such that the timescales associated with these mechanisms for modification of the atomic structure are longer than those of the nonthermal processes described above.

The transfer of energy to the atoms comprising a material is followed by quenching of the affected volume on the order of 10 ps [1]. This rapid relaxation to ambient conditions places kinetic constraints on the recovery of a material to its initial state, such that structural modifications or irradiation-induced "damage" are often retained in a metastable state following the diffusion of deposited energy into the matrix surrounding the ion-solid interaction region. Thus, the highly transient, nanometric energy deposition associated with swift heavy ion irradiation can produce unique structural changes in insulating materials, including the formation of defects [11,12], polymorphic phase transformations [13,14], amorphization [15,16], chemical decomposition [17,18], and irreversible deformations [19,20]. The transfer of energy from a swift heavy ion to a material, the transfer of energy from the material's electronic subsystem to its atomic subsystem, and the resulting material modifications are summarized in Figure 4, along with the associated timescales.

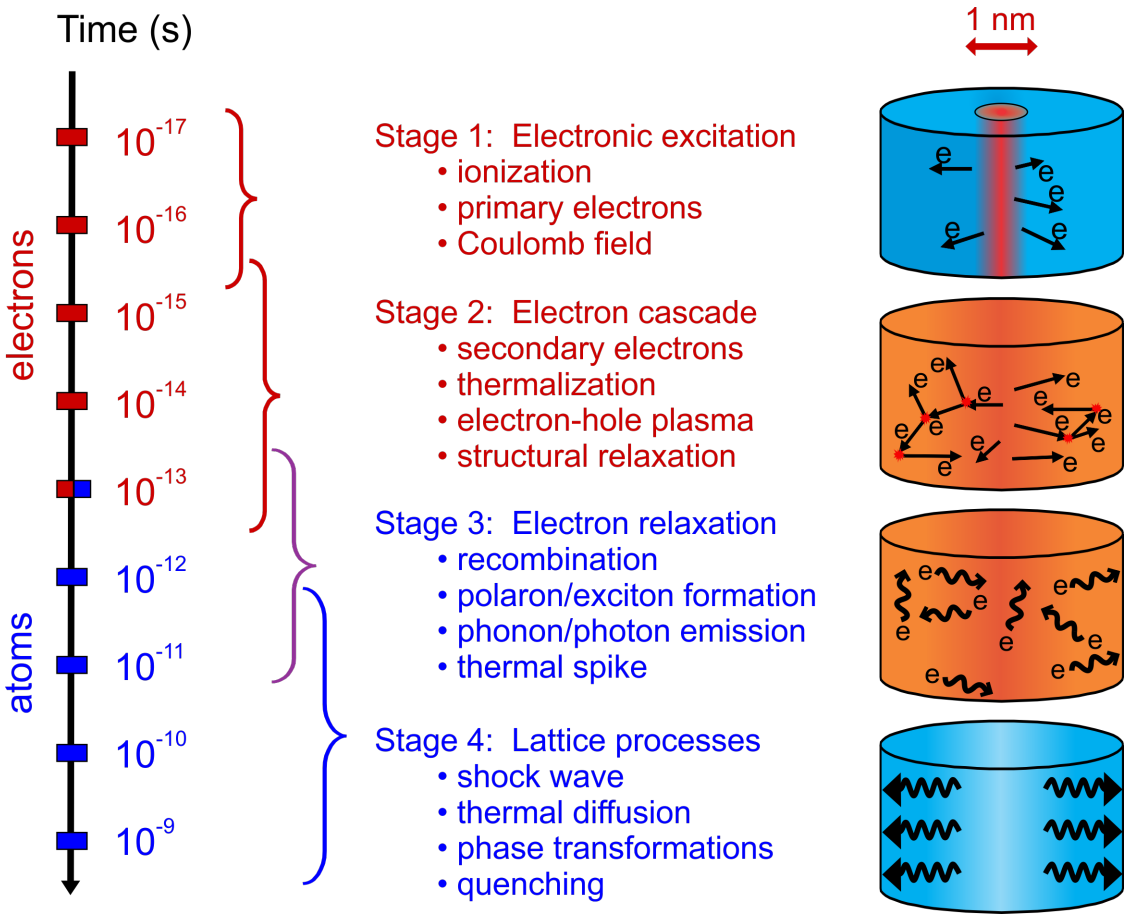

Figure 4: A summary of the excitation and relaxation processes induced by swift heavy ion irradiation of a material. Wavy black lines represent phonons emitted during electron-hole recombination. This figure is adapted from [21].

Tolerance of a material to swift heavy ion irradiation, defined as the ability of a material to retain its initial electronic configuration and atomic structure following irradiation, is strongly material-dependent. For example, many metals are highly radiation tolerant, while many insulators are susceptible to radiation-induced phase transformations [1,15,22]. However, some metals can be amorphized by swift heavy ions [23–26], while some oxides retain their long-range crystallinity under similar irradiation conditions [18,27–33]. Thus, identification of the mechanisms controlling the accumulation of swift heavy ion irradiation-induced damage in materials and the materials properties that govern these mechanisms is of significant interest.

1.2 Swift heavy ion tracks

Swift heavy ions induce electronic excitation-driven material modification along the majority of their paths. Only at the end of path region, when most of the ions energy has been deposited to the material and it has slowed considerably, does nuclear stopping become significant. Figure 5 shows representative energy loss data as a function of the penetration depth of a 2.2 GeV Au ion in ThO_2, calculated using the SRIM code [34]. As shown by this data, the length of a swift heavy ion's path is typically on the order of 10 μm, much larger than the radial distance from the ion path center within which it deposits most of its energy. Thus, the interaction of a swift heavy ion with a radiation sensitive material results in the formation of a cylidrical ion track of high aspect ratio, within which the target material is modified.

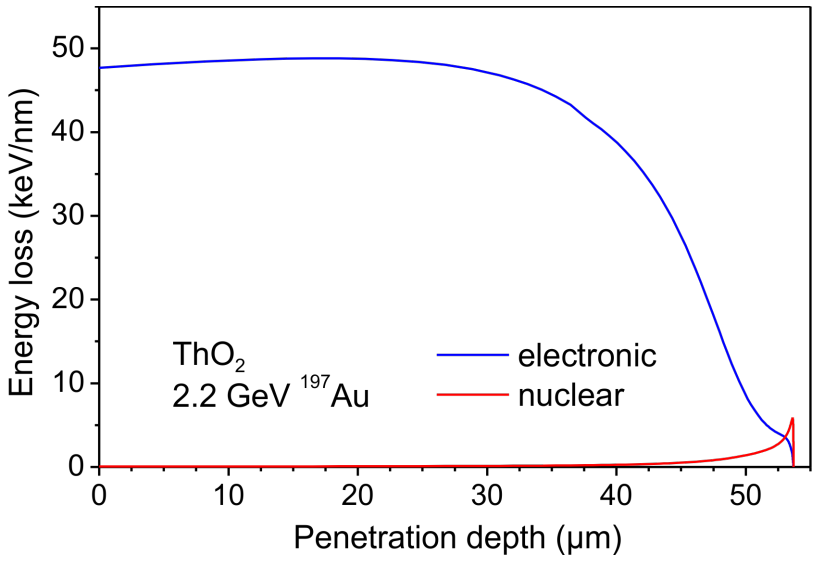

Figure 5: The electronic and nuclear energy loss of a 2.2 GeV Au ion as it traverses a dense ThO_2 solid. Only for the last few micrometers of the ion's path is nuclear energy loss of the same order of magnitude as electronic energy loss. The total penetration depth of the ion is several orders of magnitude larger than the distance from the ion path center within which it deposits the majority of its energy.

The specific modifications that occur within such tracks and are quenched to ambient conditions are material-dependent, ranging from, for example, an increase in point defect concentration to the adoption of an amorphous structure. Figure 6 shows representative

transmission electron microscopy (TEM) images of ion tracks in $Gd_2Ti_xZr_{2-x}O_7$ compounds, which exhibit dramatic changes in track size and morphology with composition [35]. As shown here, tracks can consist of only a single phase or can be highly heterogeneous, with multiple phases coexisting in the cylindrical modified region. Furthermore, depending on the material studied and the mass and energy of the ion with which irradiation is performed, tracks can vary from long, continuous cylinders, as shown in Figure 6, to discontinuous, discrete regions of damage distributed along the ion path [36].

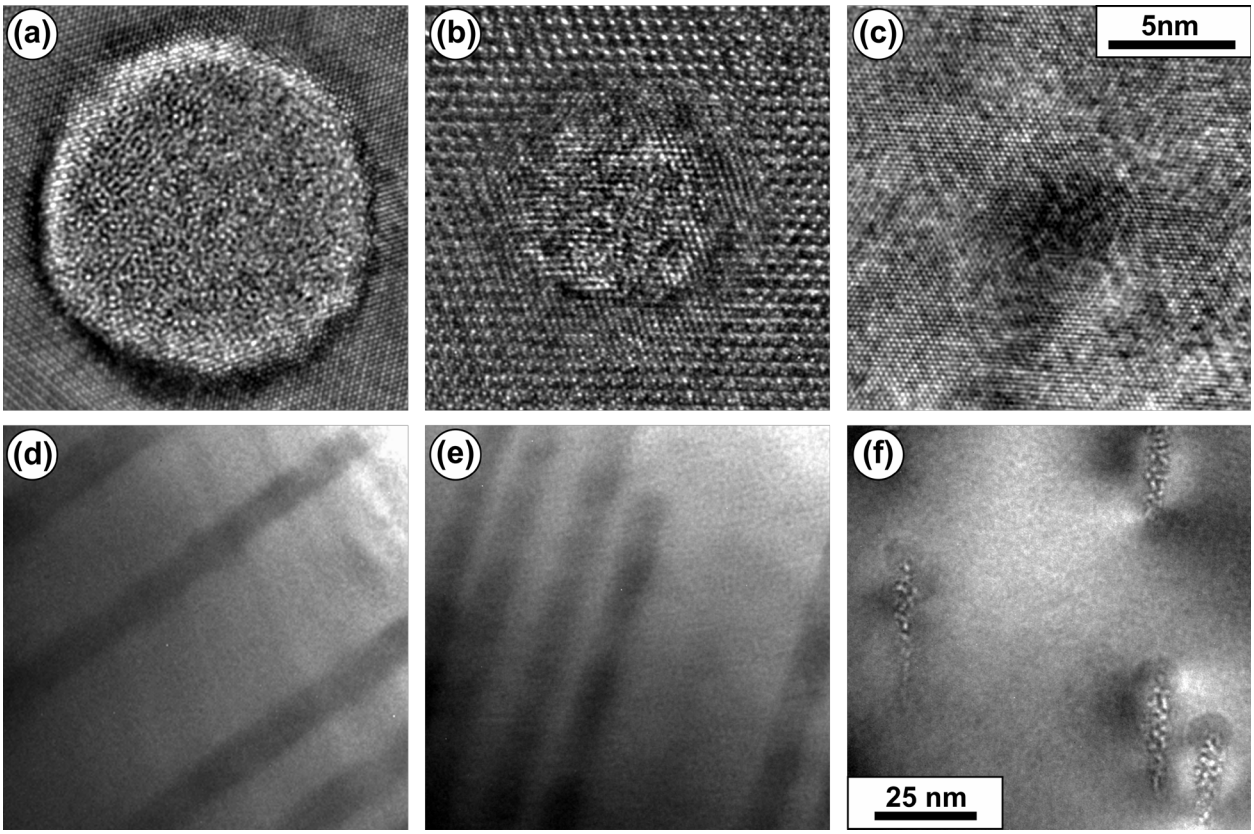

Figure 6: High-resolution TEM micrographs of ion tracks formed in $Gd_2Ti_2O_7$ (a,d), Gd_2TiZrO_7 (b,e), and $Gd_2Zr_2O_7$ (c,f) by irradiation with 2.2 GeV Au ions. The top row (a-c) shows high-resolution TEM images of tracks imaged parallel to the ion beam path, emphasizing the material-dependence of the modifications associated with the interior of an ion track. Tracks in $Gd_2Ti_2O_7$ (a) consist primarily of amorphous material, while tracks in $Gd_2Zr_2O_7$ (c) consist of a disordered crystalline phase and tracks in Gd_2TiZrO_7 (b) consist of a mixture of these two phases. The bottom row (d-f) shows tracks imaged perpendicular to the ion path direction, emphasizing their high aspect ratios. This figure is adapted from [35].

1.3 Sources of swift heavy ions

Interest in the behavior of materials irradiated with swift heavy ions began in the early 1940s, when Wigner first recognized the potential influence of the exposure of nuclear fuels to energetic fission fragments on the performance of these components in nuclear energy systems [37]. These heavy nuclear fragments are produced during the fission of actinide elements and possess masses in the range $m \approx$ 90-160 u and energies in the range $E \approx$ 60-120 MeV, such that they can be considered swift heavy ions [38]. Additionally, alpha particles emitted during the decay of some radioactive isotopes, which are helium nuclei with initial energies around 5 MeV, have specific energies in the electronic energy loss regime, such that their effects are similar to those of swift heavy ions. Fission fragment tracks in the nuclear fuel UO_2 were directly observed using TEM in 1960 by Noggle and Stiegler [39], only a few years after the first observation of ion tracks in uranium oxalate [40], although little was known about their in-track structure at this time. Since then, it has been demonstrated that this fission fragment radiation damage has a significant effect on the performance of nuclear fuels, degrading critical materials properties such as thermal conductivity [41]. Additionally, fission fragment irradiation has been identified as a likely cause of the problematic "rim effect" in nuclear fuels wherein the outer layer of the pellets, where fission rates are highest, exhibit high porosity and grain polygonization at high fuel burn-ups, enhancing fission gas release [33,42,43].

Shortly after the first observation of fission fragment-induced swift heavy ion tracks, numerous groups began to investigate track formation in a variety of compounds via exposure of these materials to fission fragments [44–49]. Among these materials were a number of minerals, mainly of the mica group [47,49,50]. In 1963, Price and Walker identified similar ion tracks in natural samples of mica, attributing them to the spontaneous fission of uranium impurities [50].

Realizing that the concentration of tracks in a mineral is thus a function of its age, they showed that accurate mineral age determinations could be made by the counting of ion tracks using microscopy. Furthermore, they concluded that tracks shrink in size when minerals are exposed to temperatures above ~300 °C, such that their observation can yield information about the thermal history of geological materials. Subsequently, fission track dating techniques were developed for various uranium-bearing minerals (*e.g.* apatite, zircon, and titanite), becoming a valuable technique for thermochronology in the geological sciences [51,52]. Exposure to fission fragments and alpha particles can also induce bulk changes in the structure of minerals, rendering them amorphous after long exposure times, making an understanding of their effects important for mineralogical investigations [53].

In addition to fission fragments, swift heavy ions are encountered by materials in the form of cosmic rays. These particles can have energies greater than 1 EeV (10^{18} eV) [54] and very high masses, including transuranic nuclei [55]. Their source is an area of ongoing study. They may originate via particle emission from the atmospheres of stars, or from interstellar gases, and are likely accelerated by supernova shock waves [56]. Cosmic-ray induced ion tracks were first observed by Maurette *et al.* in 1964 [57], in crystals of olivine recovered from meteorites. Shortly thereafter, Fleischer *et al.* [58] identified heavy ions as the source of these tracks. Analysis of ion tracks in mineral samples recovered from meteorites has proven useful for characterization of cosmic rays, particularly their elemental composition which can be derived from measurements of ion track dimensions [59]. Phosphate glasses are also used as artificial detectors in studies of cosmic rays composition, using similar track analysis techniques [56,60]. Such studies help to constrain potential sources of galactic cosmic rays. Material modification by cosmic ray swift heavy ions is of further astrophysical interest due to its effects on the properties

of silicate interstellar dust, which controls the catalysis of gas-phase molecules in the early stages of planet and star formation [61,62]. Finally, exposure to cosmic ray irradiation can adversely affect the performance of microelectronics on spacecraft [63] and of biological materials [64], such that it is an important consideration is space exploration.

Most recently, heavy ion accelerators have been developed for the controlled production of swift heavy ions [65]. Advantages of these ion beams for materials modification include precise control of ion mass and velocity, in addition to the ability to focus, collimate, and raster the beams. Facilities dedicated to materials research using heavy ion accelerators currently operate at, for example, the GSI Helmholtz Centre for Heavy Ion Research in Darmstadt, Germany, the GANIL Large Heavy Ion National Accelerator in Caen, France, the Joint Institute for Nuclear Research in Dubna, Russia, and the Institute of Modern Physics in Lanzhou, China. In addition to simulation of the effects of fission fragment and cosmic ray irradiation, swift heavy ion beams have found use in, for example, the engineering of nanostructures [66–70] and the tailoring of optoelectronic materials properties [71–74]. The highly transient, nanometric deposition of large amounts of energy to the electronic subsystems of materials makes swift heavy ion irradiation a useful method for inducing modifications of the structures of materials that cannot be achieved using conventional processing techniques.

1.4 *f*-block oxides

The responses of oxides of the *f*-block elements (lanthanides, La-Lu, and actinides, Ac-Lr) to irradiation with swift heavy ions are of particular importance due to their prevalence in nuclear applications and their unique phase systematics. This system includes the light actinide dioxides, which comprise the majority of current and proposed nuclear fuel materials (*i.e.* ThO_2, UO_2, and PuO_2). Oxides of the heavier, transuranic actinides, such as Np, Pu, Am, and Cm, are

major components of nuclear wastes and account for most of the long-term radiotoxicity and decay heat of spent nuclear fuel [75]. Minerals which are influenced by fission fragment and alpha particle irradiation are typically actinide-bearing oxides [53]. Oxides of elements of the lanthanide series also have applications in nuclear energy technologies, most commonly as neutron absorber additives to nuclear fuels [76–78]. They can also be used as surrogates for actinide materials in experimental investigations due to their similar structural, chemical, and thermophysical properties, alleviating many of the difficulties associated with the study of radioactive materials. Finally, the potential for modification of the properties of lanthanide oxides and the production of new phases is of technological interest, given the diverse applications of these materials. They find use in, for example, catalysis [79,80], gas sensing [81], high- κ dielectrics [82,83], nanoparticles for biomedical imaging [84], materials for high-power and ultrafast lasers [85,86], and scintillators for the detection of ionizing radiation [87,88].

f-block elements have unique crystal chemistry due to the presence of *f*-orbitals, which are filled across the lanthanide (4*f*) and actinide (5*f*) series. *f*-electrons are typically highly localized, resulting in minimal participation in bonding [89]. For this reason, most *f*-block elements are chemically uniform, as the addition of *f*-electrons does not influence bonding. The trivalent oxidation state is most common in this system. For example, all lanthanide elements adopt a stable trivalent state and an associated sesquioxides compound, although elements with nearly empty of nearly half full *f*-shells (Ce, Pr, and Tb) also adopt stable tetravalent states, while those with nearly half full or nearly full *f*-shells (Eu and Yb) adopt divalent states, although divalent Yb is rare [90,91]. Somewhat different behavior is found in the actinides. Those heavier than Pu possess localized *f*-orbitals similar to the lanthanides, although many can adopt tetravalent oxidation states in addition to trivalent [90]. Significant deviation in this valence

stability exists in the light actinides (Th-Pu), which have more itinerant 5*f* electrons which can hybridize strongly and participate in bonding [89]. This leads to more variability in the oxide stoichiometries accessible to these elements. The most stable oxidation states adopted by the *f*-block elements as binary oxides [90] are shown in Figure 7. These phase systematics, which allow for isolation of the effects of ionic radius and valence stability on swift heavy ion-induced materials modifications, make the *f*-block oxides an ideal system for the study of mechanisms of irradiation-induced damage accumulation.

f^0	f^1	f^2	f^3	f^4	f^5	f^6	f^7	f^8	f^9	f^{10}	f^{11}	f^{12}	f^{13}	f^{14}
La 3+	**Ce** 3+ 4+	**Pr** 3+ 4+	**Nd** 3+	**Pm** 3+	**Sm** 3+	**Eu** 2+ 3+	**Gd** 3+	**Tb** 3+ 4+	**Dy** 3+	**Ho** 3+	**Er** 3+	**Tm** 3+	**Yb** 3+	**Lu** 3+
Ac 3+	**Th** 4+	**Pa** 4+ 5+	**U** 4+ 5+ 6+	**Np** 4+ 5+	**Pu** 3+ 4+ 5+	**Am** 3+ 4+	**Cm** 3+ 4+	**Bk** 3+ 4+	**Cf** 3+ 4+	**Es** 3+	**Fm** ?	**Md** ?	**No** ?	**Lr** ?

Figure 7: The *f*-block of the periodic table, with the nominal *f*-orbital occupancy of each column (4*f* for lanthanides and 5*f* for actinides) indicated in blue, along with the most common oxidation states exhibited in oxides. The lanthanides show relatively uniform valence stability, with all elements adopting a trivalent state. The actinides, which have more itinerant *f*-orbitals, deviate from this uniformity. Insufficient experimental data is available on oxides of the heaviest actinides, Fm-Lr.

For those elements with relatively uniform stable electronic configurations, the main determinant of crystal chemistry is the ionic radius. *f*-electrons provide poor screening of nuclear charge, so the increasing nuclear charge across both series is accompanied by contraction of the ions. Thus, the phase systematics of the *f*-block oxides tend to vary gradually across the lanthanide and actinide series, with the exception of the light actinides, for which their oxidation state variability plays a significant role in phase stability. The most common structures of the *f*-block oxides are the bixbyite-type for trivalent cations and the fluorite-type for tetravalent cations, named after the minerals $(Mn,Fe)_2O_3$ and CaF_2, respectively [90]. Both are shown in

Figure 8. These structures are very similar, such that the sesquioxide bixbyite structure can be considered a derivative of the dioxide fluorite structure with ordered constitutional anion vacancies to preserve stoichiometry, along with slight distortion of the cation and anions sublattices due to relaxation towards these vacancies. In combination with transition metals, these elements can form a variety of complex oxides. Those with pyrochlore-type structures, shown in Figure 8, have received particular attention due to potential applications as, for example, nuclear wasteforms [92]. This structure type is also a derivative of the fluorite structure, distinguished by the ordering of two elements on the cation sublattice and the presence of constitutional vacancies on the anion sublattice, accompanied by slight distortions.

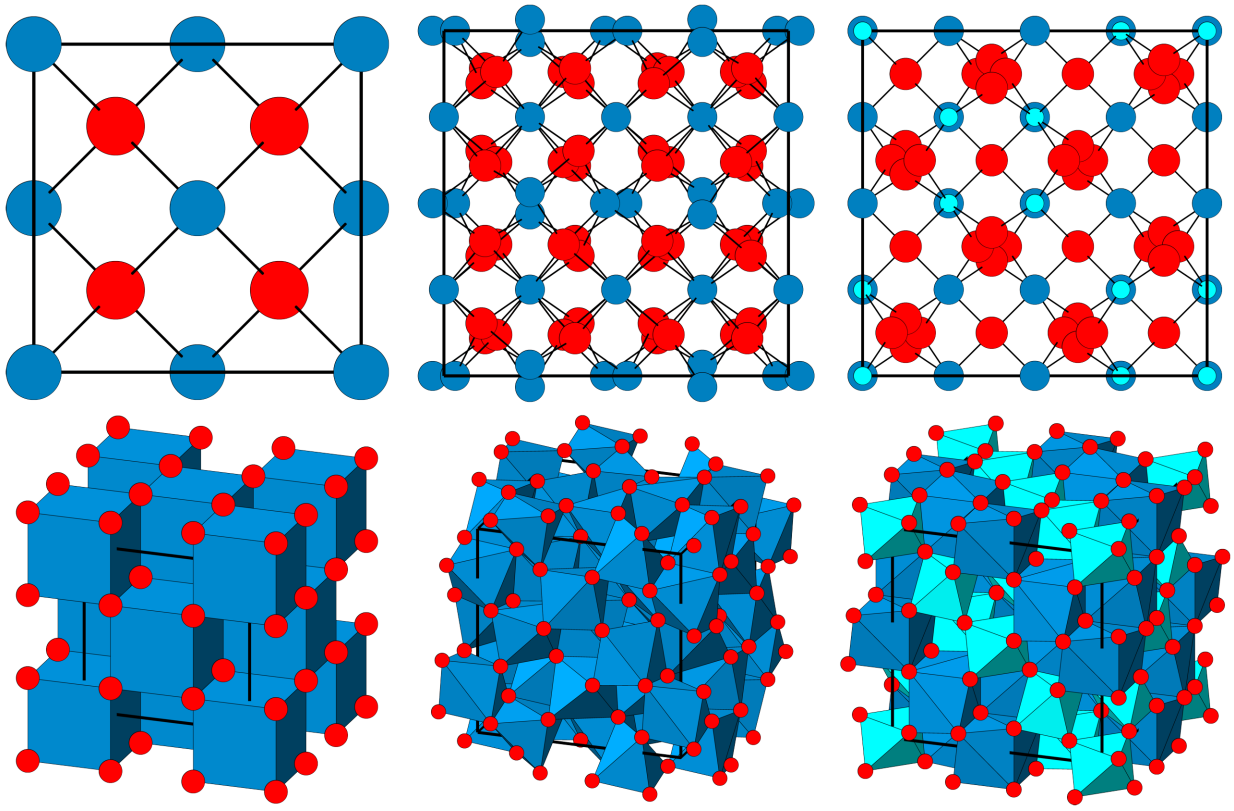

Figure 8: The fluorite (left), bixbyite (center), and pyrochlore (right) unit cells viewed along [100] (top) and in an arbitrary direction (bottom). Blue circles represent cations, blue polyhedra indicate cation coordination, and red circles represent anions. The fluorite structure is typical of AO_2 compounds, the bixbyite structure of A_2O_3 compounds, and the pyrochlore structure of $A_2B_2O_7$ compounds. All three structure-types exhibit a cubic crystal system. The fluorite

structure corresponds to a face-centered cubic cation sublattice with anions occupying the tetrahedral interstices, yielding cubic coordination of cations. The bixbyite structure features a distorted face-centered cubic cation sublattice, which an anion sublattice similar to that of the fluorite structure, yet oxygen-deficient and distorted. Cations are in distorted octahedral coordination in this structure. Its unit cell is comprised of eight fluorite-like cells, such that it can be considered a 2×2×2 supercell derivative of the fluorite structure. The pyrochlore structure is also a 2×2×2 superstructure of the fluorite structure, with one eighth of the anions replaced by vacancies and two cation species on the face-centered cubic sublattice. It exhibits mixed 8-fold scalenohedral and 6-fold distorted octahedral coordination of the A and B cations, respectively.

This dissertation reports the results of three experimental investigations of the structural and chemical effects of swift heavy ion irradiation on various *f*-block oxides. The primary purpose of these studies is to relate compositional trends in radiation response and radiation tolerance to the unique variations in crystal chemistry characteristic of oxides containing *f*-block elements. Chapter 2 explains in detail the experimental methods used in this work, including sample preparation, ion beam irradiation, synchrotron x-ray diffraction and absorption spectroscopy, Raman spectroscopy, and transmission electron microscopy techniques. Chapter 3 details a study of the response of lanthanide sesquioxides to swift heavy ion irradiation, in which the effects of the lanthanide contraction on the radiation response are assessed. Chapter 4 details a study of the response of the redox-active light actinide and lanthanide dioxides to swift heavy ion irradiation, wherein the effects of irradiation-induced redox behavior are isolated and investigated. Finally, Chapter 5 details a study of the response of lanthanide stannate compounds with the pyrochlore structure to swift heavy ion irradiation.

Experiments described in Chapters 2 and 4 were previously reported in [93] and [18] , respectively, while manuscripts corresponding to Chapters 3 and 5 are currently in preparation. All publications resulting from the work described in this dissertation and related work carried out during my graduate studies at the University of Michigan are listed below:

C.L. Tracy, M. Lang, F. Zhang, C. Trautmann, R.C. Ewing. Phase transformations in Ln_2O_3 materials irradiated with swift heavy ions, submitted to *Phys. Rev. B* (2015)

C.L. Tracy, M. Lang, D. Severin, M. Bender, C. Trautmann, R.C. Ewing. Anisotropic expansion and amorphization of Ga_2O_3 irradiated with 946 MeV Au ions, submitted to *Nucl. Instrum. Meth. B* (2015)

F.X. Zhang, **C.L. Tracy**, M.K. Lang, R.C. Ewing. Stability of fluorite-type $La_2Ce_2O_7$ under extreme conditions, submitted to *J. Solid State Chem.* (2015)

C.L. Tracy, M. Lang, F. Zhang, R.I. Palomares, S. Park, R.C. Ewing. Review of recent experimental results on the behavior of oxide nuclear materials in extreme environments, submitted to *Prog. Nucl. Energy* (2015)

M.K. Lang, **C.L. Tracy**, R.I. Palomares, F.X. Zhang, D. Severin, M. Bender, C. Trautmann, C. Park, V. Prakapenka, V.A. Skuratov, R.C. Ewing. Characterization of ion-induced radiation effects in nuclear materials using synchrotron x-ray techniques, *J. Mater. Res.* **30,** 1366 (2015)

D.R. Rittman, **C.L. Tracy**, A.B. Cusick, M.J. Abere, B. Torralva, R.C. Ewing, S.M. Yalisove. Ultrafast laser and swift heavy ion irradiation: Response of Gd_2O_3 and ZrO_2 to intense electronic excitation, *Appl. Phys. Lett.* **106**, 171914 (2015)

S. Park, M. Lang, **C.L. Tracy**, J. Zhang, F. Zhang, C. Trautmann, M.D. Rodriguez, P. Kluth, R.C. Ewing. Response of $Gd_2Ti_2O_7$ and $La_2Ti_2O_7$ to swift-heavy ion irradiation and annealing, *Acta. Mater.* **93**, 1 (2015)

R.I. Palomares, **C.L. Tracy**, F. Zhang, C. Park, D. Popov, C. Trautmann, R.C. Ewing, M. Lang. In situ defect annealing of swift heavy ion irradiated CeO_2 and ThO_2 using synchrotron X-ray diffraction and a hydrothermal diamond anvil cell, *J. Appl. Cryst.* **48**, 711 (2015)

C.L. Tracy, M. Lang, J.M. Pray, F. Zhang, D. Popov, C. Park, C. Trautmann, M. Bender, D. Severin, V.A. Skuratov, R.C Ewing. Redox response of actinide materials to highly-ionizing radiation, *Nat. Commun.* **6**, 6133 (2015)

M. Lang, M. Toulemonde, J. Zhang, F. Zhang, **C.L. Tracy**, J. Lian, Z. Wang, W.J. Weber, D. Severin, M. Bender, C. Trautmann, R.C. Ewing. Swift heavy ion track formation in $Gd_2Zr_{2-x}Ti_xO_7$ pyrochlore: Effect of electronic energy loss, *Nucl. Instrum. Meth. B* **336**, 102 (2014)

F.X. Zhang, M. Lang, **C.L. Tracy**, R.C. Ewing, D.J. Gregg, G.R. Lumpkin. Incorporation of uranium in pyrochlore oxides and pressure-induced phase transitions, *J. Solid State Chem.* **219**, 49 (2014)

C.L. Tracy, J.M. Pray, M. Lang, D. Popov, C. Park, C. Trautmann, R.C. Ewing. Defect accumulation in ThO_2 irradiated with swift heavy ions, *Nucl. Instrum. Meth. B* **326**, 169 (2014)

S. Park, M. Lang, **C.L. Tracy**, J. Zhang, F. Zhang, C. Trautmann, P. Kluth, M.D. Rodriguez, R.C. Ewing. Swift heavy ion irradiation-induced amorphization of $La_2Ti_2O_7$, *Nucl. Instrum. Meth. B* **326**, 145 (2014)

M. Lang, F. Zhang, J. Zhang, **C.L. Tracy**, A.B. Cusick, J. VonEhr, Z. Chen, C. Trautmann, R.C. Ewing. Swift heavy ion-induced phase transformation in Gd_2O_3, *Nucl. Instrum. Meth. B* **326**, 121 (2014)

C.L. Tracy, M. Lang, J. Zhang, F. Zhang, Z. Wang, R.C. Ewing. Structural response of A_2TiO_5 (A = La, Nd, Sm, Gd) to swift heavy ion irradiation, *Acta Mater.* **60**, 4477 (2012)

Chapter 2

Methods for the characterization of swift heavy ion irradiation effects

To date, the majority of post-swift heavy ion irradiation studies of *f*-block oxides have focused exclusively on nuclear fuels and have involved techniques that are generally not suitable for atomic-level characterization. Examples of commonly used techniques include: fluid-gravimetry and porosity measurements (density and swelling analysis), γ-scans and electron-probe microanalysis (EPMA) (fission product/elemental analysis), Raman spectroscopy, and an array of visual inspection methods, such as ceramography, scanning electron microscopy (SEM), bright-field transmission electron microscopy (TEM), and X-ray radiography [94–98]. Due to the radioactivity concerns associated with studies of actinide-bearing materials, many current post-irradiation examination efforts require the use of hot cells and dedicated handling facilities in order to provide sufficient shielding from the radiation, necessarily limiting the analytical methods that can be applied. Although the same limitations are not applicable to studies of the lanthanide oxides, they inhibit efforts for direct comparison of the behavior of lanthanide and actinide materials using consistent methods, as is an objective of the work described in this dissertation. Thus, the research described here necessitated the development and use of experimental techniques suitable for high spatial resolution characterization of radioactive materials. This was achieved by minimizing the amount of material needed for accurate analysis of irradiation-induced modifications, which also minimizes the total radioactivity of the samples studied to levels suitable for routine handling.

High-resolution structural and chemical analysis of microgram quantities of material using x-ray techniques has recently become possible due to the widespread availability of third generation synchrotron sources. In recent years there has been a renewed interest in using synchrotron radiation to characterize actinides and radioactive compounds with several dedicated synchrotron beamlines around the world [99–104], such as the MARS beamline at the French National Synchrotron Facility SOLEIL in Paris, France and the BL-27 beamline at the Photon Factory in Tsukuba, Japan. Still, synchrotron-based studies of irradiated nuclear fuels have been largely limited to dedicated research groups (*e.g.* [99,105–108]) that have overcome the handling and safety issues associated with highly radioactive fuel materials. There are several advantages to the use of synchrotron-based techniques for post-irradiation structural and examination of materials. X-ray scattering of polycrystalline materials can yield measurements that are more statistically reliable than electron microscopy techniques, for example, which limit observations to a very small region of interest. Synchrotron techniques are also flexible in terms of x-ray energy, beam size, and detector selection/configuration, permitting multi-scale (nm-μm) characterization and element-specific spectroscopy. Raman spectroscopy techniques allow for similar control over photon energy and beam size, making this a complementary analysis technique, which can be performed using laboratory-scale instruments.

2.1 Sample preparation and irradiation

The experiments described in this dissertation were performed using polycrystalline powder samples with typical grain sizes on the order of 1 μm. These samples are ideal for analysis by x-ray and visible light scattering and absorption because they allow for the minimization of crystallite orientation effects, allowing for analysis of a nearly randomly-distributed collection of small crystallites. Furthermore, this grain size is large, relative to the

diameters of ion tracks, minimizing the influence of surface effects on the material modifications observed. By comparing the radiation response of these microcrystalline powders to those of nanocrystalline powders of the same structure and composition, these surface effects can be isolated.

To address the experimental difficulties associated with the study of radiotoxic materials, a new sample holder system was designed. Adopted from the small sample handling techniques commonly used for high-pressure materials science experiments [109], microscopic sample chambers were prepared in thin molybdenum foils by drilling several holes of ~100 μm diameter. A tabletop electric-discharge machining device from Hylozoic Micro EDM Systems, equipped with a 100-μm copper wire tip, was used for this drilling (Figure 9). The foil thickness varied from 12.5 μm to 50 μm, and was selected based on the penetration depth of the ion beam used, calculated using the SRIM code [34]. The foil thickness, which determines the sample thickness, was chosen such that all ions would pass completely through the samples, excluding the ion end-or-range region where nuclear energy loss becomes significant and preventing implantation of the ions into the sample materials. For each sample material, the thickest foil that satisfied this sample penetration requirement was used, as thicker samples allow for larger volumes of material to be probed in transmission mode x-ray beam characterization, yielding improved signals and statistics. These sample holders were then cleaned in an ultrasonic bath with acetone. Subsequently, sample powder was placed over the holes and pressed between two steel die-pieces using a hydraulic laboratory press (Carver, Inc.) at 20-30 MPa. Excess sample material was then removed with a sharp scalpel under the microscope to ensure well-defined pellet dimensions of 100 μm in diameter and, depending on the ion energy used during irradiation, 12.5 μm, 25 μm, or 50 μm in thickness. Typically, a sample holder prepared for a given irradiation

fluence consisted of seven small pellets (filled holes). Multiple, identical sample pellets were irradiated to account for loss of material during ion irradiation and sample handling during irradiation, transportation, and characterization. Typically, several sample sets of various materials were irradiated simultaneously on a rectangular molybdenum-foil strip (Figure 10), to ensure identical irradiation conditions, facilitating direct comparison of the irradiation effects. With a typical ion-beam spot size of ~1 cm^2 and appropriate spacing between holders intended for individual fluence steps, three molybdenum strips with pellets could be placed in the ion beam and simultaneously irradiated to the same fluence.

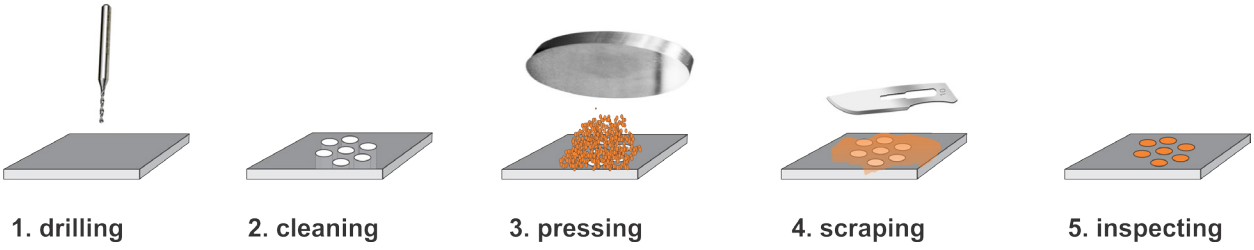

Figure 9: The sample preparation method used in this work, presented in sequence. Microscopic holes (diameter ~100 µm) were drilled into a molybdenum foil of 12.5-50 µm thickness, serving as sample chambers. The sample pellets were then prepared by pressing loose powder into the cleaned holes and scraping off any excess material.

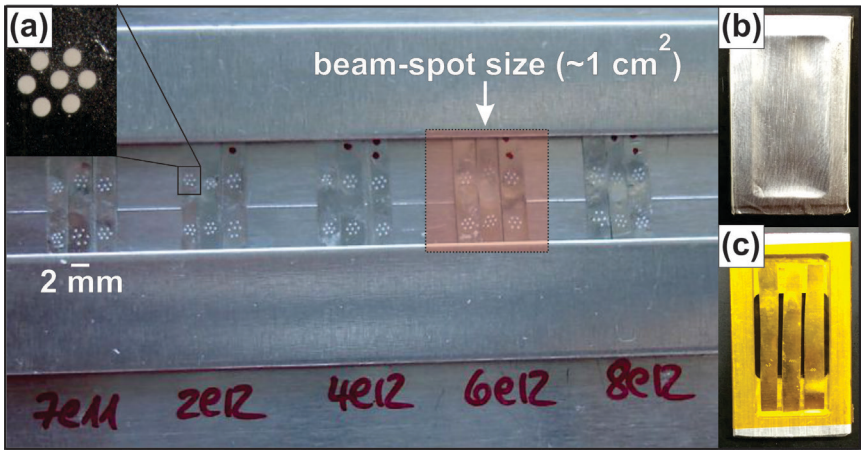

Figure 10: (a) Photograph of the irradiation holders with five sets of samples to be exposed to ion fluences between 7×10^{11} and 8×10^{12} ions/cm^2. Three molybdenum foil strips, each with two sets of seven pellets, were irradiated simultaneously with an ion beam of ~1 cm^2 spot size. The inset displays the 7 symmetrically arranged pellets of the same material (diameter: ~100 µm). To avoid the release of radioactive materials, these foil strips could be attached to small aluminum

frames (area: 1 x 2 cm^2) sealed with (b) 10 μm thick aluminum foil for ion-beam irradiation and (c) 25 μm thick Kapton foil for synchrotron x-ray measurements.

The molybdenum foil strips were directly fixed with double-sided tape onto a larger aluminum frame, serving as a sample strip holder in the irradiation chamber (Figure 10a). Alternatively, when radioactive materials were investigated, the strips were attached in sets of three to smaller aluminum holder frames (Figure 10b,c). The latter procedure allow for complete containment of the samples, achieved through wrapping of individual holders with a thin layer of aluminum foil, for irradiation, or x-ray transparent Kapton foil, for characterization. During irradiation, the thickness of the aluminum cover was taken into account when determining the energy ion the accelerated ions at the irradiated sample surface.

Each set of samples in a holder was homogeneously irradiated with the same ion beam to the desired fluence (see the indicated beam spot size in Figure 10a). Different sets of samples including the same materials were sequentially irradiated to various fluences by moving each holder into the beam. This allowed for the characterization of damage in a specific material as a function of ion fluence. All irradiations were conducted at room temperature, with beam incidence normal to the sample pellet surface. Irradiations experiments were performed at beamlines M2 and HLI of the UNILAC linear accelerator at the GSI Helmholtz Center for Heavy Ion Research in Darmstadt, Germany and at the IC-100 cyclotron at the Joint Institute for Nuclear Research in Dubna, Russia.

2.2 Sample characterization

After irradiation, the samples were analyzed using multiple complementary characterization techniques including x-ray diffraction (XRD), x-ray absorption spectroscopy (XAS), Raman spectroscopy, and transmission electron microscopy (TEM). During irradiation dimensional changes of the pellets (*e.g.* volume reduction due to densification) or fragmentation

often results in sample loss. Thus, sample characterization methods that can probe very small volumes of material were used. Due to the availability of small x-ray, visible light, and electron beam sizes, even minor sample residue at the edge of the drilled hole was sufficient for investigation.

Synchrotron x-ray analysis of irradiated materials was performed at beamlines developed for high-pressure materials research. These instruments provide high-brilliance, hard, highly-focused and collimated x-rays, with spot sizes of less than 25 μm. This allows for characterization of very small, microgram sample pellets without unwanted signal from the molybdenum sample holders. As an example, beamline HPCAT 16 BM-D of the Advanced Photon Source (APS) is used to explain the operational mode of a typical synchrotron high-pressure beamline (Figure 11). The methods described here are representative of those used at all beamlines from which data reported in this dissertation was obtained. The monochromatic x-ray wavelength was selected by a Si (111) double-crystal monochromator operating in pseudo channel-cut mode (typical values: λ = 0.4959 Å or E = 25.000 keV). The incident beam size before the monochromator was 1.5 mm with a beam-slit location of ~42 m from the source. This configuration results in an energy resolution of about $\Delta E/E = 5\times10^{-4}$ at E = 25.000 keV. The downstream x-ray beam behind the monochromator was further focused using a rhodium-coated Kirkpatrick-Baez (KB) type mirror at 1.5 mrad angle (cut-off energy is ~45 keV) in the vertical and horizontal directions. The asymmetry of both focusing mirrors leads to a beam profile at the focal point of about 16 μm × 6 μm in the full width at half maximum (FWHM). The converging incident beam was constrained by a clean-up pinhole of 35 μm in diameter just in front of the sample station to cut out the scattering background from nearby material hit by the x-ray beam. The total intensity on the sample from a focused beam was usually around 5×10^{8} photons/sec.

The structure of irradiated materials were investigated by means of angle-dispersive micro x-ray diffraction (XRD). Debye-Scherrer rings were collected using a MAR345 Image Plate detector (Figure 11) that was typically located 320 mm behind the sample position. The detector geometry and distance from the sample were calibrated using a National Institute of Standards and Technology (NIST) CeO_2 standard powder. The electronic configuration of the irradiated materials was investigated by means of x-ray absorption spectroscopy (XAS). These measurements can be combined with XRD measurements by the beamline's switchable diffraction-absorption setup without losing the sample alignment. The double crystal monochromator is designed for a nearly-fixed-exit configuration (from 6 keV to 60 keV energy) which allows switching from the XRD to the XAS setup by simply moving to the designated absorption edge energy and tweaking the second monochromator crystal to maximize the beam intensity after the clean-up pinhole. The monitor and detector ionization chambers were pneumatically moved into position (Figure 11), and the energy was scanned based on pre-defined tabulated energy points. For these high-energy absorption measurement, the two ionization-chambers were filled with pure Ar gas flowing with a pressure slightly above atmosphere. This switchable micro-XRD-XAS setup is unique in that both techniques can be applied to an identical sample volume to obtain quasi-simultaneous structural and electronic information on irradiated materials, as is required for systematic study the effects of swift heavy ion irradiation on both the atomic structures and the valence states of *f*-block oxides.

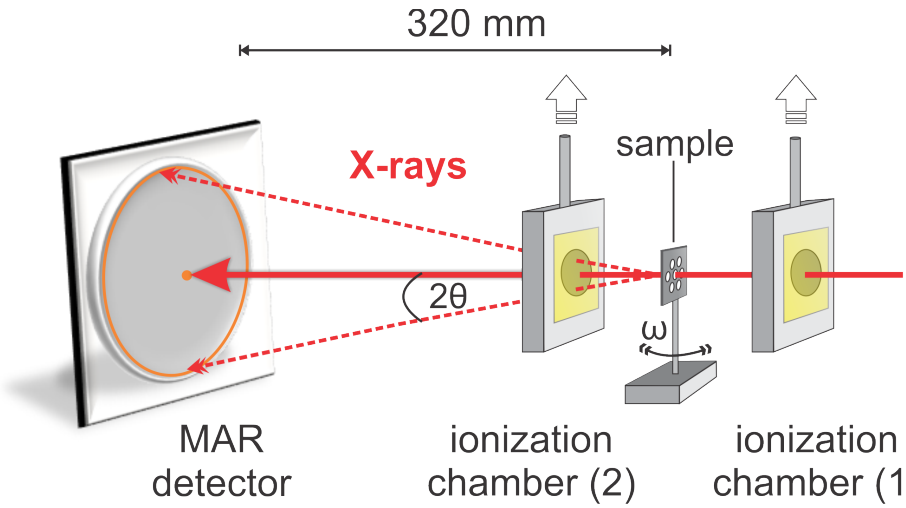

Figure 11: A schematic illustration of beamline HPCAT 16 BM-D at the Advanced Photon Source (APS) of Argonne National Laboratory. The monitor (1) and detector (2) ionization chambers are pneumatically moved into position for x-ray absorption spectroscopy (XAS) measurements, or removed for x-ray diffraction (XRD) experiments using a MAR345 image plate detector. The switchable micro-XRD-XAS setup allows use of the techniques quasi-simultaneously to obtain structural and electronic information within identical sample volumes. The typical sample-detector distance of 320 mm with x-rays of wavelength 0.4959 Å yields a maximum 2θ value of ~30° at the two-dimensional MAR detector. The sample can be rotated along the axis ω for calibration of the detector distance.

The small sample pellets were initially aligned with respect to the x-ray beam with an optical microscope mounted at the beamline. Fine adjustment with accuracy at the µm-level was obtained by scanning the beam horizontally and vertically across the sample and monitoring its intensity with a photodiode (sample stage is moved with respect to stationary x-ray beam). The center position of the sample pellet was located based on the differences in x-ray absorption of the sample and molybdenum sample holder. Molybdenum was specifically chosen for this application based on it significantly different absorption coefficient at the x-ray energies used in these experiments, making it easy to distinguish from the sample through measurements of the transmitted beam intensity. The focused x-ray beam could then be directed to the center of the sample pellet, or any desired location within the sample. As a final step, the sample position with respect to the detector, which is an important parameter for an accurate determination of –

interplanar spacings in the atomic structure, must be adjusted to the previously calibrated distance, to correct for possible errors in the manual mounting of the samples in the x-ray beam. To this end, the sample was moved such that it was aligned with the sample mount axis of rotation around the ω-axis, which is located at precisely the calibrated sample-detector distance, as shown in Figure 11. This was accomplished by repeated horizontal scans of x-ray absorbance at different angles of rotation, ω. Only at the rotation axis were the horizontal scans identical for any given rotation angle and, if they deviated, the sample-detector distance was adjusted by moving the sample relative to the detector. By repeating this procedure several times, the sample position could be determined with an accuracy of ±10 μm.

After exposure of a MAR345 detector to the diffracted x-rays for collection times ranging from seconds to minutes, the resulting diffraction images were integrated in the detector azimuthal direction, yielding 2θ-intensity profiles (diffractograms), with the software Fit2d [110]. These XRD patterns were analyzed by Rietveld refinement [111] to obtain unit-cell parameters, grain sizes, and heterogeneous microstrain values of defect-rich materials, as well as to establish phase fractions resulting from irradiation-induced crystalline-to-crystalline transformations. For example, changes in unit-cell volume are indicated by shifts in the angular positions of diffraction maxima, while changes in grain size or the production of heterogeneous microstrain induce broadening of diffraction peaks [112]. Phase transformations are associated with the attenuation of diffraction maxima corresponding to the initial phase and the growth of new peaks or, in the case of amorphous phases, diffuse scattering bands [113]. In the refinement process, parameters associated with these materials characteristics are iteratively adjusted until a simulated diffraction pattern generated using these parameters achieves a satisfactory fit to the experimental data, based on least-squares methods. Amorphization can be investigated by

applying appropriate peak-fitting procedures for deconvolution of the contribution of the crystalline (sharp diffraction maxima) and amorphous (broad diffuse scattering) sample fractions to the XRD patterns [114].

The XAS spectra collected in these experiments were analyzed for changes in the shape or position of the absorption edges and associated features. Shifts in edge energies can indicate changes in the oxidation state of an element, while changes in pre- or post-edge features are often indicative of changes in the local coordination environment of atoms. Both can be caused by irradiation, with the latter providing information complementary to that of x-ray diffraction analysis, as defect production entails modification of the coordination of both displaced atoms and those adjacent to defect sites. In all cases, comparison of patterns with standards was necessary, due to the difficulties associated with modelling of core electron absorption spectra.

After collection of synchrotron x-ray scattering and absorption data, the molybdenum sample strips were removed from their sealed holders for Raman and TEM analysis. These methods require direct access to the polycrystalline pellets because, unlike the high energy ion and x-ray beams, visible light and electron beams would interact relatively strongly with any sample covering. For the collection of Raman spectra, the samples strips were placed in the visible light beam of a spectrometer, and a translating stage was used for selection of the appropriate sample pellet. The use of an optical microscope in conjunction with the visible light Raman laser allowed for selection of individual pellets, as typical beam spot sizes are on the order of 1 μm. A high degree of disorder in a material, as is often produced by irradiation with swift heavy ions, can yield strong attenuation of signal from Raman-active vibrational modes. Therefore, to achieve suitable statistics, multiple Raman spectra were collected from each sample, and were averaged to yield a single spectrum with minimal noise. Different laser

wavelengths were used for different samples in an attempt to minimize background signal arising from luminescence associated with crystallographic defects. In this way, the Raman data obtained could be used to study changes to the local structure, coordination, and defect characteristics of materials, in a manner complementary to XRD, which yields information on the long-range structure of a material.

For those samples to which it was applied, TEM was the last characterization method performed, as it required removal of the samples from their molybdenum foil holders and grinding of the polycrystals into loose powders. The resulting small crystallites could then be dispersed onto a copper TEM sample grid. Imaging was performed on individual, isolated ion tracks in samples irradiated to relatively low ion fluences. This allowed for accurate determination of track sizes.

Chapter 3

Swift heavy ion irradiation of Ln_2O_3 materials: irradiation-induced phase transformations

Few studies have investigated the behavior of lanthanide sesquioxides, Ln_2O_3, under the extreme energy deposition conditions associated with swift heavy ion irradiation. These compounds find use in diverse applications, as high-κ dielectrics [82,83], nanoparticles for biomedical imaging [84], materials for high-power and ultrafast lasers [85,86], neutron absorbers in nuclear fuels [115], and scintillators for the detection of ionizing radiation [87,88]. Under ambient conditions, most lanthanide sesquioxides adopt a cubic (*Ia*-3) structure characteristic of the mineral bixbyite, $(Fe,Mn)_2O_3$, and known within the Ln_2O_3 phase systematics as the C-type phase (see Figure 8). This structure is shared by Sc_2O_3, Mn_2O_3, Y_2O_3, In_2O_3, and U_2N_3. It is a derivative of the fluorite structure (*Fm*-3*m*), characteristic of all lanthanide and actinide dioxides (LnO_2 and AnO_2), with a unit cell composed of eight fluorite-like subcells [91,116]. Cations occupy 24*d* and 8*b* sites that are close to the cation positions on an ideal fluorite sublattice, forming a distorted face-centered cubic arrangement. Anions occupy 48*e* sites in tetrahedrally-coordinated interstices, while one-fourth of these tetrahedral positions, the 16*c* sites, remain vacant in order to accommodate the deviation in stoichiometry from that of fluorite-structured materials. The anions relax towards these "constitutional vacancies," so called because they are not defects but are rather intrinsic to the C-type structure, producing a distorted, anion-deficient fluorite-structured sublattice.

Two other Ln_2O_3 phases have been observed at ambient conditions: the trigonal A-type (*P*-3*m*1) and the monoclinic B-type (*C*2/*m*) [91,116,117]. The A-type phase forms only for

oxides with lanthanide cations of low atomic number, while the B-type phase is a high-temperature polymorph that forms from oxides with cations near the middle of the lanthanide series, and can be quenched to ambient temperature. Two additional polymorphs, the hexagonal H-type ($P6_3/mmc$) and cubic X-type ($Im\text{-}3m$) have been observed only at high temperature [91,117–119], with the stability of both decreasing across the lanthanide series (*i.e.* with increasing atomic number). The thermal polymorphism of a material in the Ln_2O_3 system is strongly influenced by the ionic radius of its constituent lanthanide element, as illustrated in Figure 12. Because the 4*f* electron shell, which is filled across the series, is highly localized, all lanthanide elements are chemically similar. The poor screening provided by *f*-electrons results in a monotonic decrease in the ionic radius of Ln^{3+} across the series, a behavior known as the lanthanide contraction. Thus, as smaller Ln cations are substituted in the sesquioxides, the stability of the A-type phase, with seven-fold cation coordination, decreases. Concomitantly, the B-type phase, with mixed seven- and six-fold coordination, and the C-type phase, with six-fold coordination, become more stable [116,117]. The compounds that adopt multiple polymorphic structures generally follow a C-to-B-to-A transition pathway with increasing temperature or pressure, with the critical temperatures and pressures for these transformations exhibiting inverse proportionality with the lanthanide cation's ionic radius [91,116,120–127].

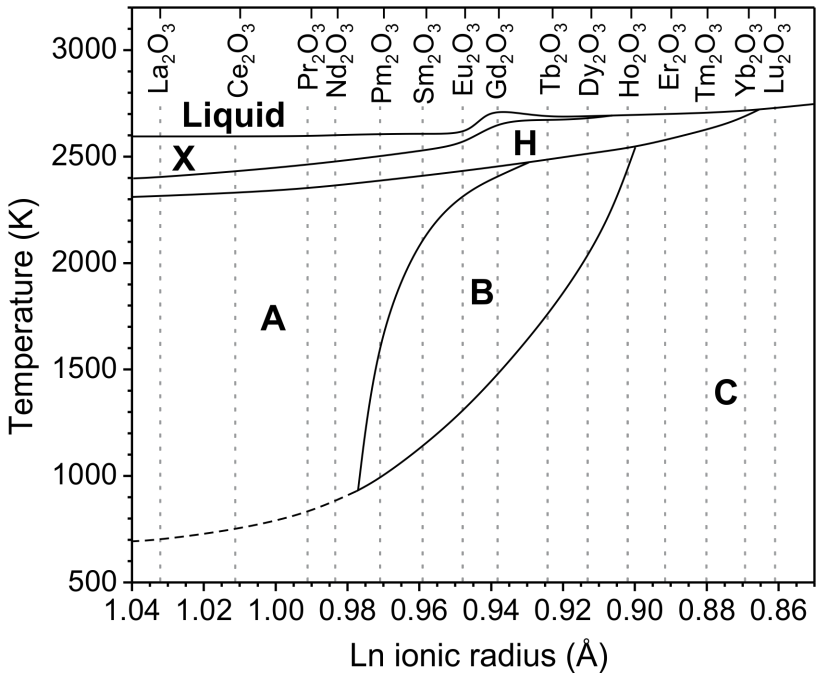

Figure 12: The high temperature polymorphism of the lanthanide sesquioxides as a function of the lanthanide cation's ionic radius. Five equilibrium phases are observed in these materials: trigonal A-type, monoclinic B-type, cubic C-type, hexagonal H-type, and cubic X-type. Because the lanthanide elements have localized 4*f* electrons, they are chemically similar and contract with increasing nuclear charge. This leads to gradual variation in the stability of sesquioxides phases across the lanthanide series, despite a general lack of variation in the accessible stoichiometries of lanthanide oxides, since most are stable only with trivalent cations. Adapted from Coutures *et al.* [119].

Observation of a swift heavy ion irradiation-induced transformation from a C-type to a B-type structure was first reported by Hémon *et al*. [14,128] in Y_2O_3, a material closely related to the lanthanide sesquioxides, and has been confirmed by others [129,130]. Recently, the same transformation has been demonstrated in the lanthanide sesquioxide Gd_2O_3 by Lang *et al.* [131]. In addition, Tang *et al.* [132–135] and Antic *et al.* [136] have shown evidence of this transformation in Gd_2O_3, Dy_2O_3, and Er_2O_3 irradiated with ions of low specific energies (< 5 keV/u), which interact with materials through elastic nuclear collisions. These investigations have studied the radiation responses of only a small number of materials, yielding little insight into the influence of the Ln_2O_3 phase systematics on their irradiation-induced phase behavior.

The gradual variation in the polymorphism of oxides across the lanthanide series makes this an ideal system for the study of phase transformations induced by dense electronic excitation. Such systematic study is particularly relevant to prediction of the behavior of the heavy actinide sesquioxides, An_2O_3 (An = Pu-Es). These compounds have localized 5*f* electrons [137], exhibit a polymorphism analogous to that of the lanthanide sesquioxides [138], and are continuously exposed to radiation in the electronic energy loss regime due to nuclear decay, yet are difficult to synthesize and handle for direct study. Limited data have indicated transformations of C-type Am_2O_3 and Cm_2O_3 to high temperature polymorphs following self-irradiation with alpha particles of high specific energy [139–141].

In this work, lanthanide sesquioxides with compositions spanning the stability range of the C-type phase were irradiated with swift heavy ions of differing mass and energy in order to systematically characterize their phase behavior under these non-equilibrium conditions and to determine its relation to the equilibrium phase systematics of this series. Analysis of the dependence of the induced transformations on both the lanthanide ionic radius and the energy deposition parameters allowed for the observed phase transformations to be related to the production of specific crystallographic defects and accompanying phase transformation mechanisms. This yields the basis for the prediction of the radiation responses of related materials, as it provides information on the dynamic atomistic processes that such materials undergo during and following the transfer of energy from a hot electron-hole plasma to an atomic structure.

3.1 Experimental methods

Samples were made from powders of Sm_2O_3, Gd_2O_3, Ho_2O_3, Tm_2O_3, and Lu_2O_3 with typical grain sizes on the order of 1 μm, supplied by Alfa Aesar. They were annealed in air for 24

hours at 1000 K to remove any water present and ensure high crystallinity. Holes of 100 μm diameter were drilled into 50 μm and 25 μm thick stainless steel sheets using electric discharge machining, and the powders were uniaxially pressed into these cavities using a hydraulic press operating at a pressure of 20 MPa. Typical densities of the compacted powders were 40-50% of the theoretical densities of the bulk materials. X-ray diffraction measurements confirmed that all samples adopted a well-crystallized C-type structure prior to irradiation.

Irradiations were performed with the UNILAC accelerator at the GSI Helmholtz Centre for Heavy Ion Research in Darmstadt, Germany, using 2246 MeV Au ions at the M2 beamline and 185 MeV Xe ions at the HLI beamline. All samples were exposed simultaneously to an ion beam defocused to approximately 1 cm^2. To prevent bulk heating of the samples, the ion flux was maintained below 2×10^9 ions cm^{-2} s^{-1} for the Au beam and below 4×10^9 ions cm^{-2} s^{-1} for the Xe beam. Identical sample sets were irradiated to various ion fluences, Φ, ranging from 5×10^{10} ions cm^{-2} to 5×10^{13} ions cm^{-2}, with typical fluence uncertainties of ~10%. Accounting for the different energies of the two ion beams, and therefore their different ranges in the material as calculated with the SRIM code [34], 50 μm thick samples were used in conjunction with Au irradiation, and 25 μm thick samples were used in conjunction with the Xe irradiation. This ensured that all ions passed completely through the samples and that the ion end-of-range region, in which nuclear collisions dominate the transfer of energy to the material, was excluded.

After irradiation, the long-range structures of the samples were characterized using angle-dispersive micro-beam x-ray diffraction at beamline X17C of the National Synchrotron Light Source at Brookhaven National Laboratory. A monochromatic beam of wavelength $\lambda = 0.4082$ Å was used, calibrated with a CeO_2 standard. Measurements were collected in transmission geometry, with the x-ray beam parallel to the axis of ion beam irradiation, such that the x-rays

probed the entire length of the ion tracks. Debye rings diffracted from each sample were recorded for 300 s on a Mar CCD detector. The resulting two-dimensional diffraction patterns were integrated in the azimuthal direction with the software FIT2D [110]. Rietveld refinement [111] of the resulting diffractograms was performed with the software FullProf [142] to characterize irradiation-induced phase transformations and to determine phase fractions as a function of ion fluence.

The local structure and bonding of the irradiated materials were characterized by Raman spectroscopy. A confocal Horiba Jobin Yvon HR800 system with a 20nW He-Ne laser was used, with an excitation wavelength of $\lambda = 632.8$ nm to minimize photoluminescence signal from point defects. A diffraction grating with 1800 grooves/mm provided a spectral resolution of approximately 0.01 nm. Multiple spectra were collected from randomly selected areas of each sample, with a laser spot size of approximately 1 μm^2. Each measurement was performed for 40 s, and each final spectrum was averaged over three measurements to reduce noise.

3.2 Results

3.2.1 Irradiation with 2246 MeV Au ions

Energy deposition by 2246 MeV Au ions caused Sm_2O_3, Gd_2O_3, and Ho_2O_3 to transform from the initial C-type phase to a B-type polymorph. Representative XRD patterns from Sm_2O_3 illustrating this transformation are shown in Figure 13. Formation of the irradiation-induced phase is indicated by the growth of new diffraction maxima concomitant with the attenuation of the initial maxima, which correspond to the C-type structure, as the ion fluence increases. Refinement showed that the new peaks fit well to the B-type structure. Evidence of this transformation was not observed in sesquioxides of the lanthanide elements with higher atomic number (Tm_2O_3 and Lu_2O_3). The C-to-B transformation entails modification of the crystal

structure and symmetry, as well as an increase in density of approximately 10%, an unusual result considering that defect production by swift heavy ion irradiation causes swelling in many oxides, rather than densification [18,143].

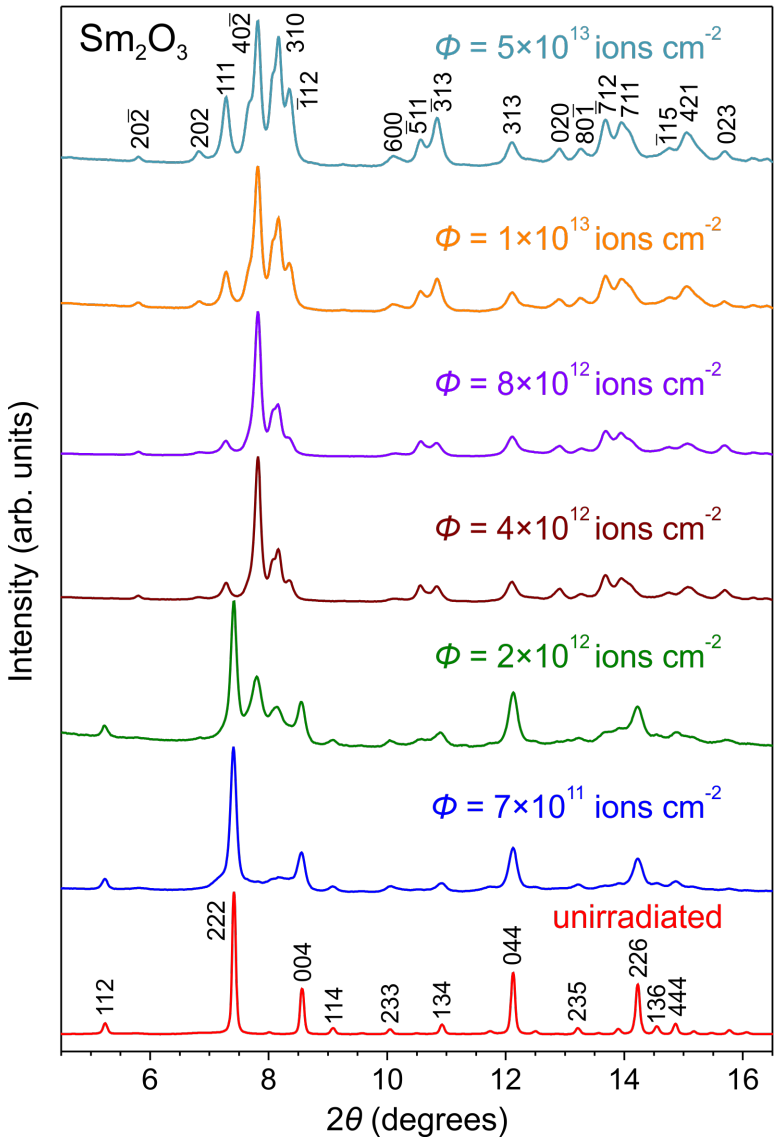

Figure 13: XRD data showing an irradiation-induced transformation from the C-type phase to the B-type phase in Sm_2O_3 irradiated with 2246 MeV Au ions. The transformation is indicated by the appearance and growth of new diffraction maxima with increasing ion fluence, Φ. The pattern corresponding to the unirradiated sample corresponds to a fully C-type material, with the peak indexing shown. At ion fluences of $\Phi = 4 \times 10^{12}$ ions cm^{-2} and greater, the patterns correspond to a fully B-type material, with the indexing shown on the top pattern. At intermediate fluences, a mixture of the two phases is observed. Growth of the B-type (40-2) peak occurs more rapidly than that of other peaks, indicating that the B-type ordering occurs preferentially in this crystallographic direction.

While all peaks in the XRD patterns collected from these three materials can be indexed with either the C-type or B-type structures, the relative intensities of the B-type maxima differ substantially from those of a well-crystallized, polycrystalline B-type material with randomly oriented crystallites. Furthermore, these relative intensities evolve with increasing ion fluence, even after the C-to-B transformation is complete. As shown in Figure 13, the B-type (40-2) peak intensity increases rapidly as the transformation proceeds, while the intensities of all other peaks increase more slowly. Thus, at intermediate ion fluences (between $\Phi = 4 \times 10^{12}$ ions cm^{-2} and $\Phi = 1 \times 10^{13}$ ions cm^{-2}) the diffraction patterns show no evidence of the initial C-type phase, but also differ from that corresponding to the highest ion fluence achieved, $\Phi = 5 \times 10^{13}$ ions cm^{-2}, in that they are dominated by the (40-2) peak. Only at the highest ion fluence do the remaining B-type peaks reach intensities commensurate with the ideal B-type phase. Similar behavior was observed in the other materials that underwent a C-to-B transformation (Gd_2O_3 and Ho_2O_3). Such deviation in relative peak intensities from that of an ideal phase can be caused by evolution of: (i) site occupancy, if the scattering contributions of specific crystallographic sites vary between diffraction peaks, or (ii) crystallite orientation, if the B-type phase forms preferentially in specific crystallographic directions corresponding to the dominant diffraction maxima. Changes in site occupancy with increasing ion fluence could be caused by preferential B-type ordering on either the cation or anion sublattices, such that scattering from specific sites preceded that from others. However, refinement of the occupancy fractions of all B-type sites showed that the deviations in peak intensity were inconsistent with changes in occupancy. Therefore, this behavior is attributed to an orientation dependence of the C-to-B transformation. The two-dimensional detector images from which the diffractograms were obtained showed highly homogeneous Debye rings, with photon counts showing minimal variation as a function of

azimuthal angle. This indicates that the orientation effect does not arise from poor sampling statistics of a textured sample, which would yield spotty Debye rings, and is instead suggestive of anisotropic characteristics of the C-to-B transformation.

The results of Raman spectroscopy measurements provide further evidence of the irradiation-induced C-to-B transformation in Sm_2O_3, Gd_2O_3, and Ho_2O_3. Representative spectra from Gd_2O_3 are shown in Figure 14. The initial spectra, from the unirradiated samples, correspond to the C-type phase, consisting of a sharp band from the A_g+T_g vibrational modes at ~120 cm^{-1}, along with seven T_g and three E_g modes [144,145]. At the highest ion fluence achieved, $\Phi = 5 \times 10^{13}$ ions cm^{-2}, the spectra show no evidence of C-type phonon modes, and instead correspond to the B-type phase. This phase nominally exhibits twenty-one Raman-active modes, including fourteen A_g modes from atomic vibrations in the basal (010) planes and seven B_g modes arising from out-of-plane vibrations, however, fewer modes are typically observed, as is the case here [144,145]. Instead, seventeen modes are apparent in the wavenumber range 110-600 cm^{-2}, comprising twelve A_g modes, four B_g modes, and one B_g+A_g mode. At intermediate fluences, for which XRD results show that irradiation has induced the adoption of a B-type long-range structure in a significant fraction of the material, the Raman signal from this phase remains weak. At the ion fluence of $\Phi = 6 \times 10^{12}$ ions cm^{-2} in Figure 14, for example, only a few weak, broad bands around 175 cm^{-1}, 265 cm^{-1}, and 480 cm^{-1} provide evidence of the transformation. Raman spectroscopy is highly sensitive to the coordination and local symmetry of a material, as these govern the accessible vibrational states. This means that even minor distortion or insufficient ordering of a material in specific crystallographic directions, which would have comparatively little effect on XRD measurements, can strongly attenuate Raman spectroscopy signal. Such attenuation is consistent with the observation, from the XRD data, that the B-type

phase does not initially form in a well-crystallized, isotropic manner, but instead the C-to-B transformation is highly orientation dependent. As such, only once a structure close to that of the ideal B-type phase is formed (*i.e.* at an ion fluence of $\Phi = 5 \times 10^{13}$ ions cm^{-2} in Figure 13) will strong Raman vibrational modes be observed. At lower fluences, the spectra are instead dominated by signal arising from the remaining, un-transformed C-type volume.

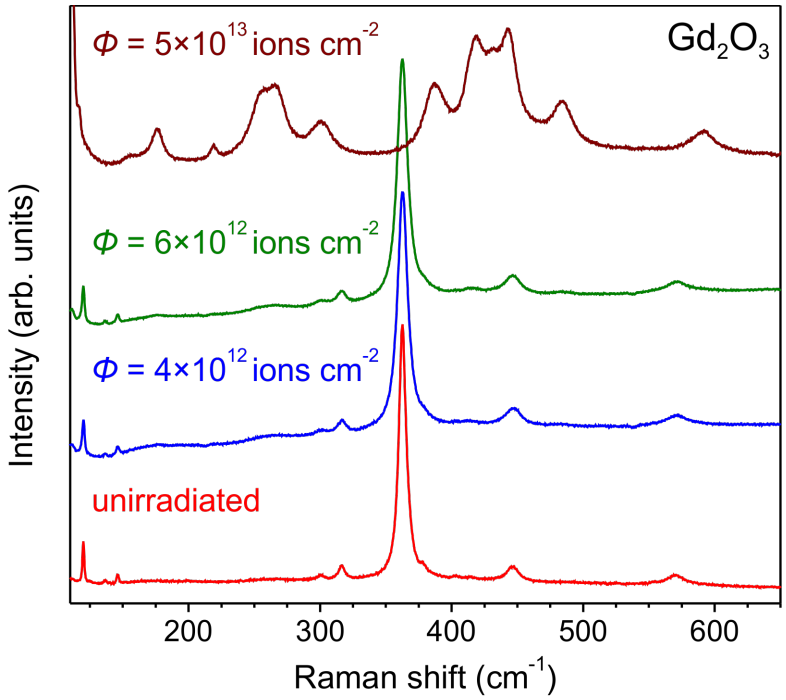

Figure 14: Raman spectra showing the C-to-B transformation in Gd_2O_3 irradiated with 2246 MeV Au ions. The spectrum from the unirradiated sample is consistent with a C-type phase, while that corresponding to an ion fluence of $\Phi = 5 \times 10^{13}$ ions cm^{-2} is consistent with a complete transformation to the B-type phase. At intermediate ion fluences, very weak bands matching the B-type spectrum are evident, but the spectra are dominated by C-type vibrational modes.

Analysis of the C-type and B-type phase fractions in each material, as a function of ion fluence, shows that the transformation rate decreases as lanthanides of higher atomic number, and therefore smaller ionic radius, are substituted in the sesquioxides. Comparison of diffraction patterns collected from different sesquioxides at the same ion fluence, as shown in Figure 15, shows qualitatively that the B-type phase fraction decreases with increasing lanthanide atomic

number. The intensities of the B-type diffraction maxima, relative to those of maxima corresponding to the C-type structure, decrease substantially across the lanthanide series. Figure 16 shows corresponding quantitative data on the B-type phase fractions for all samples, extracted from refinement of the XRD patterns. From Poisson statistics, a model for the accumulation of modified material with increasing ion fluence can be developed. The data in Figure 16 are best fit when such a model is based on the assumption of a single-impact transformation process [146], wherein each impinging ion causes a columnar volume centered on its path (the ion track) to transform from its initial phase to the B-type polymorph. This yields the equation:

$$f\left(\Phi\right) = 1 - e^{\left(-\sigma\Phi\right)} \tag{1}$$

where $f(\Phi)$ is the phase fraction of the irradiation-induced phase, σ is the cross-sectional area of the ion track, and Φ is the ion fluence. The observation of single-impact damage accumulation is consistent with the results of Hémon *et al.* [128] for the same transformation in Y_2O_3 irradiated with swift heavy ions. The data in Figure 16 are fit with this model, yielding track diameters for the C-to-B transformation of 10.1 ± 0.9 nm, 4.0 ± 0.7 nm, and 3.2 ± 0.8 nm in Sm_2O_3, Gd_2O_3, and Ho_2O_3, respectively, assuming cylindrical track geometry. No such transformation was observed for Tm_2O_3 and Lu_2O_3. This indicates that the amount of material transformed to the B-type phase per incident ion is proportional to the atomic number of the constituent lanthanide element. In other words, materials in the Ln_2O_3 system become more resistant to the irradiation-induced C-to-B transformation with decreasing lanthanide ionic radius.

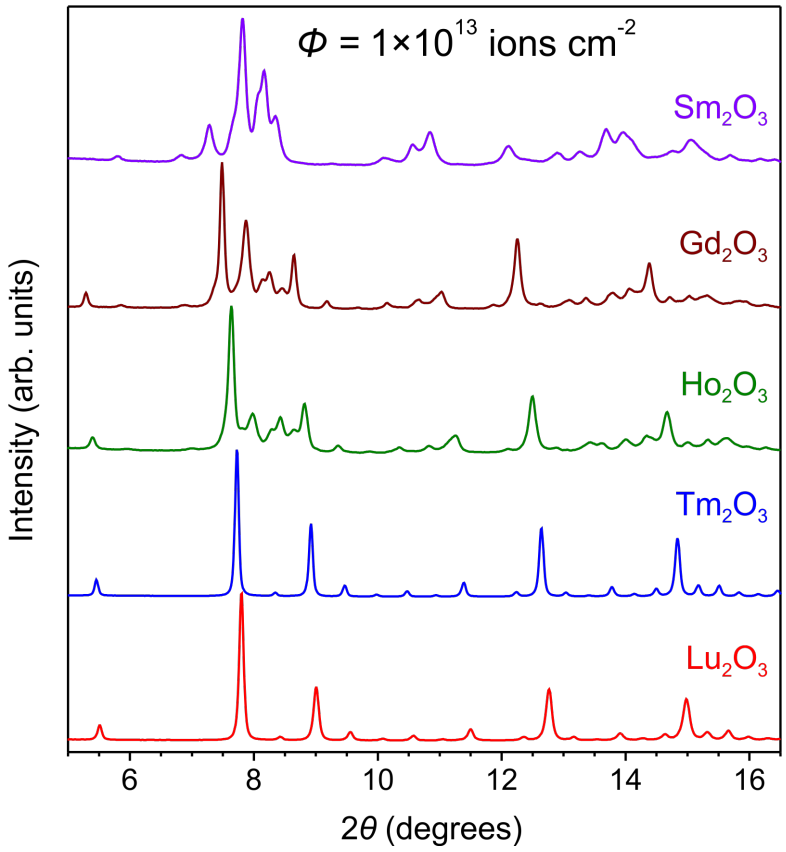

Figure 15: XRD patters of all Ln_2O_3 materials investigated, irradiated to an ion fluence of $\Phi = 1 \times 10^{13}$ ions cm^{-2}. The B-type phase fraction, which is proportional to the intensity of the corresponding diffraction maxima, decreases across the lanthanide series. The two materials with lanthanide cations of highest atomic number, Tm_2O_3 and Lu_2O_3, show no evidence of a phase transformation.

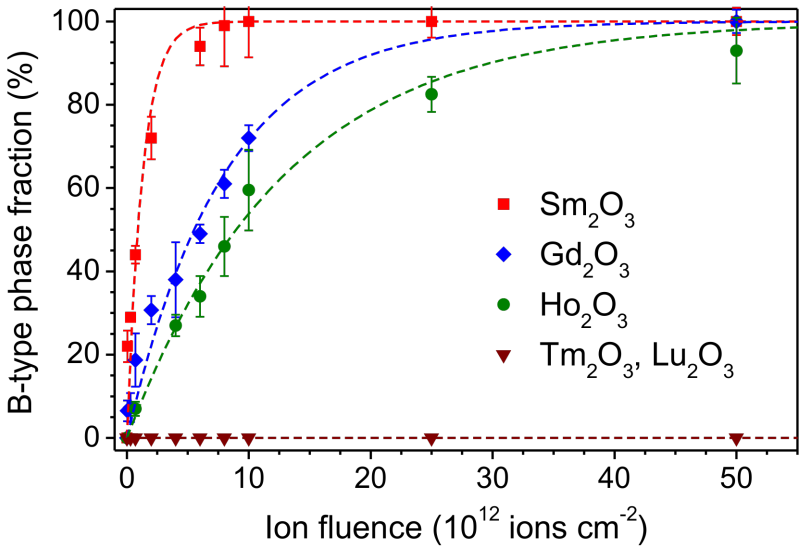

Figure 16: B-type phase fractions for all Ln_2O_3 materials investigated as a function of 2246 MeV Au ion fluence. At each ion fluence, the transformed fraction decreases with increasing lanthanide cation atomic number. No B-type phase fraction exists for Tm_2O_3 and Lu_2O_3 at any ion fluence, as they do not undergo a C-to-B transformation. The data corresponding to each material are fit with a single-impact damage accumulation model (Eq. 1), shown by the dotted lines. Error bars represent the standard deviations of phase fractions determined by refinement of multiple patterns.

The two materials containing the lanthanide cations of highest atomic number, among those tested, did not show evidence of formation of a B-type phase and largely retained their C-type structure under irradiation with 2246 MeV Au ions. Figure 17 shows representative XRD data for Lu_2O_3. For all ion fluences below $\Phi = 5 \times 10^{13}$ ions cm^{-2} only diffraction maxima corresponding to the C-type phase were observed. At the highest ion fluence achieved, diffraction patterns from both Tm_2O_3 and Lu_2O_3 revealed the emergence of a new diffraction peak of very low intensity, seen at $2\theta \approx 8.2°$ in Figure 17. The angular position of this peak is inconsistent with both the B-type phase, which is not known to form for either of these compounds, and the H-type phase, which forms at high temperature in Tm_2O_3 only (see Figure 12). However, the low intensity of this peak and the lack of other observable peaks corresponding to the new structure, which likely indicate a very small phase fraction, make it unsuitable for refinement and structure determination. Raman spectroscopy (not shown) showed

no evidence of irradiation-induced vibrational modes in these materials, further suggesting that only a small volume of material adopted this unidentified structure.

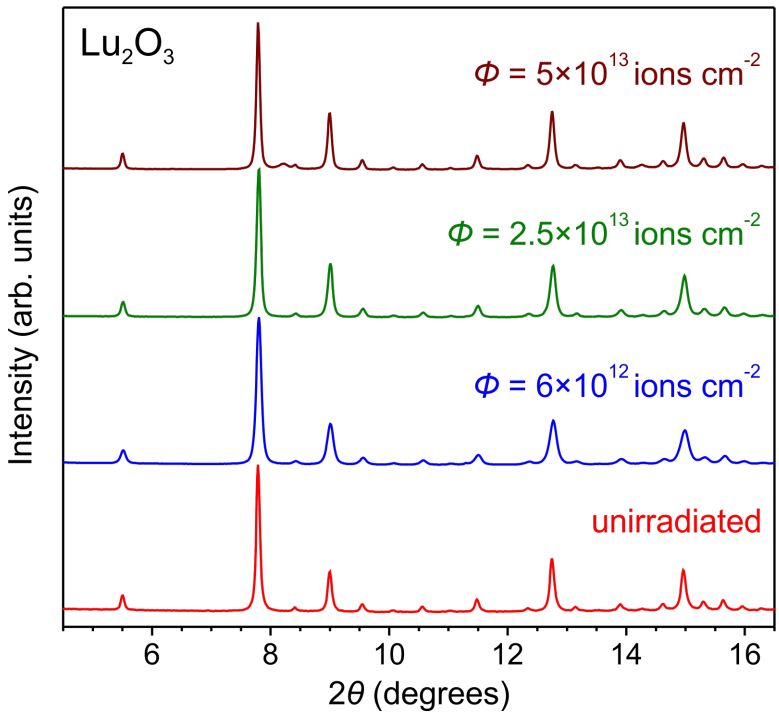

Figure 17: XRD patterns collected from Lu_2O_3 irradiated with 2246 MeV Au ions. The material largely retains its C-type structure during irradiation, but shows a single new diffraction peak at the highest ion fluence achieved of $\Phi = 5 \times 10^{13}$ ions cm^{-2}. This peak, at a diffraction angle of $2\theta \approx 8.2°$, cannot be indexed to a B-type phase, indicating that a sluggish transformation to a different crystalline phase is induced in this material by irradiation with swift heavy ions.

3.2.2 Irradiation with 185 MeV Xe ions

The phase responses of all materials in the Ln_2O_3 system to irradiation with 185 MeV Xe ions differ substantially from those observed under irradiation with the Au ions of higher mass and energy. For the three sesquioxides with lanthanides of relatively low atomic number and high ionic radius, Sm_2O_3, Gd_2O_3, and Ho_2O_3, an irradiation-induced loss of long-range structural periodicity was observed. As illustrated in Figure 18, which shows representative XRD patterns for Ho_2O_3, the dominant response to 185 MeV Xe irradiation was the production of an amorphous phase, as indicated by the growth of broad features characteristic of diffuse scattering

from an aperiodic arrangement of atoms. Additional peaks of low intensity corresponding to a B-type phase are evident, superimposed on the diffuse scattering background, indicating the partial occurrence of a C-to-B transformation. However, in contrast to the phase behavior of these materials under irradiation with 2246 MeV Au ions, it is clear that this C-to-B transformation is largely precluded by the concurrent amorphization. Additionally, a portion of the C-type phase is retained to the highest ion fluences measured. Some volume of the sample has not been transformed to either the amorphous or B-type phases at these fluences, suggesting a relatively small ion track cross-sectional area. Raman spectra (not shown) from these samples were consistent with a mixture of C-type, B-type, and amorphous [147] phases.

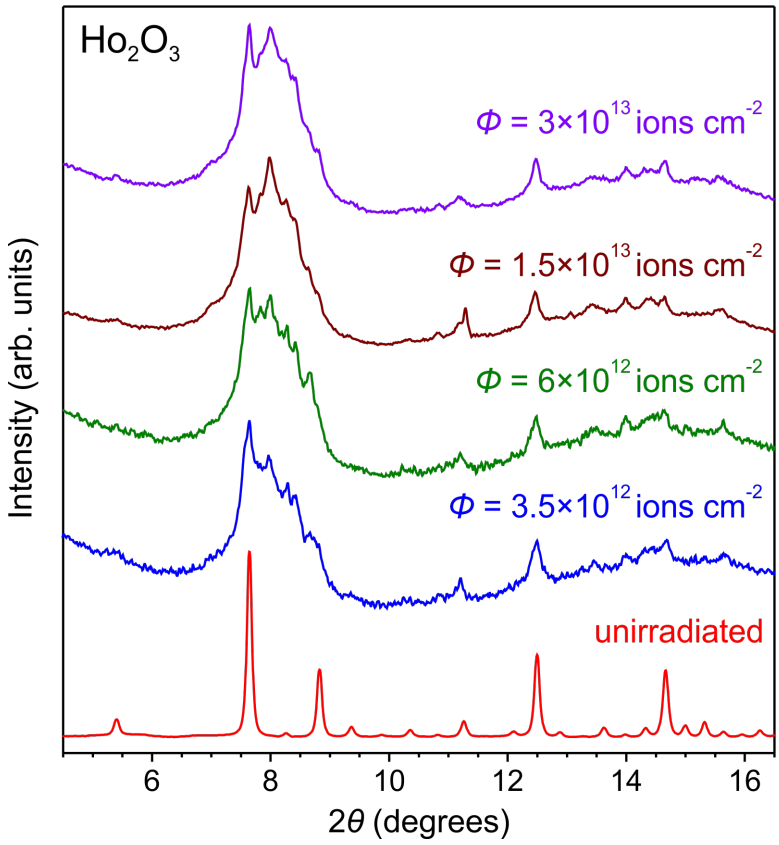

Figure 18: XRD patterns collected from Ho_2O_3 irradiated with 185 MeV Xe ions. The primary effect of irradiation is a transformation from the initial C-type phase to an amorphous phase, giving rise to diffuse x-ray scattering. Signal resulting from the amorphous phase is most evident in the broad feature centered at a diffraction angle of $2\theta \approx 8°$ in the diffractograms collected from irradiated samples. At all ion fluences, peaks corresponding to the C-type and B-type phases

coexist with this diffuse scattering signal, indicating that some material remains untransformed and some undergoes a C-to-B transformation.

As was the case for irradiation with 2246 MeV Au ions, the radiation-tolerant sesquioxides with lanthanides of high atomic number, Tm_2O_3 and Lu_2O_3, exhibited much greater retention of their initial C-type structures under irradiation, as compared with the other compounds tested. As shown in Figure 19, neither a B-type phase nor an amorphous phase forms as irradiation proceeds. These materials instead exhibit a sluggish transformation to a distinct crystalline phase. The most intense diffraction maxima arising from the irradiation-induced phase are at diffraction angles of $2\theta \approx 8.2°$ and 14.2°. The former peak position is in good agreement with that of the single, low intensity peak observed in these material under irradiation with 2246 MeV Au ions, suggesting that the same phase forms under both irradiation conditions, albeit at different rates. The growth of these peaks is relatively slow, as compared with the C-to-B and C-to-amorphous phase transformations observed in the compounds with lanthanides of large ionic radii. However, it is much more rapid, as a function of fluence, than the same transformation induced by the 2246 MeV Au ions.

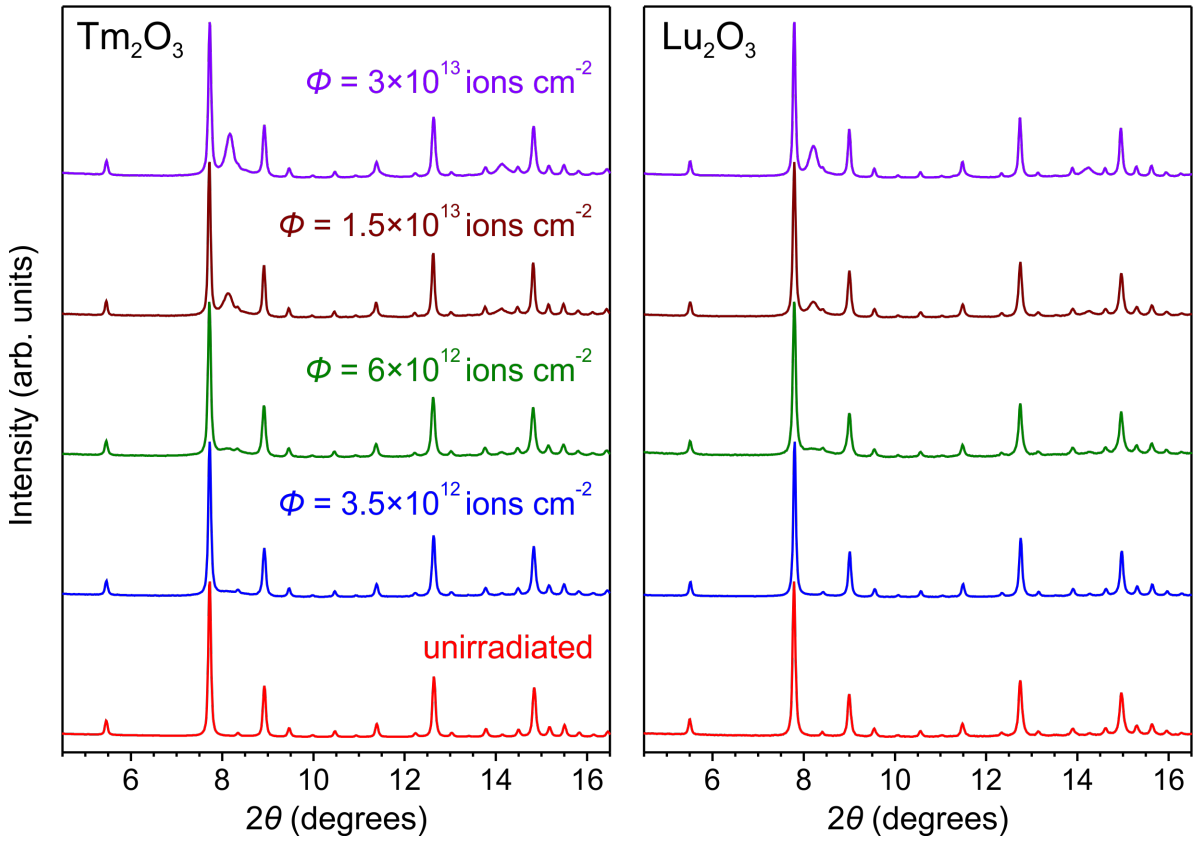

Figure 19: XRD patterns showing an irradiation-induced transformation from the C-type phase to a phase with the X-type structure in Tm_2O_3 and Lu_2O_3 irradiated with 185 MeV Xe ions. This transformation, which is sluggish compared to the C-to-B transformation in sesquioxides with lanthanides of lower atomic number, is most clearly indicated by the emergence of new diffraction maxima at $2\theta \approx 8.2°$ and 14.2° with increasing ion fluence.

Refinement was performed on XRD data collected from both Tm_2O_3 and Lu_2O_3 after irradiation. Structure models corresponding to all known polymorphs in the Ln_2O_3 series were used, as well as those of other transition metal sesquioxides that exhibit the C-type bixbyite structure, including Mn_2O_3 and In_2O_3. The only structure yielding a satisfactory fit to the irradiation-induced peaks was that of the Ln_2O_3 X-type (*Im*-3*m*) phase, which has previously been observed only for materials with lanthanide cations of lower atomic number than Ho. Additionally, this phase has never before been recovered to ambient conditions, occurring only at temperatures above 2400 K [119,148]. Thus, swift heavy ion irradiation of lanthanide sesquioxides with cations of small ionic radius produces a newly-observed, non-equilibrium

phase. Figure 20 shows representative data from the Rietveld refinement of Lu_2O_3 at an ion fluence of $\Phi = 3 \times 10^{13}$ ions cm^{-2}, illustrating the goodness of fit of a C-type and X-type mixture to the diffraction data. Measured unit cell parameters of the X-type phase were 4.0504(5) Å for Tm_2O_3 and 4.0312(7) Å for Lu_2O_3. This phase exhibits a body-centered cubic cation sublattice, with lanthanides in the 2*a* position, along with a highly disordered anion sublattice rich in constitutional vacancies. The precise positions of the anions have not been determined, due in large part to the fact that the formation of this phase has previously been achieved only at very high temperatures, but the 6*b* (50% occupancy), 12*d* (25% occupancy) and 24*g* (12.5% occupancy) sites have been proposed [118]. Due to the poor sensitivity of x-ray scattering techniques to oxygen, the data obtained here is not sufficient for determination of the anion sublattice structure. Refined X-type phase fractions for both materials are shown in Figure 21, along with results from the fitting of a single-impact model (Eq. 1), which best fits the data. As is clear from qualitative analysis of the diffraction patterns, the C-to-X transformation occurs very slowly, as a function of ion fluence, compared with the other phase transformations observed in this investigation. The model yields ion track radii of 1.4 ± 0.2 nm and 1.3 ± 0.1 nm for the transformation in Tm_2O_3 and Lu_2O_3, respectively. In contrast to the C-to-B transformation behavior, these values are within error of one another, such that no influence of lanthanide ionic radius on the radiation response of these materials is evident.

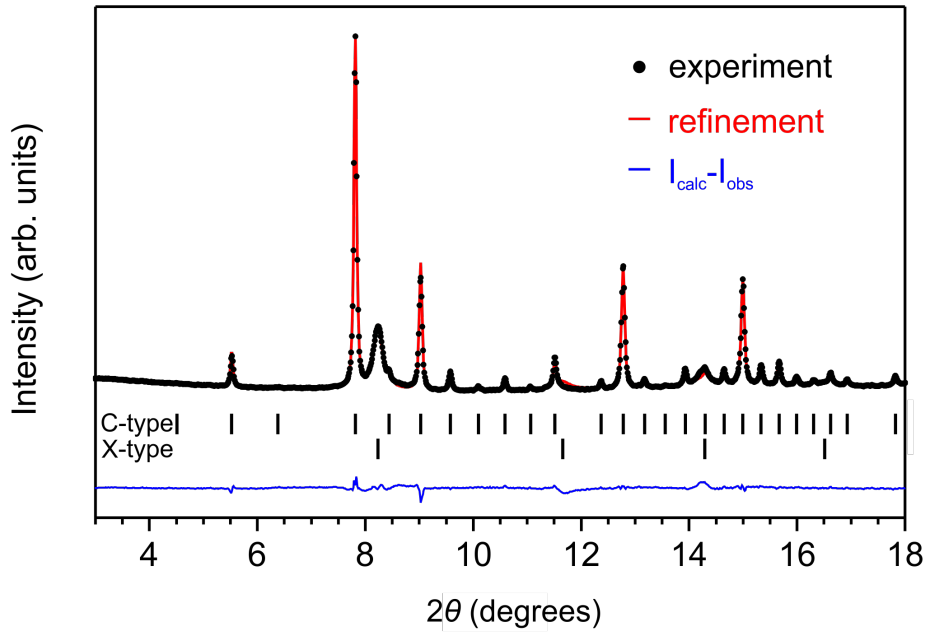

Figure 20: Refinement of an XRD pattern collected from Lu_2O_3 irradiated with 185 MeV Xe ions to a fluence of $\Phi = 3 \times 10^{13}$ ions cm^{-2}. The simulated pattern, shown by the red line, fits well to the experimental data, shown by the black circles. As shown by the vertical lines marking the angular positions of C-type and X-type phases, the pattern is well-indexed as a mixture of these two phases, with only small deviations between the simulated and experimental patterns, as shown by the blue line.

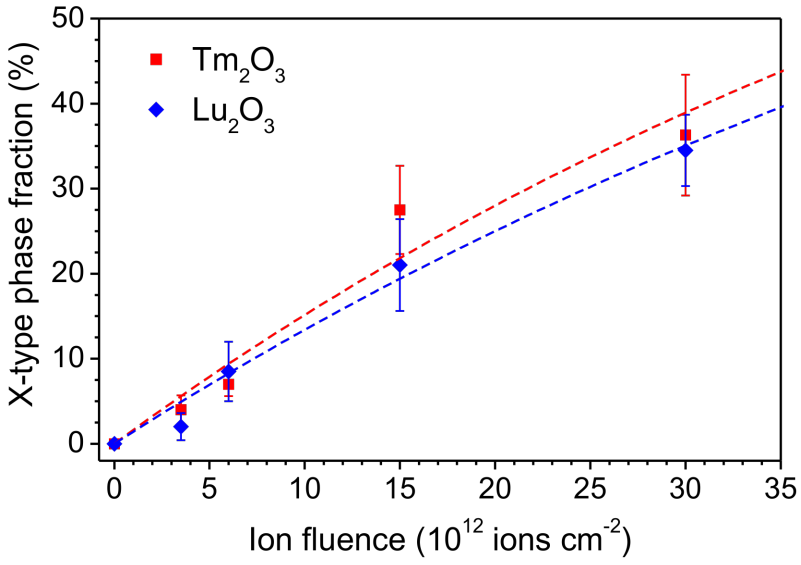

Figure 21: X-type phase fractions of Tm_2O_3 and Lu_2O_3 as a function of 185 MeV Xe ion fluence. At all fluences, these phase fractions for the two materials are within error of one another. This transformation is relatively sluggish, reaching phase fractions below 50% at the highest ion

fluence achieved. The data corresponding to each material are fit with a single-impact damage accumulation model (Eq. 1), shown by the dotted lines. Extrapolation based on this model suggests that the transformation to the X-type phase will be complete at ion fluences on the order of $\Phi = 1 \times 10^{14}$ ions cm^{-2}. Error bars represent the standard deviations of phase fractions determined by refinement of multiple patterns.

Raman spectra from these materials show irradiation-induced changes distinct from those of the sesquioxides that underwent the C-to-B or C-to-amorphous transformations. As seen in Figure 22, which shows representative data from Tm_2O_3, the vibrational modes of the unirradiated material correspond to a well-crystallized C-type phase, consistent with the XRD results. As the ion fluence increases, several broad bands grow in intensity; whereas, the C-type modes are attenuated. The irradiation-induced signal, which is attributed to the X-type phase, is similar to that of amorphous Ln_2O_3 materials [147], which share the bands centered around 90 cm^{-1} and 350 cm^{-1}. This similarity is consistent with the formation of a highly disordered structure with low occupancy of anion sites, as significant variation in the Ln-O coordination is expected in such a material. Several additional bands were observed in the X-type material, which are not present in the spectra of the amorphous phase, such as that at approximately 175 cm^{-1}. This is the first instance in which a Raman spectrum corresponding to an X-type phase has been reported.

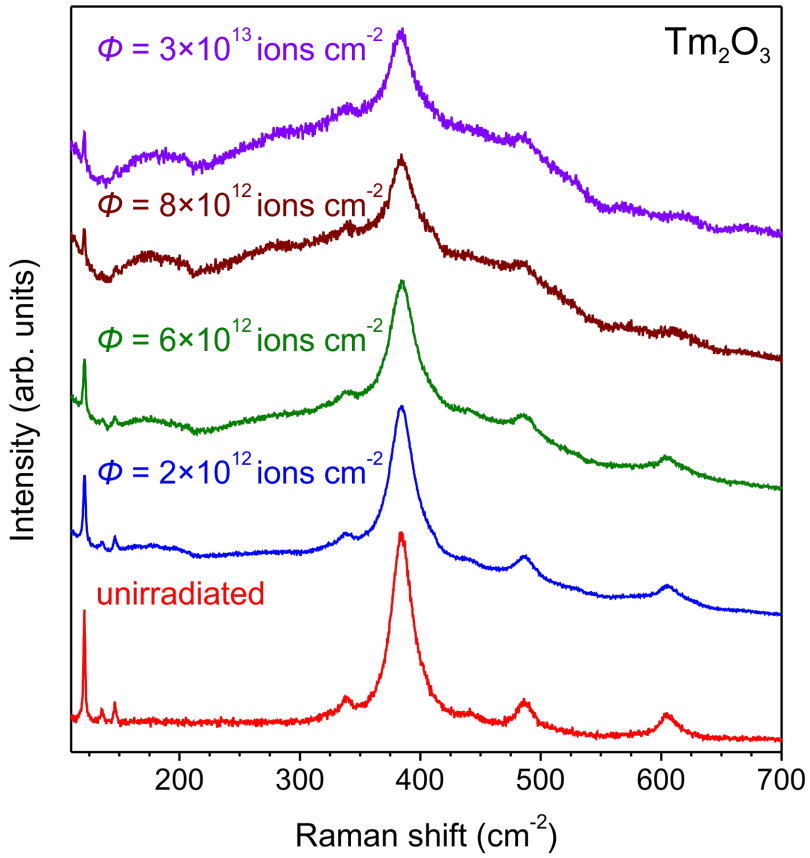

Figure 22: Raman spectra collected from Tm_2O_3 irradiated with 185 MeV Xe ions. The spectrum from the unirradiated sample is consistent with a pure C-type phase. With increasing ion fluence new, broad bands appear and grow, indicating a transformation to the X-type phase. Concurrently, the existing bands corresponding to vibrational modes of the C-type structure are attenuated. The existence of C-type peaks at the highest fluence achieved indicates that the C-to-X transformation remains incomplete, consistent with the XRD results.

3.3 Discussion

3.3.1 C-to-B transformation

A transformation from the initial C-type structure to the B-type polymorph occurred in some materials under both 2246 MeV Au and 185 MeV Xe irradiations, although it was accompanied by significant amorphization in the latter. Notable features of this transformation include its unique orientational behavior, with B-type ordering in the [40-2] direction preceding that of other orientations, its dependence on irradiation conditions, with 2246 MeV Au ion irradiation causing a more extensive transformation than 185 MeV Xe ion irradiation, and its

dependence on sesquioxides composition, with materials featuring lanthanides of large ionic radius transforming more rapidly than those with smaller cations. To understand this behavior, it is essential to consider the atomistic processes that drive the phase transformation.

The primary effect of ion irradiation-induced electronic excitation on a material's atomic subsystem, following relaxation from a state of warm dense matter, is the production of structural defects through the displacement of atoms. There are three intrinsic defect modes accessible to Ln_2O_3 materials: Frenkel pair formation, anti-Frenkel pair formation, and Schottky defect formation. These defect reactions are represented in Kröger-Vink notation as:

$$Ln_{Ln}^{\times} \rightleftharpoons V_{Ln}^{'''} + Ln_i^{\bullet\bullet\bullet} \tag{2}$$

$$O_O^{\times} \rightleftharpoons V_O^{\bullet\bullet} + O_i^{''} \tag{3}$$

$$2Ln_{Ln}^{\times} + 3O_O^{\times} \rightleftharpoons 2V_{Ln}^{'''} + 3V_O^{\bullet\bullet} + Ln_2O_3 \tag{4}$$

respectively, where an Ln^{3+} vacancy, $V_{Ln}^{'''}$, and an Ln^{3+} interstitial, $Ln_i^{\bullet\bullet\bullet}$, constitute a Frenkel pair and an O^{2-} vacancy, $V_O^{\bullet\bullet}$, and an O^{2-} interstitial, $O_i^{''}$, constitute an anti-Frenkel pair. Atomistic simulations have shown that oxygen anions have the lowest threshold displacement energy, E_d, in these materials [149]. Thus, energy deposited by a swift heavy ion and subsequently transferred to the atomic subsystem will tend to displace more anions than cations. Displaced anions can localize on vacant 16*c* constitutional vacancy sites on the C-type anion sublattice with a very low resulting increase in lattice energy. Consequently, simulations have shown that anti-Frenkel pair formation is the lowest energy defect mode in these materials, followed by Schottky defect formation [150]. Frenkel defects are much higher in energy at ~9-10 eV, compared with ~4 eV for anti-Frenkel pairs, regardless of composition. Both anti-Frenkel pair and Schottky defect formation produce predominantly anion sublattice defects, further

indicating that oxygen vacancies will be the most common form of structural damage in an irradiated Ln_2O_3 material.

An oxygen vacancy-driven mechanism for this transformation, similar to those described by Hyde [151] for transformations between Ln_2O_3 phases and related structure-types, is consistent with the data presented here. The C-type structure, wherein cations are coordinated by six anions in distorted octahedra, can adopt seven-fold, monocapped octahedral coordination of cations and a long-range periodicity characteristic of the A-type phase via the removal of oxygen atoms from some C-type (222) planes, followed by crystallographic shear of the adjacent matrix into the empty space left by this anion displacement. This exclusive seven-fold cation coordination is unstable when the ionic radii of the lanthanide cations is smaller than that of Nd (see Figure 12). Thus, for such materials, this structure will spontaneously transform to that of the B-type phase, which requires only a slight distortion of the A-type structure in the form of minor oxygen atom motion [91,121,122,145,151]. Density functional theory calculations indicate that these A-type and B-type structures have very similar formation energies, making the reversible transformation between the two energetically inexpensive [152]. This efficient displacive transformation gives rise to a B-type mixed six- and seven-fold coordination of cations. These transformation mechanisms, illustrated in Figure 23a, explain how the displacement of oxygen atoms from the (222) anion planes of the C-type structure to the anion sublattice constitutional vacancies leads to the formation of a B-type phase under swift heavy ion irradiation. An oxygen vacancy-driven C-to-B transformation is supported by the observation that synthesis of Gd_2O_3 materials in low oxygen concentration conditions promotes the formation of the B-type phase, rather than the most stable C-type phase [153].

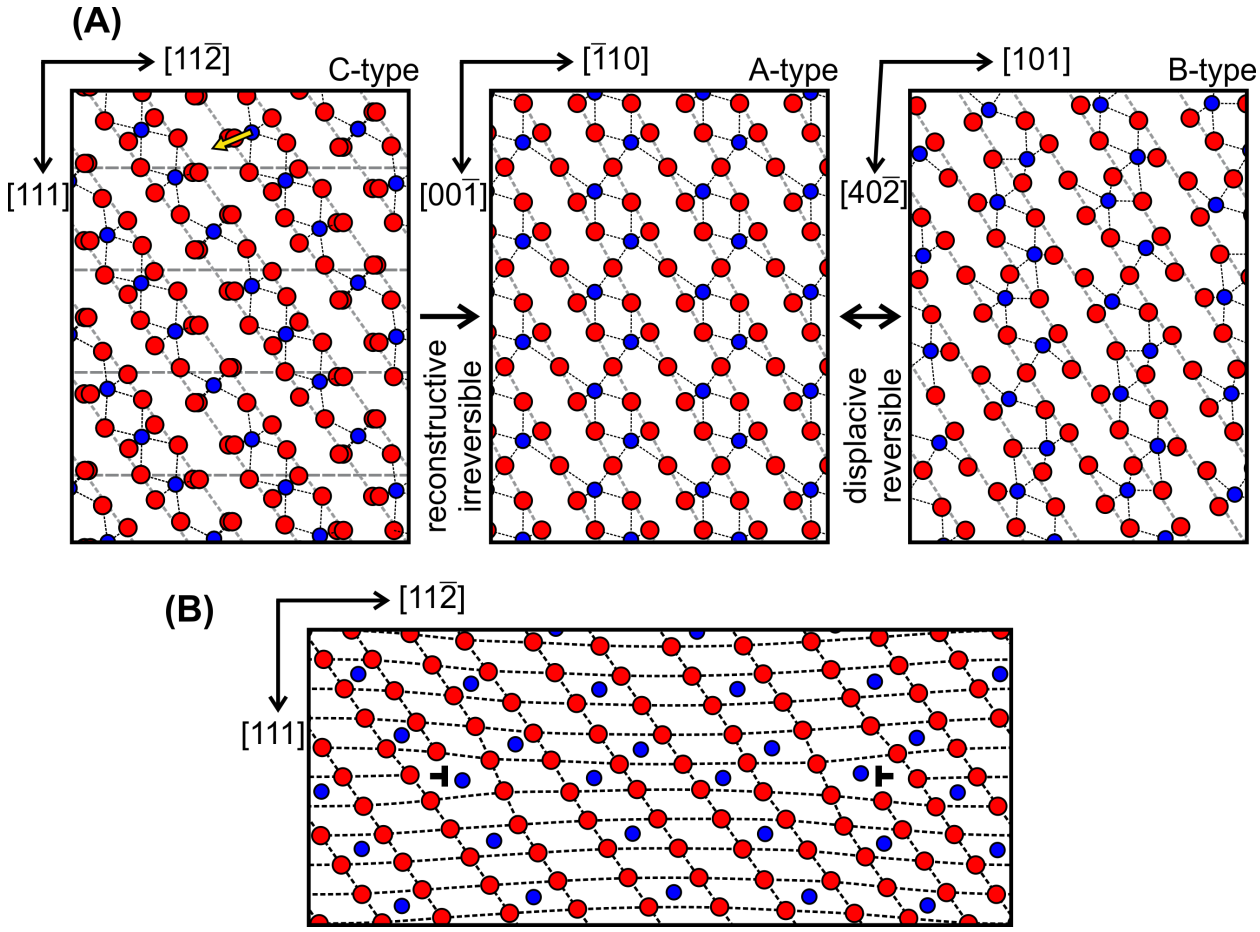

Figure 23: (a) Projections of single (1-10), (-1-10), and (010) cation (blue circles) planes in the C-, A-, and B-type structures, respectively, along with coordinated anions (red circles). The removal of every fourth (222) anion plane in the C-type structure (indicated by the horizontal dashed lines) by the displacement of these anions to vacant 16*c* sites causes crystallographic shear of adjacent cation planes in the direction indicated by the arrow. This process yields A-type ordering, involving an increase in the coordination of cation from six-fold to seven-fold. A reversible, displacive transformation to the B-type phase involves minor motion of oxygen, yielding mixes six- and seven-fold coordination of cations. Diagonal dashed lines are included to highlight the similarities of these three polymorphic phases. (b) Projection of a single (1-10) cation plane in a fluorite-structured material, along with coordinated anions. A fluorite structure is illustrated, rather than the C-type structure, for clarity. A vacancy dislocation loop and accompanying crystallographic shear of an adjacent cation plane cause local ordering characteristic of the A- and B-type polymorphs. In this way, the transformation process described in part (a) can proceed locally, nucleating the polymorphic phase. Dashed lines are included to guide the eye. Adapted from Hyde [151].

In order for this transformation to proceed, isolated oxygen vacancies produced following the formation of anti-Frenkel and Schottky defects must aggregate into planar clusters, known as

dislocation loops, on the (222) anion planes of the C-type phase. In this way, the mechanism described above can occur locally, allowing for nucleation of B-type lamellae, coherent with a C-type matrix [151]. Such a lamella is illustrated schematically in Figure 23b. Molecular dynamics simulations have shown that the oxygen vacancy is the most mobile defect in C-type Ln_2O_3 materials, with migration energies around 1 eV [149,154]. Additionally, electronic excitation from ion irradiation causes ionization-enhanced diffusion in a variety of oxides, promoting the aggregation of defects into these clusters [155,156]. Oxygen vacancy dislocation loops in (222) anion planes have previously been observed in C-type Y_2O_3 thin films grown using ion beam processing [157].

This transformation mechanism is consistent with the observed orientation-dependent formation of the B-type phase. When oxygen vacancy dislocation loops form on C-type (222) planes and crystallographic shear results, the material locally adopts ordering characteristic of B-type (40-2) planes (see Figure 23). These B-type nuclei can then grow, as more irradiation-induced defects are formed, but will always order initially in the B-type [40-2] direction. In the XRD data reported here, it was seen that the B-type (40-2) diffraction peak grew faster than other B-type peaks at intermediate ion fluences (see Figure 13), as it is in this crystallographic direction that the material first adopts B-type ordering. This is also consistent with the Raman spectra obtained from materials that underwent the irradiation-induced C-to-B transformation, as signal from the B-type vibrational modes remained weak at these intermediate ion fluences. In the wavenumber range probed, Raman signal arises primarily from vibrations in the B-type basal (010) planes [145]. Because B-type ordering is initially generated only in the (40-2) planes, significant signal from this phase's Raman-active vibrational modes will not be observed until the B-type nuclei grow at high ion fluences into an isotropically well-crystallized structure. In

previous observations of ion irradiation-induced C-to-B transformations in Y_2O_3 and Dy_2O_3, a crystallographic relationship between the transformed and unirradiated materials was observed [129,130,132,158]. In all cases, B-type (40-2) planes grew parallel to the C-type (222) planes, as is consistent with the measurements reported here.

The observed variation in the phase response of these lanthanide sesquioxides with ion beam mass and energy results from the dependence of the C-to-B transformation on oxygen vacancy production and the characteristics of energy deposition from swift heavy ions. This transformation occurred more extensively during irradiation with 2246 MeV Au ions than during irradiation with 185 MeV Xe ions. The latter instead induced a more substantial modification of its structure, primarily to an amorphous phase. This seemingly contradictory result, of more extensive damage resulting from irradiation with ions of lower energy and mass, is explained by the swift heavy ion velocity effect [159]. As the velocity of a swift heavy ion decreases, so does the radial distance from its path center which excited electrons reach prior to relaxation, reducing the distance within which the ion deposits energy to a material. For example, Meftah *et al.* showed that the in-track energy density produced during irradiation of $Y_3Fe_5O_{12}$ with 185 MeV Xe ions was more than twice that produced by irradiation with 2484 MeV Pb ions [159]. These ion masses, energies, and velocities are close to those used in the present work, such that qualitatively similar proportionality between ion velocity and deposited energy density can be assumed. Thus, while the total energy deposited per unit path length by the 2246 MeVAu ions ($dE/dx \approx 49$ keV/nm for all materials) is greater than that of the 185 MeV Xe ions ($dE/dx \approx 30$ keV/nm for all materials), the energy densities produced in the irradiated materials will show the opposite relation. More energy per atom is available for atomic displacement within the smaller energy deposition volumes produced by 185 MeV Xe irradiation, compared with the larger

energy deposition volumes corresponding to 2246 MeV Au irradiation. Based on the identified C-to-B transformation mechanism, formation of the B-type phase requires only the formation of anti-Frenkel defects, produced when oxygen atoms are displaced. This is the lowest-energy defect process accessible to Ln_2O_3 materials, and should therefore be the predominant process over a wide range of energy densities. Furthermore, oxygen becomes mobile, and therefore relatively easy to displace, in lanthanide oxides at temperatures around 600 K, whereas cation transport is appreciable only above around 1200 K [91]. Thus, within the comparatively low energy density 2246 MeV Au ion tracks, the C-to-B transformation occurs exclusively, as the necessary oxygen vacancies are preferentially produced. In contrast, the amorphization observed in materials irradiated with 185 MeV Xe ions requires the production of both anti-Frenkel pairs and high energy Frenkel pairs (*i.e.* the displacement of both anions and cations). This is consistent with the higher energy densities produced by irradiation with these ions of relatively low velocity.

With the atomistic processes controlling the irradiation-induced C-to-B transformation identified, the observed compositional dependence of the transformation can be understood on the basis of the relationship between composition, defect formation, and the transformation mechanism. As has been established, this transformation is driven by the production of anion vacancies via the displacement of 48*e* oxygen to the 16*c* site. Thus, the transformation rate, as a function of ion fluence, should depend on the efficiency of both anti-Frenkel pair formation and the C-to-B transformation mechanism. Atomistic simulations have shown minimal variation in the anti-Frenkel formation energy of Ln_2O_3 materials across the lanthanide series [150]. However, this value expresses only the difference in lattice energy between the pre- and post-defect formation states, and does not account for the dynamic nature of atomic displacement or

the associated energy barriers. The threshold displacement energy accounts for these parameters, but such values have not been determined for compositions across the lanthanide series. However, trends in the ease of anion displacement can be predicted through analysis of related materials properties. The packing of atoms in these materials becomes more efficient as the ionic radius of the lanthanide cation decreases. Atomic packing factors vary from monotonically from 0.43 for Sm_2O_3 to 0.47 for Lu_2O_3, based on reported unit cell parameters [91] and ionic radii [160]. As the amount of "empty" space within a material decreases, greater structural distortion, and therefore greater energy, is required for atomic displacement to occur. *Ab initio* calculations [120,161] and experiments [124,125] show that this improved packing is concomitant with an increase in bulk modulus, which represents the resistance of a material to structural distortion. Calculations show that the Ln-O bond covalency increases [120,162], and the Ln_2O_3 lattice energy decreases [152,163], with lanthanide atomic number, with the latter result supported by calorimetric measurements [164]. Shifts in the frequency of Raman-active vibrational modes indicate an increase in the Ln-O force constant with increasing lanthanide atomic number [144]. These changes indicate stronger bonding across the lanthanide series, meaning improved resistance to the bond breaking associated with atomic displacement. Finally, oxygen mobility decreases rapidly across the lanthanide series [91]. Together, these trends suggest that the formation of anti-Frenkel pairs through oxygen displacement becomes much less energetically favorable as the ionic radius of the lanthanide cation in an Ln_2O_3 material decreases.

Similar to this variation in the efficiency of irradiation-induced anti-Frenkel pair formation with lanthanide sesquioxide composition, the formation of a B-type structure is inhibited by a decrease in the ionic radius of the lanthanide cation. The C-to-B transformation involves an increase in the anion coordination of cations from a six-fold distorted octahedron to a

seven-fold monocapped octahedron. From Pauling's first rule [165], the stability of a cation coordination polyhedron is governed in large part by the cation-anion ionic radius ratio, r_{cation}/r_{anion}. As the cation radius decreases, as occurs across the lanthanide series, the coordinated anions must move closer to one another, increasing anion-anion repulsion and lattice energy. Thus, the B-type seven-fold coordination of lanthanide cations by oxygen becomes less stable for smaller lanthanide elements, making the C-to-B transformation less energetically favorable, as is consistent with the positive slope of the equilibrium transformation temperature, as a function of lanthanide ionic radius (Figure 12). Measured transition enthalpies are in agreement with this assessment, as they increase from 3.8 ± 2.6 kJ mol^{-1} for Sm_2O_3 to 16.691 kJ mol^{-1} for Lu_2O_3, as reported by Zinkevich [116]. For a sufficiently small cation, the increased Coulomb energy of the seven-fold coordination will render the B-type phase unstable, explaining why it is not observed as a polymorph for compounds with lanthanides of higher atomic number than Er (see Figure 12). Consequently, the irradiation-induced C-to-B transformation was not observed for Tm_2O_3 or Lu_2O_3 in this work. Similar behavior has been observed in C-type Ln_2O_3 materials irradiated with light ions of low energy, for which elastic nuclear collisions are the dominant process of energy transfer to the material. Irradiation with 30 keV O ions induces a C-to-B transformation in Gd_2O_3, but Er_2O_3 retains its C-type structure under these conditions [136]. Similarly, irradiation with 300 keV Kr ions induces the same transformation in Dy_2O_3 and Er_2O_3, while Lu_2O_3 retains its C-type structure [135].

Similar swift heavy ion irradiation-induced crystalline-to-crystalline phase transformations have been previously observed in a small number of materials. Monoclinic ZrO_2 and HfO_2 transform to a tetragonal high-temperature polymorph in response to irradiation in the electronic excitation regime [13,166–168]. The polymorphic monoclinic-to-tetragonal

transformation in these materials is driven by the displacement of oxygen atoms [169,170], occurring once a critical oxygen vacancy concentration is achieved [171,172]. Large concentrations of oxygen vacancies have been observed in irradiated ZrO_2 [11,173]. Formation of the tetragonal polymorph also involves an increase in the coordination of cations by oxygen. In these respects, this transformation is analogous to the C-to-B transformation observed in this investigation.

3.3.2 C-to-X transformation

With the C-to-B transformation rendered energetically inaccessible to the lanthanide sesquioxides with small cations, and the high bond strength and structural rigidity of these compounds preventing amorphization, these materials slowly transform to a non-equilibrium X-type phase. The sluggish nature of this transformation is indicated by the very small ion track radii extracted from fitting of the phase fraction data to Eq. 1, indicating that each impinging ion forms only a very small volume of the X-type phase. This suggests a large kinetic barrier to the displacement of atoms and the C-to-X transformation in these materials, consistent with the above analysis of the composition dependence of the lanthanide sesquioxides' radiation response. Furthermore, there exists no obvious relation between the C-type and X-type structures, as has been demonstrated for the C-type and B-type structures. This precludes the occurrence of a facile transformation mechanism, like that of the C-to-B transformation. Therefore, the C-to-X transformation likely requires the displacement of both anions and cations (*i.e.* both Frenkel and anti-Frenkel pair formation).

This dependence of the C-to-X transformation on the formation of defects on both the cation and anion sublattices contrasts with that of the C-to-B transformation, explaining the differing dependence on ion beam velocity of the two processes. The X-phase formed most

rapidly under irradiation with 185 MeV Xe ions (see Figure 19), which produce relatively high in-track energy densities suitable for the displacement of anions and cations. Under irradiation with 2246 MeV Au ions, which produce lower energy densities, only very small X-type phase fractions (< 1%) were produced at the highest ion fluence achieved. This is consistent with the conclusion that these energy densities are too low to cause extensive cation displacement and instead cause primarily anti-Frenkel pair formation. These defects cannot cause a C-to-B transformation in compounds with lanthanide cations of low ionic radius and are not sufficient for the cation sublattice reordering characteristic of a C-to-X transformation. Thus, under these conditions Tm_2O_3 and Lu_2O_3 largely retained the C-type structure (see Figure 17).

This is, to the authors' knowledge, the first reported observation of an X-type phase of Tm_2O_3 or Lu_2O_3 and is the first reported instance of the recovery of an X-type Ln_2O_3 phase to ambient conditions. Previously, Lang *et al.* produced a material with a similar structure from the compound $Gd_2Zr_2O_7$ via irradiation with swift heavy ions at a very high pressure of ~40 GPa [174]. This material had an initial pyrochlore structure, which is an anion-deficient derivative of the fluorite structure, much like the C-type bixbyite structure. While this irradiation- and pressure-induced phase shares a body-centered cubic cation sublattice with the Ln_2O_3 X-type phase, its anion sublattice likely differs due to the differing stoichiometry of pyrochlore- and bixbyite-structured compounds. Unlike the C-to-X transformation observed in this investigation, the pyrochlore compounds did not form the X-type-like phase under irradiation at ambient pressure.

The stabilization of an X-type phase at ambient conditions is of particular interest due to the ionic conductivity of this phase. The very low occupancy of the X-type anion sublattice (between 12.5% and 50%, depending on the site occupied by the anions) means that there are

many paths along which oxygen can migrate with small energy barriers. Consequently, Aldebert *et al.* have measured very high ionic conductivities in X-type La_2O_3 at high temperatures [118]. Based on the damage accumulation behavior observed here, the C-to-X transformation should be complete following irradiation with 185 MeV Xe ions to a fluence on the order of $\Phi = 1 \times 10^{14}$ ions cm^{-2}. This would allow for the measurement, for the first time, of the ionic conductivity of this phase at temperatures below 2400 K.

3.4 Conclusions

Dense, transient electronic excitations in C-type lanthanide sesquioxides induced various phase transformations, with the final phase formed showing dependence on the lanthanide element present in the sesquioxides, as well as the energy densities generated. For sesquioxides with cations of atomic number less than Tm, a transformation to the B-type monoclinic phase was observed. This transformation was dominant in materials irradiated with 2246 MeV Au ions, but was accompanied by extensive amorphization during irradiation with 185 MeV Xe ions. For sesquioxides with heavier lanthanides, a non-equilibrium X-type phase was produced. This transformation occurred more rapidly, as a function of ion fluence, for the 185 MeV Xe irradiation, as compared with the 2246 MeV Au irradiation. The C-to-B transformation proceeds via a mechanism driven by the production and aggregation of anion vacancies, while amorphization and the C-to-X transformation require the displacement of both anions and cations in significant quantities.

The composition dependence of the phase responses of these materials to irradiation arises from the decreasing energetic favorability of both point defect formation and the C-to-B transformation across the lanthanide series. The C-to-X transformation occurs only when the formation of the B-type phase is energetically inhibited, due to the large ionic radius of the

lanthanide cations present in an Ln_2O_3 material. The dependence of both transformations on the mass and energy of the accelerated ions is caused by the inverse proportionality between ion velocity and the density of energy deposition to the material. Thus, the transformations that require the formation of both Frenkel and anti-Frenkel defects (C-to-X and C-to-amorphous) occur preferentially during irradiation with the ion of relatively low mass and energy, while the transformation that requires exclusively anti-Frenkel pair formation (C-to-B) occurs preferentially during irradiation with the ion of relatively high mass and energy. The phase space of the lanthanide sesquioxides under the extreme conditions produced by swift heavy ion irradiation are related to the equilibrium high-temperature phase space of these materials, but differs in many respects due to the unique kinetics associated with the relaxation of a material from a state of warm dense matter. This allows for the formation and recovery to ambient conditions of non-equilibrium phases, such as X-type Tm_2O_3 and Lu_2O_3, not accessible under conventional processing conditions. Due to their chemical and structural similarity, related phase behavior is likely to occur in the heavy actinide sesquioxides.

Chapter 4

Swift heavy ion irradiation of AnO_2 and related materials: irradiation-induced redox reactions

In contrast to the behavior of the lanthanide elements most actinides, in addition to cerium, praseodymium, and terbium, can adopt tetravalent or higher oxidation states (see Figure 7). This allows them to form, for example, dioxides and trioxides. The most common compound of the *f*-block oxides after the sesquioxide (Ln_2O_3 or An_2O_3), is the dioxide (LnO_2 or AnO_2). All *f*-block dioxides adopt a fluorite structure (see Figure 8). Unlike the sesquioxides, they exhibit no high temperature polymorphism, instead retaining the fluorite phase to their melting temperatures. Due to the exceptional stability of this phase for oxides of the tetravalent *f*-block elements, irradiation-induced phase transformations are precluded. In previous studies of the radiation response of fluorite-structured CeO_2 [29,30,175–179], ThO_2 [31] and UO_2 [33,180–182] irradiated with swift heavy ions, these materials were shown to maintain their fluorite structures at any ion fluence, exhibiting only limited structural distortions within ion tracks.

Most *f*-block elements with tetravalent oxidation states also exhibit stable trivalent states. This is of particular relevance to the behaviour of these materials under swift heavy ion irradiation, as partial reduction of cerium in irradiated CeO_2 to the trivalent state has been previously demonstrated by x-ray photoelectron spectroscopy [175,183]. Thus, for these materials, which lack structural variability but possess cation valence variability, the systematics of the swift heavy ion irradiation response can significantly differ from those of the sesquioxides. It is important for these materials to compare any changes to the atomic structure, such as unit

cell expansion or microstrain, to changes of the electronic configurations of cations, in order to elucidate possible coupling between the two. Investigation of the behavior of actinide oxides and related materials under swift heavy ion irradiation is also necessary for the development of advanced, radiation tolerant nuclear fuels.

In studies of the effects of swift heavy ions irradiation on insulating materials, it is generally assumed that electron-hole recombination leads to recovery of the pre-irradiation charge distribution [5] but, given the highly non-equilibrium conditions under which relaxation of the electron cascade occurs, electronic structure modifications are possible. The *f*-block dioxides and trioxides are an ideal system for studying the influence of cation electron capture and associated redox changes on a material's radiation response, as they exhibit substantial variation in accessible valence states with changing composition. The reduction of Zr^{4+} to Zr^{3+} has been shown [184] to accompany a radiation-induced phase transformation in $Sc_4Zr_3O_{12}$ [185], suggesting that irradiation-induced redox behavior might have some effect on the accumulation of structural damage. Any relationship between radiation tolerance and redox behavior would have important implications for the technologically important light actinide (Th-Cm) oxides, as their partially delocalized 5*f* orbitals cause significant variation in the accessible stable electronic configurations across this series [89].

Motivated by the potential influence of their complex chemistry on the radiation response of the *f*-block dioxides and trioxides, several of these materials were systematically irradiated with 167 MeV Xe ions, similar in mass and energy to fission fragments, and 950 MeV Au ions. CeO_2, ThO_2, UO_3, and hydration products of the uranium oxides were studied. Thorium and cerium are both nominally one *f*-electron elements and possess dioxides isostructural with those of all light actinides, yet they possess contrasting solid state chemistry. The cation in ThO_2, a

proposed nuclear fuel component used for the breeding of uranium, does not adopt a trivalent oxidation state , while the cerium in the actinide analogue CeO_2 is easily reduced from the tetravalent state to the trivalent state, similar to the behavior of PuO_2. Finally, UO_3 and its room temperature hydration products, $(UO_2)(OH)_2$ (α-uranyl hydroxide) and $(UO_2)_4O(OH)_6(H_2O)_5$ (metaschoepite), feature hexavalent uranium that can be reduced in valence by multiple steps to the tetravalent oxidation state [186]. They are common oxidation/hydrolysis products of the nuclear fuel UO_2, and are produced by fuel-coolant interactions and groundwater exposure of fuel [187].

These experiments showed evidence of coupling between radiation-induced redox behavior and structural modifications, with materials that undergo cation valence state changes exhibiting damage accumulation behavior distinct from those that are resistant to such chemical modification. In redox-active materials, control of the efficiency of these radiation-induced redox processes through, for example, grain size modification, can be used to tailor the susceptibility of a material to radiation damage. These results are particularly important for the light actinide oxides as, due to the partially-itinerant nature of their 5*f* electrons, they exhibit increasing variability in stable electronic configurations across the actinide series (as the 5*f* orbitals are filled). This results in systematic variation in their radiation tolerance. These results also yield new insight into the mechanisms by which highly-ionizing radiation produces damage in nuclear fuel materials and demonstrate potential for the design of radiation tolerant materials through control of their redox behavior.

4.1 Experimental Methods

Powders of CeO_2, ThO_2, UO_3, and a mixture of $(UO_2)(OH)_2$ and $(UO_2)_4O(OH)_6(H_2O)_5$ were pressed into holes of 200 μm diameter in thick stainless steel sheets of 12.5 μm and 50 μm

thickness. Nanocrystalline CeO_2, in the form of spherical nanocrystals, was procured from MTI Corporation and was synthesized from cerium ammonia nitrate using a hydrothermal process. The uranium oxyhydroxide material was produced by exposure of γ-UO_3 to humid air for several years and contains a minor amount (<2%) of the oxide precursor phase. Typical grain sizes were on the order of a few μm for the microcrystalline samples and 20 nm for nanocrystalline samples. The resulting compacts were 50-60% theoretical density. Irradiation of the 50 μm thick samples in vacuum, at room temperature, with 950 MeV Au ions was carried out at beamline M2 of the UNILAC linear accelerator at the GSI Helmholtz Centre for Heavy Ion Research in Darmstadt, Germany. Samples were irradiated to fluences of up to 5×10^{13} cm^{-2}, with the ion flux limited to ~10^9 $cm^{-2}s^{-1}$ to avoid heating of the samples. Irradiation of the 12.5 μm thick samples with 167 MeV ^{132}Xe ions was carried out under the same conditions using the IC-100 cyclotron at the Joint Institute for Nuclear Research in Dubna, Russia, to fluences of up to 1×10^{14} cm^{-2}. The ranges and stopping powers of these ions in the samples were calculated using the SRIM code [34], correcting for the low densities of the samples [131]. In all cases, the projected ranges were greater than the sample thickness, indicating that all ions passed completely through the samples and were not implanted. For all samples, the electronic energy loss was several orders of magnitude greater than the nuclear energy loss for the majority of the ion path, and remains greater throughout the entire sample. However, significant variation in both the electronic and nuclear energy loss exists across the ion paths, particularly for the Xe ion irradiations. In order to simulate the damage produced in nuclear material by ionizing fission fragments, sample dimensions were selected such that damage across the majority of the ion tracks could be probed, while excluding the end-of-range regions in which nuclear collisions dominate. Thus, the extent of damage measured is averaged over the majority of the ion path, to account for variation in ion

energy loss as the ion is slowed and to obtain data that are directly relevant to the specific modification of a nuclear fuel material by fission fragments.

The structures and electronic configurations of irradiated and unirradiated samples were investigated by means of synchrotron x-ray diffraction and synchrotron x-ray absorption spectroscopy, both performed in transmission geometry. In this geometry, the entirety of the ion tracks in a given sample are probes simultaneously, such that the signal obtained is averaged over the entire sample depth and is representative of the total damage caused by fission fragments in the electronic stopping regime. Angle dispersive XRD was performed at beam line HPCAT 16BM-D of the Advanced Photon Source at Argonne National Laboratory. A monochromatic beam of 25 keV (λ = 0.4959 Å), selected using a Si (111) double crystal monochromator with a focused spot size of 12 μm (v) × 5 μm (h) in the full width at half maximum, was used in transmission geometry and diffraction rings were recorded with a Mar345 image plate detector. A collection time of 300 s and a photon flux on the order of 10^9 s^{-1} was used for all diffraction patterns. Unit cell parameters were determined by full XRD pattern refinement using the Rietveld method with the software Fullprof [142] and microstrain was determined using Williamson-Hall analysis [112]. In the latter method, the broadening of all peaks, expressed as integral breadths, were measured and instrumental broadening was subtracted to obtain the radiation-induced x-ray line broadening (the increase in integral breadth relative to the intrinsic instrumental peak breadth). The angular dependences of these peak breadths were fit using a convolution of the models for strain (β_{strain}) and crystallite size (β_{size}) broadening:

$$\beta_{strain} = 4\varepsilon \tan\theta \tag{5}$$

$$\beta_{size} = \frac{0.9\lambda}{t\cos\theta} \tag{6}$$

where β is the peak breadth after correction for instrumental broadening, ε is the heterogeneous microstrain, θ is the diffraction angle of a given peak, λ is the x-ray wavelength, and t is the mean linear dimension of a crystallite. Due to their distinct angular dependences, these two contributions could be distinguished and quantified. Phase proportions in the uranyl hydrate mixture were determined by Rietveld refinement.

Transmission XAS at the Ce K-edge, Th L_{III}-edge, and U L_{III}-edge were measured immediately after the diffraction measurements without changing the beam spot on the sample or the experiment geometry. HPCAT 16BM-D's fixed-exit beam monochromator (Si (111) double crystals in pseudo channel cut mode) and switchable diffraction-absorption setup allowed consistent measurement of the two properties at an identical sample condition. Analysis of the XAS spectra was performed using the software DATLAB [188] and the XAS edge energies were defined as the inflection points of the edges (i.e. the zero of the second derivative).

The influence of defect accumulation on the local structure and phonon modes of these materials was characterized by Raman spectroscopy. A confocal Horiba Jobin Yvon HR800 system with a 20nW He-Ne laser was used, with an excitation wavelength of λ = 632.8 nm to minimize photoluminescence signal. A diffraction grating with 1800 grooves/mm provided a spectral resolution of approximately 0.01 nm. Multiple spectra were collected from randomly selected areas of each sample, with a laser spot size of approximately 1 μm^2. Each measurement was performed for 60 s, and each final spectrum was averaged over three measurements to reduce noise.

4.2 Results

4.2.1 Defect accumulation in ThO_2

Irradiation of ThO_2 with swift heavy ions induced only minor structural modifications (Figure 24a,b). XRD patterns corresponding to both ion beam conditions displayed a shift in the fluorite-structure diffraction maxima to lower 2θ angles, signifying an increase in the unit cell parameter, and broadening of the peaks due to the accumulation of heterogeneous microstrain. The latter effect was quantified via the use of Williamson-Hall analysis [112], in which microstrain and crystallite size contributions to peak breadth are differentiated based on the angular dependence of broadening. No contribution to broadening from a decrease in crystallite size was observed, consistent with previous work that has shown grain growth to result from irradiation of fluorite materials in the electronic stopping regime [189]. Therefore, the increased breadth of the diffraction peaks can be attributed solely to microstrain. Together, these peak shifts and broadening are consistent with the accumulation of defects that distort the local periodicity of the atomic structure. Both unit cell expansion and microstrain can be produced by the same defects, such as Frenkel pairs. The former indicates long-range changes in the periodicity length of lattice planes due to the additional volume occupied by these defects, while the latter results from heterogeneous, short-range distortion in the spacing of planes in the local environment of defects.

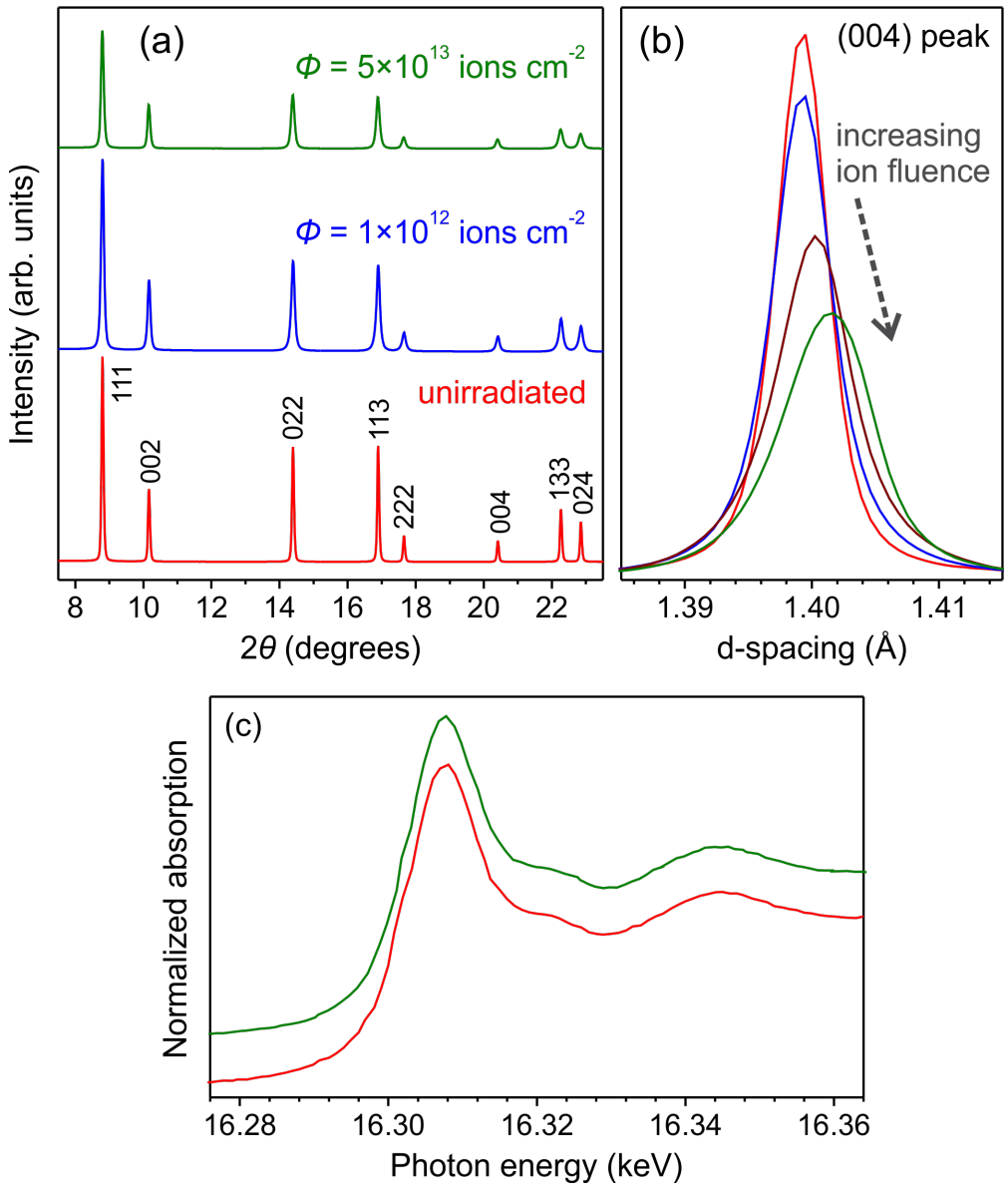

Figure 24: (a,b) XRD patterns of ThO_2 irradiated with 950 MeV Au ions as a function of ion fluence, Φ. The fluorite structure diffraction maxima exhibit both an increase in width and a shift to lower 2θ values with increasing fluence, as illustrated by the dashed lines. These changes indicate the presence of strain and unit cell volume expansion, respectively. (c) No significant changes are apparent in the XAS spectra, indicating that thorium remains in a tetravalent oxidation state.

Figure 25 shows refined unit cell parameter expansion, $\Delta a/a_0$, and average microstrain, ε, for ThO_2 as a function of ion fluence for both ion beam conditions. The evolution of these parameters is consistent with a single-impact model of damage accumulation, given in Eq. 1

[146]. This model of damage accumulation yields an initial linear relationship between radiation damage and ion fluence, corresponding to well-separated ion tracks in which structural modification has occurred, followed by saturation with increasing track overlap. For both irradiation conditions, the slopes of the initial linear regions, which are proportional to the ion track cross-sectional area, are greater for microstrain than for unit cell expansion. This indicates ion track heterogeneity due to a decreasing defect density along the radial track direction [3,31]. The energy density deposited by a swift heavy ion exhibits similar radial decay, such that defect production is most efficient in the track core. Here, the damage is sufficient to induce an increase in the average spacing of atomic planes over medium-range length scales, along with significant microstrain. In contrast, the more isolated defects present in the track shell region cause primarily local structural distortion, or microstrain, resulting in a larger effective track diameter for this modification. Track diameters extracted from fitting of a single impact model to the data are $d_{\text{cell expansion}} = 3.0 \pm 0.1$ nm and $d_{\text{microstrain}} = 3.2 \pm 0.3$ nm for the 167 MeV Xe irradiations, while the 950 MeV Au irradiations yielded $d_{\text{cell expansion}} = 6.1 \pm 0.4$ nm and $d_{\text{microstrain}} = 10.2 \pm 0.9$ nm.

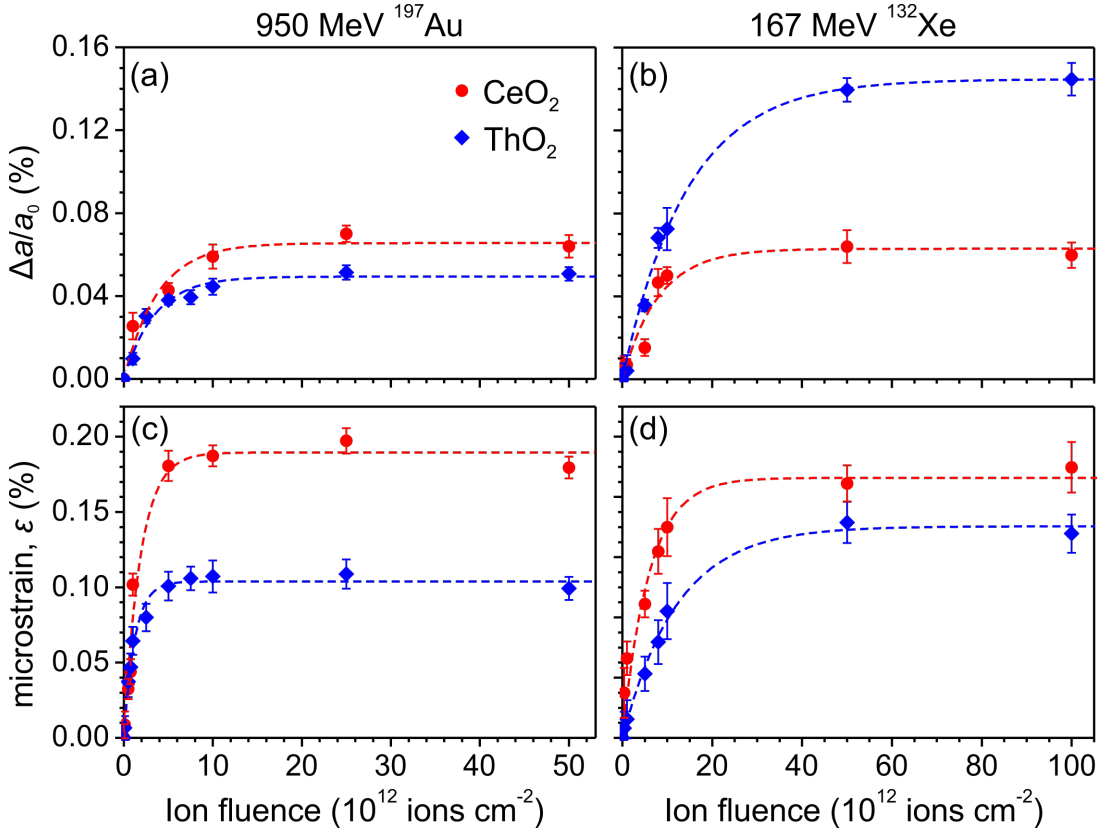

Figure 25: The volume expansion (a,b) and heterogeneous microstrain (c,d) measured in irradiated ThO_2 and CeO_2. Both the unit cell parameter expansion, $\Delta a/a_0$, and the heterogeneous microstrain, ε, present in each material increase with ion fluence. This increase is initially linear, but saturates as ion track overlap occurs. The saturation damage shows strong dependence on ion specific energy for ThO_2, but is relatively constant for CeO_2. The dashed lines corresponds to fits of the data to a single-impact model (Eq. 1) and the error bars represent the standard deviation of unit cell expansion and microstrain values determined from multiple samples irradiated to the same ion fluence.

Comparison of the damage induced by the two ion beams used in this work indicates increased track size for the high specific energy ion, but a significant decrease in the saturation unit cell volume expansion and strain. This is consistent with the ion velocity effect, wherein a decrease of the energy and mass of impinging particles can lead to enhanced damage efficiency within smaller ion tracks, due to more compact electronic energy deposition volumes. For example, Meftah *et al.* [159] have shown that mean in-track energy densities produced by 185 MeV Xe ions in $Y_3Fe_5O_{12}$ are more than double those produced by 2.5 GeV Pb ions, a trend

similar to that seen here. Because the magnitude of the structural damage quenched into ion tracks in ThO_2 depends on the amount of energy available to displace atoms and produce point defects, the decreased spatial extent of energy deposition by the Xe ions, as compared with Au, results in enhanced damage production within smaller ion tracks. Saturation of the unit cell parameter expansion and microstrain for the Xe irradiations occur at 0.145 ± 0.004% and 0.141 ± 0.003%, respectively, while those for the Au irradiations occur at 0.049 ± 0.002% and 0.107 ± 0.003%. XAS spectra of the Th L_{III}-edge (Figure 24c) confirm that thorium remains in the tetravalent oxidation state following irradiation, as expected. Trivalent thorium compounds are rare and are unknown in the Th-O system [190]. Minor modification of features in the pre-edge region may be present, but the resolution obtained is not sufficient for analysis. Such features arise from electron transitions to bound states and are sensitive to the local environment of absorbing atoms, such that thorium Frenkel defects are a likely cause of any changes in this region of the spectra.

Raman spectroscopy results were consistent with the identification of point defect formation as the source of irradiation-induced structural modifications of this material. Spectra of the unirradiated sample (Figure 26) showed only a single vibrational mode at approximately 465 cm^{-1}, in agreement with previous measurements [191]. This band is attributed to the triply degenerate T_{2g} vibration. Its intensity is significantly reduced with increasing ion fluence, indicating distortion of the structure accompanying the displacement of atoms from their equilibrium lattice sites, which suppresses this vibrational mode. The only other observed modification to the spectra is the growth of a broad band or of multiple overlapping bands in the range ~500-660 cm^{-1}. Guimbretière *et. al.* [192] observed similar Raman signals in approximately this range for fluorite-structured UO_2 irradiated with 25 MeV He ions, for which,

as with the ions used in this study, the energy loss is primarily electronic. They attributed this signal to the influence of defect-activated modes, including the Raman-forbidden LO mode [193]. This optical phonon mode has previously been observed in UO_2 irradiated with 200 keV Kr ions, which cause damage to a material through elastic nuclear collisions, and has been shown to indicate a breakdown in the selection rules of fluorite materials due to structural damage accompanying irradiation-induced defect production [194]. Therefore, the appearance of a broad band in the Raman spectra of irradiated ThO_2 centered around 575 cm^{-1} and the reduction in the intensity of the T_{2g} mode both confirm the accumulation of structural distortion with increasing fluence, resulting from the production of point defects or defect agglomerates.

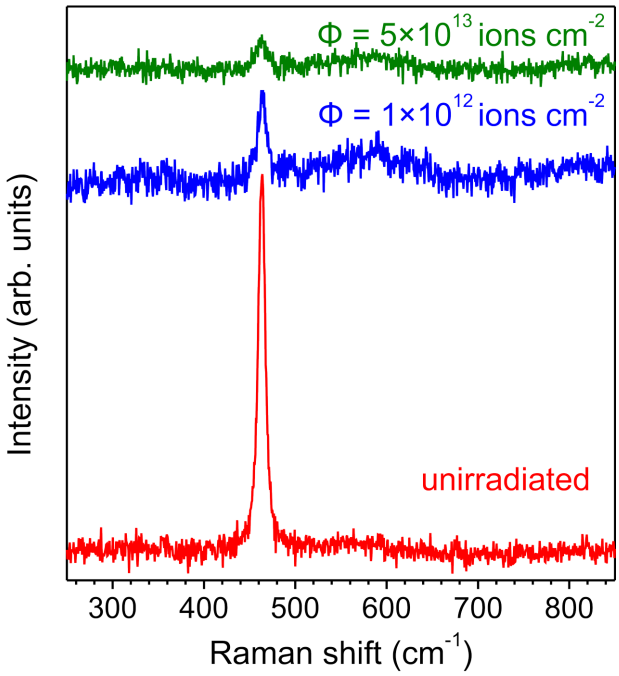

Figure 26: Raman spectra of irradiated and unirradiated ThO_2. A pronounced decrease in the intensity of the T_{2g} mode at approximately 465 cm^{-1} is observed with increasing fluence, indicating the presence of structural distortion resulting from defect accumulation. As the intensity of this mode decreases, a broad, weak peak centered at ~575 cm^{-1} grows.

4.2.2 Redox response of CeO_2

CeO_2 exhibits a structural radiation response qualitatively similar to that of ThO_2, but a dramatically different dependence of saturation damage on ion mass and energy (Figure 25). Again, XRD peak shifts indicated unit cell expansion, while peak broadening indicated the accumulation of heterogeneous microstrain. No decrease in the crystallite size was observed in the Williamson-Hall analysis, such that broadening can be attributed solely to microstrain. The evolution of unit cell expansion and microstrain both follow single-impact behavior and exhibit ion track diameters of $d_{\text{cell expansion}} = 3.9 \pm 0.3$ nm and $d_{\text{microstrain}} = 4.6 \pm 0.5$ nm for the 167 MeV Xe irradiations, with $d_{\text{cell expansion}} = 5.8 \pm 0.6$ nm and $d_{\text{microstrain}} = 8.4 \pm 0.7$ nm for the 950 MeV Au irradiations. Saturation of the cell expansion and microstrain occur for the Xe irradiation at $0.063 \pm 0.004\%$ and $0.172 \pm 0.009\%$, respectively, and at $0.066 \pm 0.004\%$ and $0.192 \pm 0.007\%$ for the Au irradiation. This relatively constant unit cell parameter expansion agrees well with that reported by Ohno *et al.* [175] of 0.06% for irradiation with 200 MeV Xe ions. Clearly, the energy and mass of swift heavy ions have little effect on the efficiency of in-track damage evolution in this material, suggesting a damage production mechanism fundamentally different from the defect accumulation process active in ThO_2. This unique radiation response is further demonstrated by XAS spectra of the Ce K-edge, shown in Figure 27, which confirm the partial reduction of cerium to its trivalent state, as demonstrated by a shift in the edge to a lower energy following irradiation. This is evidence of a decreased core electron binding energy concomitant with decreased charge of the cation. The roughly 2 eV edge shift, which also does not vary significantly between the two ions, indicates partial reduction, as a complete reduction of all Ce^{4+} to Ce^{3+} corresponds to a 7 eV shift [195]. Previous studies [175,183] of CeO_2 irradiated with 200

MeV Xe ions have demonstrated similar oxidation state changes using x-ray photoelectron spectroscopy.

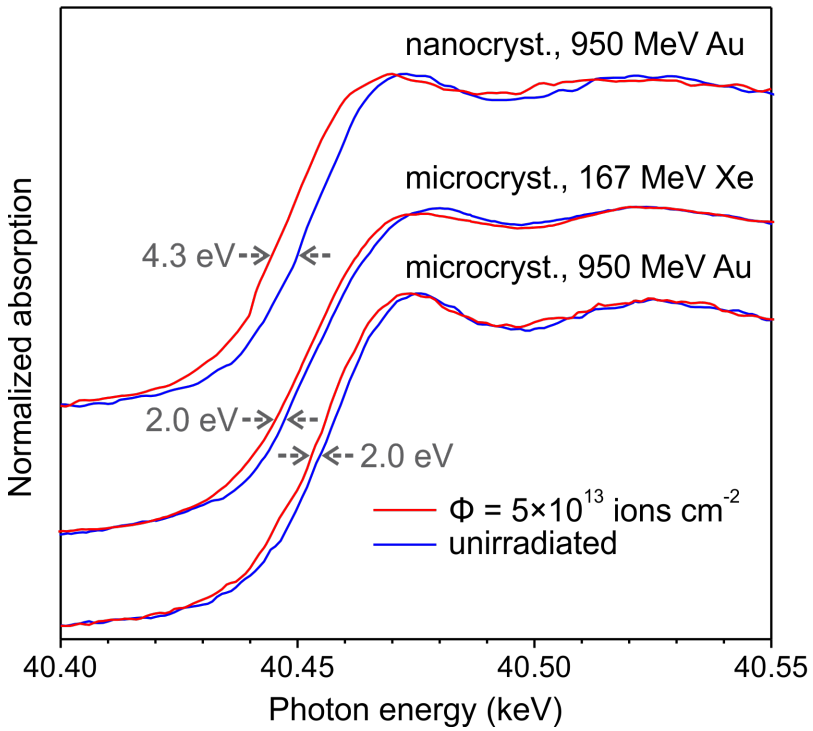

Figure 27: XAS of the Ce K-edge measured before and after ion irradiation. Following irradiation to a fluence of 5×10^{13} cm^{-2}, the absorption edges shift to lower energies, indicative of partial reduction of cerium from the tetravalent to the trivalent oxidation state. Minimal dependence of the edge shift on ion mass or energy is evident. Under identical irradiation conditions, nanocrystalline CeO_2 exhibits more extensive cation reduction than microcrystalline CeO_2.

The reduction of cerium alone, without concurrent Frenkel defect accumulation, has been shown to result in structural modifications identical to those observed here [196,197]. As large Ce^{3+} cations (ionic radius = 1.14 Å) replace Ce^{4+} (ionic radius = 0.97 Å) [160], the fluorite unit cell expands and the distribution of atoms of different ionic radii on the cation sublattice causes local structural distortion. Additional unit cell expansion arises from a decrease in the electrostatic attraction between cations and anions accompanying the reduction of cerium's charge. Therefore, the radiation-induced structural modifications to CeO_2 shown in Figure 25 must be at least partially attributed to the effects of the observed cerium valence reduction.

Comparison of quantitative unit cell expansion and valence reduction data by Iwase *et al.* [183] indicated that the expansion induced in CeO_2 by ions in the electronic stopping regime can be attributed almost entirely to this redox effect. The lack of a significant influence of ion mass and energy on the extent to which cerium is reduced to the trivalent state explains the constant damage saturation in this material and further suggests that this redox effect is the primary cause of the observed structural modifications. The saturation of cerium reduction may be related to the efficiency of electron capture by this element's *f*-orbitals during relaxation of the electron cascade. This mechanism of structural modification by swift heavy ion irradiation is illustrated in Fig. 28.

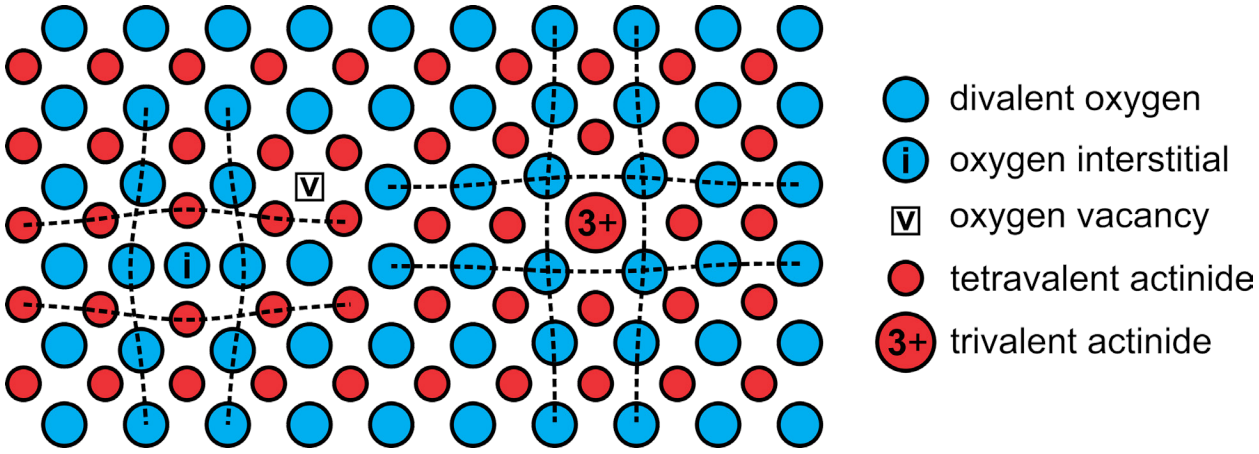

Figure 28: A schematic diagram of the two sources of irradiation-induced structural distortion identified here: point defect formation and cation valence reduction. On the left, an anion has been displaced to an interstitial site, producing a Frenkel pair. The atomic structure is distorted around the constituent vacancy and interstitial defects. This is the dominant mode of damage in ThO_2, which has a non-multivalent cation. On the right, a cation has been reduced in oxidation state, concomitant with an increase in ionic radius. This produces local distortions of the atomic structure similar to those cause by defect production. This irradiation-induced redox behavior is the dominant mode of damage in CeO_2, due the accessibility of a trivalent state of this compound's cation.

Raman spectroscopy data obtained from irradiated CeO_2 are consistent with this interpretation of a primarily redox-driven radiation response in this material, distinct from that of ThO_2. As shown in Figure 29, the spectra corresponding to CeO_2 show no evidence of defect-

induced Raman modes, as were evident in irradiated ThO_2 (see Figure 26). This is associated with a relatively minor influence of point defects or defect agglomerates on the irradiation-induced structural distortions. Instead, they arise primarily from distortions associated with partial valence reduction of cerium, such that attenuation of the initial T_{2g} band is still apparent.

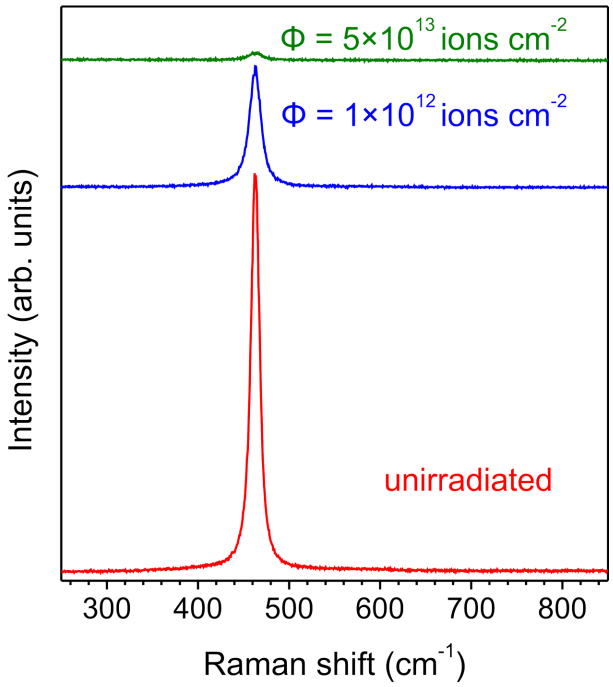

Figure 29: Raman spectra collected from CeO_2 both before and after irradiation. At all ion fluences, the sample exhibits only a single, T_{2g} vibrational mode, consistent with a fluorite structure. With increasing ion fluence, the intensity of this mode decreases significantly.

The modified electronic structure observed in CeO_2 ion tracks requires accompanying modification of the atomic structure to maintain charge neutrality, as the oxygen coordination of Ce^{3+} must be lower than that of Ce^{4+} in unirradiated CeO_2. Takaki *et al*. [178], using advanced scanning transmission electron microscopy (STEM) techniques, have demonstrated a decrease in the atomic density of ion track core regions of CeO_2 irradiated with 200 MeV Xe ions. The 4 nm diameter of this modified region is much smaller than the 17 nm track diameter identified using conventional TEM analysis [198], but is close to the ~4-6 nm track diameters measured by XRD in the present work. They attribute this track size discrepancy to the production of a small,

vacancy-rich track core (visible in STEM micrographs) surrounded by a large, interstitial-rich track shell (observed with conventional TEM). Comparison of these STEM results with x-ray photoelectron spectroscopy and extended x-ray absorption fine structure studies [175,183] of irradiated CeO_2 indicate that the segregation of defects occurs preferentially on the oxygen sublattice, resulting in a hypostoichiometric track core and a hyperstoichiometric shell. Consistent with the results reported here, this suggests that damage accumulation in this redox-active material is driven by concurrent cation valence changes and anion-specific Frenkel pair formation, a process distinct from that of non-reducible ThO_2. Similar oxygen-selective point defect production has been observed in CeO_2 irradiated with electrons [199–201], which deposit energy through isolated electron excitation, confirming that the formation of these ion tracks is an effect of ionization. In this work, clusters of interstitial oxygen were observed, indicating that anions preferentially displaced by ionizing radiation tend to aggregate in planar interstitial dislocation loops [200], which have been identified as a possible cause of problematic microstructure changes in the rim region of nuclear fuel pellets [202].

A process analogous to the redox effect of highly-ionizing radiation on CeO_2 can be found in the radiation response of the alkaline earth halides. Under high-energy, heavy ion irradiation, fluorite-structured CaF_2 forms nanoscale metallic inclusions within the track cores due to anion-specific expulsion of atoms from the particle-solid interaction volume following the formation of mobile interstitial fluorine [17,203]. Similar behavior, which indicates complete valence reduction of the cations, has been observed in SrF_2 and BaF_2 under ionizing radiation [204]. Planar defects, likely composed of interstitial anions, were observed in the track shell regions, and TEM analysis [205] has shown the presence of strain around ion tracks, caused by the volume expansion that accompanies the track core redox effect. The saturation of damage in

CaF_2 seems to be related to its redox chemistry, with electron radiation damage accumulation ceasing once 5-10% of the material has been fully reduced to metallic Ca, regardless of the irradiation conditions [204]. This is consistent with the constant saturation damage and cerium reduction observed in CeO_2, for which the same coupling of radiation-induced redox behavior with structural damage, in the form of lattice distortion, is observed. Cation valence reduction by ionizing radiation is further evident in the fluorite materials ZrO_2 [11] and UO_2 [192], while Al_2O_3 has been shown to undergo both reduction [206] and anion-selective defect accumulation [207]. Anion segregation, accompanied by chemical reduction, has also been observed in Al_2O_3 irradiated with an ultrafast laser [208] which, like high-energy heavy ions, deposits energy in a material via electronic excitation. Taken together, these results suggest that the redox mechanism proposed here represents a fundamental response of ionic compounds to electronic excitation.

4.2.3 Enhanced reduction of nanocrystalline CeO_2

If damage accumulation in CeO_2 is controlled largely by this material's redox behavior, its radiation response should exhibit a strong dependence on grain size, since the presence of high-energy surfaces dramatically enhances the redox activity of CeO_2 [209]. To test this hypothesis, nanocrystalline CeO_2 with an average crystallite size of 20 nm was irradiated. Figure 27 shows an irradiation-induced Ce K-edge shift of 4.3 eV for the nanocrystalline material, more than twice that of microcrystalline powder. This confirms the occurrence of more extensive cation valence reduction, accompanied by increased saturation damage. The unit cell expansion observed in the nanocrystalline sample (Figure 30) of $0.903 \pm 0.002\%$ was more than an order of magnitude greater than that observed in microcrystalline CeO_2. Furthermore, the XRD results for this material show attenuation of the initial, small cell parameter peaks accompanied by the growth of new, larger cell parameter peaks. This differs from the gradual peak shifts seen in

diffraction patterns of the microcrystalline material and suggests that highly-ionizing radiation induces a phase transformation-like process, rather than a gradual accumulation of damage, for these nanometric crystallites. A local transformation from CeO_2 to CeO_{2-x} is consistent with the aforementioned STEM results of Takaki *et al*. [178], as they directly observed the expulsion of oxygen from a central track region and determined an oxygen segregation distance, 17 nm, that is very close to the grain size of the nanocrystals used here. Thus, oxygen expelled from the track core region should reach crystallite surfaces, where it can be efficiently released, facilitating the production of a highly-modified hypostoichiometric phase. Interestingly, this result contrasts with the increased radiation tolerance observed in many nanocrystalline materials due to enhanced defect annihilation at grain boundaries [210]. This provides further evidence that the redox mechanism of radiation damage accumulation, rather than simple point defect production, is the dominant source of radiation damage in CeO_2.

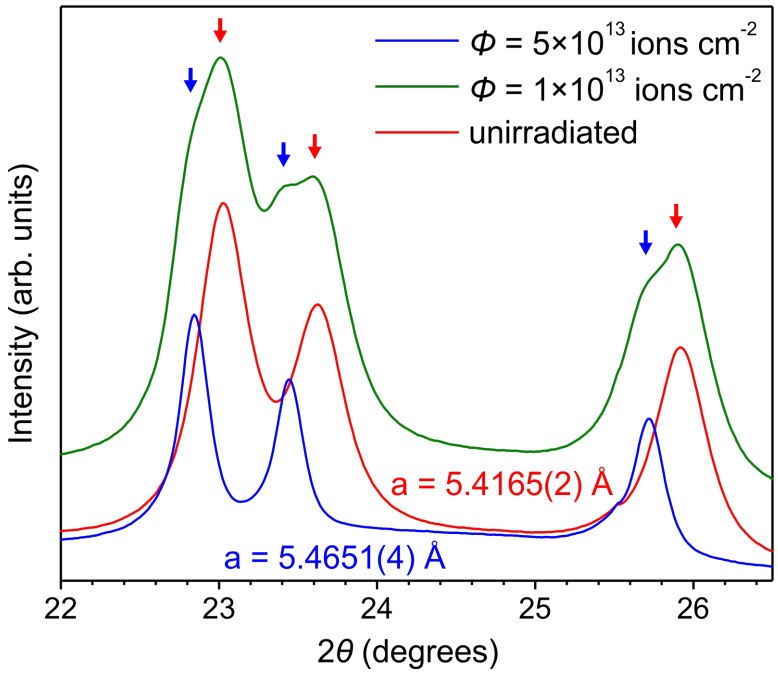

Figure 30: XRD patterns of nanocrystalline CeO_2 as a function of ion fluence. With increasing fluence, the initial fluorite-structure peaks decrease in intensity, while new fluorite-structure peaks at lower 2θ values appear and increase in intensity. At the highest fluence achieved,

5×10^{13} cm^{-2}, the initial peaks are no longer observed, indicating a complete transformation to the new fluorite material with a 0.903 ± 0.002% larger unit cell parameter. Minimal 2θ shifts of the diffraction maxima corresponding to each phase are observed as a function of fluence, such that the pattern at intermediate fluences is a superposition of the low- and high-fluence patterns.

A deleterious effect of nanocrystallinity on high energy, heavy ion radiation tolerance has previously been observed in a small number of oxides. Merkle [211] proposed the spatial confinement of energy deposited by this radiation as the cause of its destruction of very small crystallites, an effect modelled by Berthelot *et al*. [212] using a two-temperature thermal spike model. However, experimental results suggest that the influence of grain size on radiation tolerance in the electronic stopping regime cannot be explained solely by this effect. For example, Hémon *et al*. [213] showed that microcrystalline powders of Y_2O_3 are more susceptible to high energy, heavy ion radiation damage than bulk single crystals of the same material. Thermal confinement should have no effect for such a material, as the grain size is several orders of magnitude larger than the ion-solid interaction volume cross section, suggesting that this behavior is instead related to the presence of interfaces, as is consistent with the enhanced reduction of nanocrystalline CeO_2. Similarly, Moll *et al*. [214] have attributed the differing responses of microcrystalline and single crystal fluorite ZrO_2 to radiation in this regime to the loss of defects, such as interstitial anions, at grain boundaries.

4.2.4 Phase transformations in hexavalent uranium compounds

In contrast to CeO_2, in which one electron can be localized on the cerium 4*f* shell during reduction, hexavalent uranium compounds can be further reduced from U^{6+} to U^{4+}, making possible dramatic structural effects of radiation-induced redox processes. Powders of γ-phase UO_3 and a mixture of 88% α-uranyl hydroxide, 12% metaschoepite, simulating the complex phase assemblages common to nuclear fuel/water interactions, were irradiated with both 167 MeV Xe and 950 MeV Au ions (Figure 31). The structures off both materials are based on edge-

and corner-sharing uranyl coordination complexes, in which relatively short U-O axial bonds accompany longer U-O or U-OH equatorial bonds, yielding bipyramidal polyhedra. Because the stability of these structures is dependent on this coordination, which is unique to hexavalent uranium compounds [215], changes to this cation's oxidation state should show strong coupling with structural modifications.

When compared to published spectra of UO_2 [216] and UO_3 [217], the XAS spectra shown in Figure 31c,d confirm that reduction of uranium to the tetravalent oxidation state occurs for both ions used based on the shift in the U L_{III}-edge to lower photon energies, broadening of the main edge, and the disappearance of the shoulder at approximately 17.19 keV. This post-edge feature is characteristic of axial oxygen atoms present in the uranyl groups of the pre-irradiated materials [216]. The hexavalent uranium oxide structures are not stable without uranyl groups and, as shown in Figure 31a,b, this instability results in a phase transformation, as illustrated in Figure 32. With increasing ion fluence, the diffraction maxima corresponding to the hexavalent uranium compounds decrease in intensity, accompanied by the growth of new peaks corresponding to fluorite-structured UO_{2+x}. This transformation constitutes a much more extensive structural modification than the volume expansion and microstrain observed in CeO_2, indicating that the larger potential for reduction of hexavalent uranium, as compared with tetravalent cerium, results in greatly reduced radiation tolerance. Similar transformations of U^{6+} hydrolysis compounds to UO_2 have been observed in materials irradiated with electron beams [218,219], confirming that this transformation is driven by ionization.

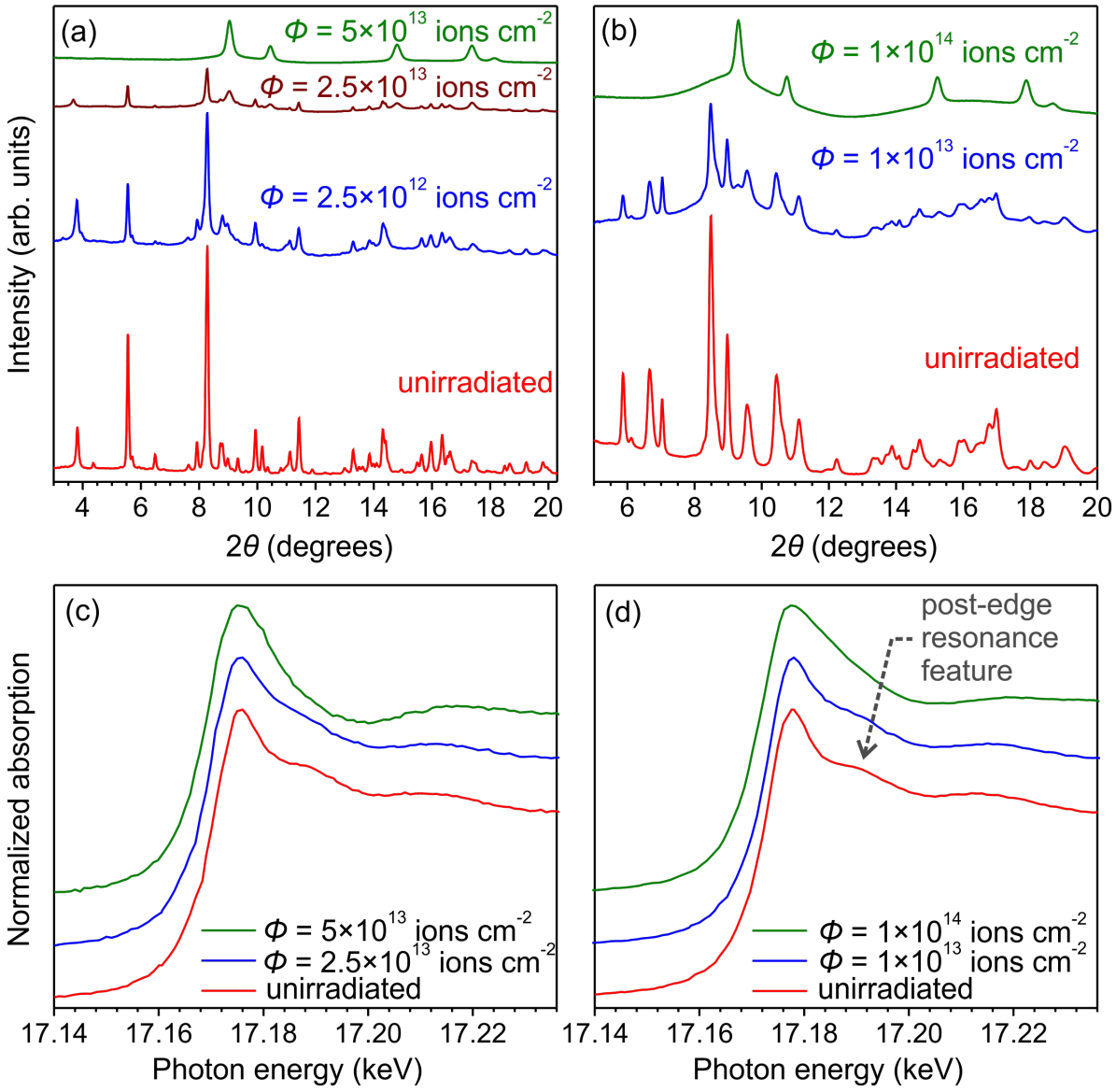

Figure 31: Evidence of structural (XRD) and chemical (XAS) modification of UO_3 and its hydration products by irradiation with swift heavy ions. (a) Representative XRD patterns of the hydration product as a function of 950 MeV Au ion fluence. (b) Representative XRD patterns of UO_3 as a function of 167 MeV Xe ion fluence. With increasing fluence, the diffraction maxima corresponding to the structures of the hexavalent uranium compounds decrease in intensity, while peaks corresponding to a UO_2-type fluorite structure increase in intensity. (c,d) XAS spectra of the uranium L_{III}-edge for both materials as a function of ion fluence. As irradiation progresses, the spectra transform from one corresponding to hexavalent uranium to one corresponding to tetravalent uranium, as indicated by, for example, loss of the post-edge resonance feature characteristic of the hexavalent state.

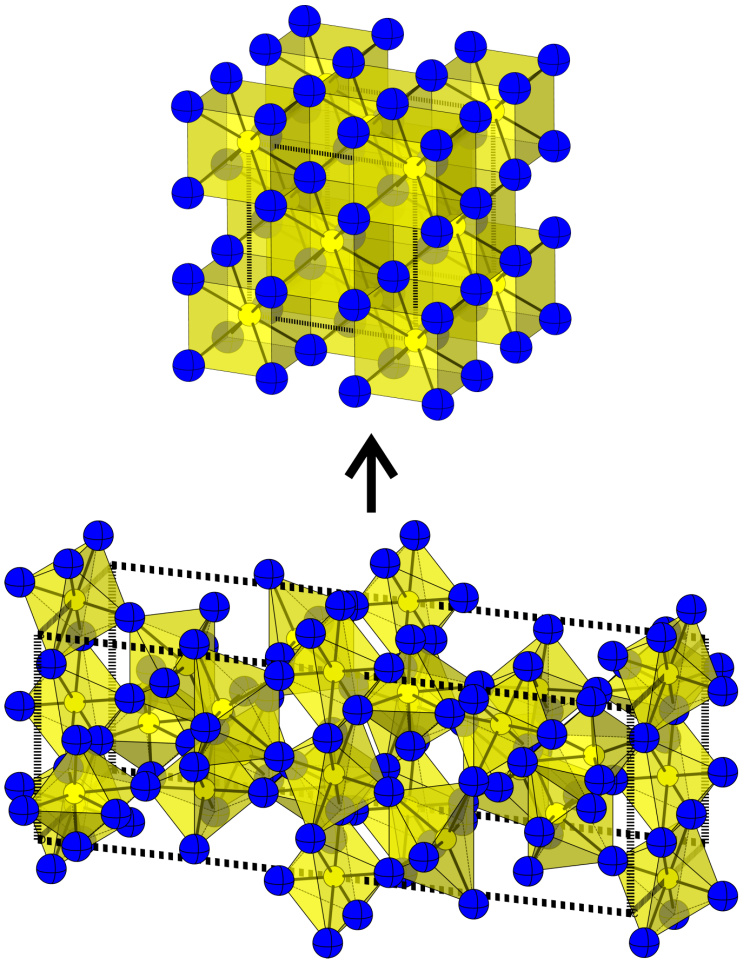

Figure 32: The unit cells of the α-UO_3 (bottom) and fluorite UO_2 structures. The trioxide has a structure based on former-sharing of uranyl bipyramidal coordination complexes, as is typical of hexavalent uranium compounds. Irradiation of α-UO_3 with swift heavy ions induced a transformation to a fluorite-like structure, characteristic of UO_{2+x}, as demonstrated by the XRD results reported here. This involves the loss of the uranyl coordination, consistent with the XAS results.

4.3 Discussion

These results demonstrate a significant influence of cation valence behavior on the ability of oxides to resist damage caused by highly-ionizing radiation. While radiation-induced redox effects have been observed in previous studies [11,175,183,184,206], this comparative investigation of both valence state changes and structural damage caused by irradiation, in a range of materials, represents the first demonstration of systematic coupling between the two modifications. Reducible materials, with multivalent cations, show structural radiation responses

that are fundamentally different from that of non-redox active ThO_2. As the efficiency of cation valence changes or the extent to which they can occur is increased, radiation tolerance decreases. For example, reduction of the grain size of CeO_2 enhances the radiation-induced redox behavior, resulting in significantly increased unit cell expansion. Irradiation of UO_3, containing hexavalent uranium with multiple accessible lower oxidation states, results in phase modification much more extensive than that caused by irradiation of CeO_2, for which cerium only has one oxidation state lower that its initial tetravalent state, and ThO_2, in which cations cannot be reduced in valence. In this way, radiation damage production at the atomic scale is closely linked to modification of materials at the electron scale, in the case of highly ionizing radiation. This indicates that, for some materials, radiation tolerance can be tailored by the control of redox behavior, through either doping with cations of different electronic configurations or grain size coarsening. Evidence of the former effect has been shown by Tahara *et al*. [176], who measured disorder in the Ce-O coordination of CeO_2 irradiated with 200 MeV Xe ions and found that doping of the material with non-multivalent Gd^{3+} reduced the extent to which this disorder was induced, thereby preserving local stoichiometry. The influence of microstructure on redox-induced damage was demonstrated in the present work, with nanocrystalline CeO_2 showing enhancement of both chemical and structural modifications, compared to its microcrystalline counterpart.

The highly heterogeneous anion distributions produced by ionizing radiation lead to structural changes that are distinct from those produced by homogeneous reduction mechanisms, such as thermal decomposition. Reduction of CeO_2 generally proceeds via a reaction involving an oxygen and two cerium atoms, wherein the anion's ionic bonds are broken when two of its electrons are localized on the cations, producing an oxygen vacancy, two trivalent cerium

cations, and half of a neutral O_2 molecule [220]. Displacement of this oxygen from its ideal site is limited in the case of irradiation by the short timescales over which it possesses the energy necessary for mobility, leading to the heterogeneous core-shell tracks discussed previously. In contrast, during thermally-induced reduction, oxygen can easily escape from the crystallites to form a homogeneous CeO_{2-x} phase. The heterogeneity of the material produced by irradiation might be expected to result in decreased expansion compared to a homogeneous case, as the hypostoichiometric track shells within which the valence of cerium is reduced is contained within a hyperstoichiometric matrix, constraining its expansion. Consistent with this interpretation, the 0.06% expansion observed for irradiated CeO_2 is much lower than the 1.1% expansion measured for the same material reduced by thermal treatment to the same trivalent cerium fraction [197], assuming that this fraction is linearly proportional to the Ce K-edge position. The influence of stoichiometric heterogeneity on unit cell expansion should be lessened in the case of irradiated nanocrystals, for which displaced oxygen can more easily escape the crystallites, as occurs in reduction through thermal processes. The results presented here agree, as the irradiated CeO_2 nanospheres exhibit a 0.9% reduction that is much closer to the 2.5% observed for thermal reduction to the same trivalent cerium fraction [197], again assuming linear proportionality between this fraction and the Ce K-edge position.

In this study, materials in which the *f*-block cations exhibited their highest stable oxidation state were used in order to isolate the influence of valence reduction on radiation damage accumulation. However, the actinide elements present in the common nuclear fuel components UO_2 and PuO_2 possess higher oxidations states, allowing for the formation of stable, hyperstoichiometric oxides with the fluorite structure. This might be expected to result in enhanced tolerance for highly-ionizing radiation, as these materials can easily incorporate

adventitious oxygen, as found in CeO_2 ion track shells, with minimal structural modification [221]. Experimental work has demonstrated, for low fluences, exceptional tolerance of UO_2 to fission fragment radiation [222,223]. However, at fluences on the order of 1×10^{14} cm^{-2}, damage to the atomic structure begins to rapidly accumulate in the form of unit cell expansion [33]. At such high fluences, both CeO_2 [224,225] and UO_2 [222,226] are known to undergo extensive microstructural modification under fission fragment irradiation, developing nanocrystalline subgrains and porosity. Termed the "rim effect," this process is commonly encountered in the relatively cool outer region of fuel pellets where fission rates are highest, and has been attributed to the formation of a dislocation loop network [222,224–226]. The precipitation of anion interstitial defects into these dislocation loops has been observed in CeO_2 [227] and UO_2 [223,228] irradiated with ionizing radiation. Density functional theory calculations [229] have shown that these interstitial oxygen defects are stable in neutral charge states, which would allow for charge neutrality following the transfer of electrons to cations. This behavior is consistent with the redox-induced charge redistribution process observed in the current work. At low fluences, UO_2 is able to easily incorporate the local stoichiometry variation produced by radiation-induced valence changes. However, once the interstitial oxygen expelled from ion track cores begins to form neutral defect clusters and, at high fluences, a dislocation network, it can contribute to fuel degradation in the form of "rim effect" microstructural damage. Because it has been shown that the production of these anion defects is coupled to valence state changes in the cations, control of a material's redox behavior presents a possible strategy for the mitigation of this radiation-induced fuel degradation process.

4.4 Conclusions

f-block oxides that incorporate cations which are not in their lowest stable oxidation state exhibit swift heavy ion irradiation-induced cation valence reduction. This modification of the electronic configuration of *f*-block cations leads to coupled modifications to the atomic structures of these materials, as valence reduction results in changes to the ionic radius and bonding of the cations. Because the oxidation states accessible to *f*-block elements are not fully uniform, particularly in the light actinides due to their relatively itinerant *f*-orbitals, this irradiation-induced valence reduction mechanism yields related compositional variation in the structural response of these oxides to swift heavy ion irradiation. ThO_2, a fluorite-structured dioxide with a cation that does not possess a trivalent state in oxide compounds, exhibited irradiation-induced unit cell expansion and microstrain accumulation that was attributable to defect formation. In contrast, CeO_2 exhibited a reduction of Ce^{4+} to the trivalent state under identical irradiation conditions, which is the primary source of unit cell expansion and microstrain accumulation in this material. Nanocrystallinity was shown to enhance both the valence reduction of cations in CeO_2 and the material's associated structural modifications. Finally, irradiation-induced reduction of U^{6+} to U^{4+} caused a phase transformation of UO_3 to a fluorite-like structure, characteristic of UO_{2+x} phases. Generally, oxides containing multivalent *f*-block elements with stable lower oxidation states exhibit responses to swift heavy ion irradiation that are controlled by their irradiation-induced redox behavior, in contrast to the behavior of oxides of non-multivalent elements, the responses of which tend to be governed by the effects of defect accumulation and the phase systematics of these compounds.

Chapter 5

Swift heavy ion irradiation of $Ln_2Sn_2O_7$ and related materials: irradiation-induced disordering and amorphization

The *f*-block elements can be incorporated with many transition metals and main group metals in a variety of complex ternary oxides. Prior study of the response of complex oxides to radiation damage has been largely motivated by their proposed use as host materials for the immobilization of nuclear wastes and as inert matrix nuclear fuels for the transmutation of plutonium and the "minor" actinides (Np, Am, and Cm) in advanced nuclear fuel cycles [92,230–232]. One of the most commonly studied materials systems for these applications is the class of $Ln_2B_2O_7$ compounds (where B is a transition or main group metal) exhibiting the pyrochlore structure (see Figure 8) [92]. Many ternary oxides of the general formula $A_2B_2O_7$ exhibit this phase, isostructural with the mineral pyrochlore, $(Na,Ca)_2Nb_2O_6(OH,F)$ [233]. These compounds are crystallographically related to the fluorite structure, but are distinguished by their inclusion of both a tetravalent B-site metal cation and a trivalent A-site cation. Ordering of these two species on the cation sublattice and the presence of ordered oxygen vacancies on the anion sublattice result in a 2×2×2 superstructure of the fluorite unit cell, where the pyrochlore cell (*Fd3m*) can be considered to consist of eight fluorite cells (*Fm3m*) (see Figure 8). The fluorite structure's single 4*a* cation site is replaced by 16*c* and 16*d* sites, on which the A- and B-site cations are ordered in rows alternating in [110] and [-110], on sequential (002) planes. Three pyrochlore anion sites replace the fluorite 8*c* oxygen site: the 8*b* site is coordinated tetrahedrally with four B-site cations, the 8*a* site is vacant to maintain charge balance, and the 48*f* site is

displaced towards this anion vacancy, leading to coordination with two A- and two B-site cations in distorted tetrahedral configuration. The magnitude of this displacement, represented by the difference of the 48*f* site *x*-coordinate from the ideal fluorite-type value of 0.375, fully describes the structure of any pyrochlore-type compound and varies with composition [234]. It leads to distortion of the otherwise octahedral and cubic anion coordination of the A- and B-site cations respectively. Because the distortion of pyrochlores from the ideal fluorite structure is caused by the incorporation of two cations of different ionic radii and oxidation state, those compounds with similarly-sized cations exhibit less distortion, and hence 48*f* site *x*-coordinates closer to 0.375. Pyrochlores typically undergo a high temperature order-disorder phase transformation to an oxygen deficient fluorite structure, with random arrangements of the two cations and constitutional oxygen vacancies on the cation and anion sublattices, respectively [235]. The critical temperature for this transformation, $T_{O\text{-}D}$, is generally inversely proportional to the cation ionic radius ratio, r_A/r_B.

While swift heavy ion irradiation tolerance trends in ternary lanthanide oxides with the pyrochlore structure have been extensively studied, the majority of this work has focused exclusively on titanate and zirconate compounds (B = Ti or Zr). Under ion irradiation, many of these compounds amorphize [236]. In an extension of previous work on the radiation tolerance of complex oxides due to nuclear stopping of energetic ions [237], Lang *et al.* [114,238] and Sattonnay *et al.* [239,240] have shown that the resistance of materials with the pyrochlore structure to swift heavy ion irradiation-induced amorphization varies with their composition. In particular, for pyrochlore materials of the general formula $A_2B_2O_7$, amorphization proceeds most rapidly, as a function of ion fluence, when the ratio of the A- and B-site cation ionic radii, r_A/r_B, is large. As this ratio decreases, the stability of a defect fluorite high temperature polymorph,

which represents a disordered state in which the pyrochlore superstructure is lost, increases. Thus, pyrochlores that are resistant to amorphization instead show an ion irradiation-induced disordering phase transformation, yielding a defect fluorite material. This relationship between composition and the thermodynamic stability of the disordered defect fluorite phase can also be considered in terms of the critical temperature for thermal disordering of a pyrochlore, $T_{O\text{-}D}$ [237], which represents the relative stability of this phase, or the formation energy of a cation antisite defect, which drives the order-disorder transformation because the pyrochlore superstructure is based on an ordered arrangement of A- and B-site elements on the cation sublattice [241].

The stannate pryochlores, in which the B-site cation is tin, are of particular interest for such investigations. The ionic radius of Sn^{4+} is intermediate to those of Ti^{4+} and Zr^{4+} (the pyrochlore B-site element is generally tetravalent). Based on the aforementioned ionic radius ratio radiation tolerance criterion [237], this would be expected to yield intermediate radiation tolerance for stannate pyrochlores, with susceptibilities to amorphization between those of comparable titanates, which are easily amorphized, and the highly tolerant zirconates, which generally show disordering with little or no amorphization. However, the Sn-O bond is known to be highly covalent, much more so than both the Ti-O and Zr-O bonds [242,243]. Naguib and Kelly [244] have proposed a bond covalency criterion for radiation tolerance, which was later supported by experiments and analysis by Eby *et al.* [245] and Trachenko *et al.* [246,247]. This assessment is based on the influence of bonding on the recrystallization of a highly-damaged ion track region and the energy landscape encountered by the constituent atoms in a relaxing thermal spike. According to this analysis, covalently-bonded materials exhibit short-range interatomic forces that encourage the formation of covalent networks with only short-range ordering, as seen

in amorphous silicon, where corner-sharing SiO_4 tetrahedra can organize in an amorphous local-minima of the material's structural energy landscape, for which long-range ordering is absent. Conversely, materials with strong ionic character in their bonding exhibit longer-range electrostatic forces that prevent the atoms from relaxing to an amorphous local energy minima, instead promoting recrystallization of a melted thermal spike region. Experimental data from a large number of insulating and semiconducting materials follow this general trend in radiation tolerance, exhibiting greater resistance to radiation damage with decreasing bond covalency [246]. This bond covalency criterion for radiation tolerance [246] would predict greater susceptibility to swift heavy ion irradiation-induced amorphization for the stannate pyrochlores than both the zirconate and titanate pyrochlores. Here, a systematic study of the radiation response of stannate titanates with A-site cations spanning the lanthanide series is presented, with the intent of comparing the applicability of these two radiation tolerance criteria to the pyrochlore system. It is shown that the covalency of the Sn-O bond does not give rise to significant deviation of the behavior of the stannate pyrochlore under swift heavy ion irradiation from that predicted based on ionic radius considerations.

5.1 Experimental methods

Materials in the system $Ln_2Sn_2O_7$ with A-site cations spanning the lanthanide series (Nd, Sm, Gd, Er, and Yb) as well as the rare earth cation Y, were synthesized via solid state methods. By investigating compounds with multiple lanthanide cations, which decrease in ionic radius across the lanthanide series, the effects of cation size were isolated, as the lanthanide elements are all chemically similar due to their strongly localized, non-bonding *f*-orbitals. Stoichiometric ratios of the binary compounds Ln_2O_3 and SnO_2 were mixed, milled, and calcined to form well-ordered pyrochlore materials. This powder was then pressed into small pellets of 50 μm

thickness and ~60% theoretical density. These samples were irradiated at beamline M2 of the UNILAC linear accelerator at the GSI Helmholtz Centre for Heavy Ion Research in Darmstadt, Germany, with 2246 MeV Au ions. Samples were irradiated to fluences of up to 3×10^{13} cm^{-2}, with the ion flux limited to less than 10^{9} $cm^{-2}s^{-1}$ to avoid bulk heating of the samples. The projected ranges of the ions in a fully dense sample were greater than 50 μm for all materials tested, indicating that all ions passed completely through the low density compacts. The calculated nuclear energy loss was, for the entire ion path, at least two orders of magnitude less than the electronic energy loss and was assumed to be negligible.

Characterization of the initial and irradiated samples was performed using transmission electron microscopy, x-ray diffraction, and Raman spectroscopy. Samples irradiated to a fluence of 5×10^{10} cm^{-2}, at which individual ion tracks are well-separated and easily resolved, were crushed into a fine powder that was then deposited on a holey carbon grid. TEM imaging of ion tracks in various orientations with respect to the electron beam was carried out on a JEOL 3011 microscope. Angle-dispersive synchrotron XRD was performed at the B2 beamline of the Cornell High Energy Synchrotron Source (CHESS). A monoenergetic beam (λ = 0.496) was operated in transmission mode with a spot size of 300 μm and the resulting diffraction rings were recorded with a charge coupled device (CCD) detector. Integration of the CCD images was performed using Fit2D software [110] and the resulting diffraction patterns were refined with Fullprof software [142]. The degree of irradiation-induced amorphization was quantitatively analyzed by deconvoluting these diffraction profiles in order to isolate diffraction intensity contributions from the crystalline and amorphous fractions, a process similar to that used in previous studies of irradiated pyrochlores [114]. Pseudo-Voigt functions were used in the peak fitting procedure. Semi-quantitative values of the total amorphous fraction were then obtained by

taking the ratio of the integrated intensity of the broad amorphous peaks to that of the sharp crystalline peaks over the entire 2θ range measured. Raman spectra were collected using a Renishaw inVia Raman Microscope with a 785 nm laser operating in backscattering geometry. A measuring time of 25 s was used for all samples and spectra were collected over a range of 100-1000 cm^{-1}. Multiple measurements were taken at different positions for each sample to test for orientation effects, which were not observed.

5.2 Results

In all materials tested, irradiation with swift heavy ions induced phase modification within ion tracks of roughly ten nanometers in diameter. Low-magnification HRTEM micrographs of all materials tested exhibited contrast between the ion tracks and the surrounding, unmodified material matrix. A representative micrograph is shown in Figure 33. The tracks are highly linear and, in all crystallites observed, extend from one surface to another, confirming that the accelerated ions passed completely through these samples. This contrast suggests a modification of the material's structure in the interior of the ion tracks. Such a modification could indicate either a crystalline-to-crystalline phase transformation, such as the order-disorder fluorite transformation common to zirconate pyrochlores, or amorphization, as has been shown to occur in titanate pyrochlores [238].

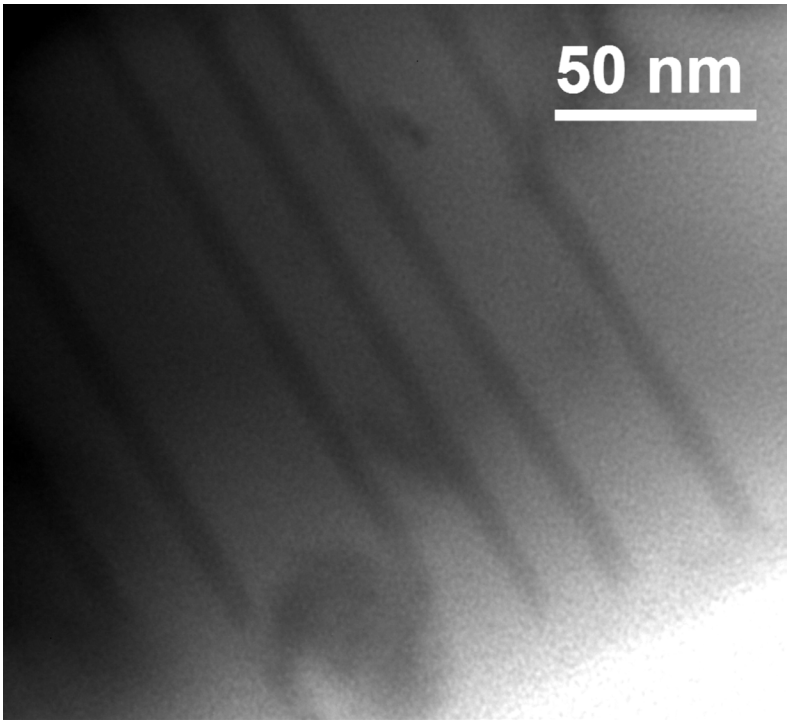

Figure 33: A TEM micrograph of ion tracks in $Nd_2Sn_2O_7$. Strong contrast is observed between the track interiors and the surrounding, unmodified matrix. This indicates a structural modification that affects the diffraction of the electron beam from these ion track regions.

To obtain quantitative information regarding the structural transformations induced by high energy ion irradiation, XRD was used. As shown by Figure 34, the collected diffraction patterns exhibit a large variation in radiation response with composition. A general trend of decreasing amorphization and increasing fluorite formation as large, light lanthanide cations are substituted with smaller, heavier lanthanides is evident. In $Nd_2Sn_2O_7$, the least radiation tolerant material tested, the pyrochlore diffraction maxima are significantly attenuated as the ion fluence increases. Simultaneously, there appear four broad peaks, indicative of the formation of amorphous material [113], in the approximate ranges 2θ = 7-11°, 13-17°, 17-20°, and 22-26°. In contrast, $Yb_2Sn_2O_7$ shows very little evidence of amorphization. Instead, a phase transformation to the defect fluorite structure is indicated by the attenuation of only the diffraction maxima corresponding to the pyrochlore superstructure ordering, with no change in those common to

both the pyrochlore and fluorite lattices. By a fluence of 1.5×10^{13} cm^{-2}, the (111), (133), and (155) pyrochlore superstructure peaks are absent, while the pyrochlore (222), (004), (044), and other peaks are maintained. These latter peaks correspond to the (111), (002), and (022) fluorite reflections in the modified phase. This loss of superstructure ordering corresponds to the mixing of A- and B-site cations on a single sublattice (the formation of cation antisite defects) and the mixing of anion 8*b* vacancies with occupied anion sublattice sites. For compositions with lanthanide cations between neodymium and ytterbium, intermediate behavior was observed, with both amorphization and disordering occurring. The ratio of the extent to the two transformations is dependent on the cation ionic radius ratio.

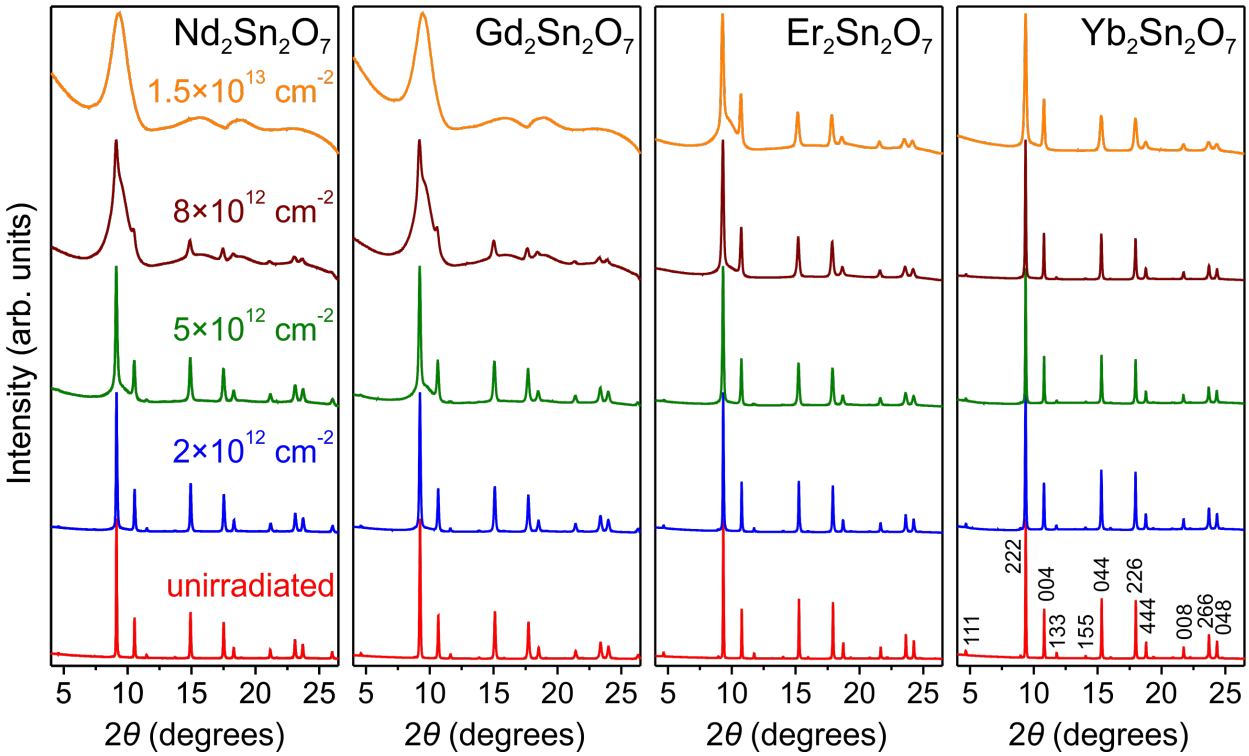

Figure 34: Representative XRD patterns of stannate pyrochlores irradiated to a range of ion fluences. Amorphization in those compounds containing lanthanides of low atomic number is indicated by the growth of broad scattering bands, while a transformation to the fluorite structure in those containing heavier lanthanides is indicated by the attenuation of the pyrochlore superstructure peaks (e.g. (111), (133), (155), etc.)

Raman spectroscopy is highly sensitive to short-range ordering, making it a useful tool for the analysis of defect-rich materials such as these. In pyrochlores, both amorphization and disordering to the defect fluorite structure involve the loss of order, since the crystalline defect fluorite phase must accommodate random arrangements of aliovalent cations and oxygen vacancies. The spectroscopy results show similar spectrum evolution with fluence regardless of the modification induced by swift heavy ion irradiation. Representative spectra are shown in Figure 35 for $Nd_2Sn_2O_7$, which amorphizes, and $Yb_2Sn_2O_7$, which disorders. Attenuation of the initial peaks, which match well to those previously reported for stannate pyrochlores [248], occurred in both materials at a similar rate, as a function of ion fluence, as does the growth of a broad band centered at approximately 650 cm^{-1}. Similar broad features in disordered titanate pyochlores have been attributed to TiO_x polyhedra with low oxygen coordination (five- or six-fold) due to disorder on the anion sublattice [249]. The fact that this band is observed at the highest ion fluence achieved in all compositions tested (Figure 36) suggests that the local environment of oxygen-coordinated titanium following irradiation is similar in both the fluorite and amorphous phases. At the highest fluence achieved, the only feature distinguishing the disordered materials from those that have become amorphous is a peak at approximately 450 cm^{-1}. This corresponds to a T_{2g} mode common to well-crystallized, non-defective fluorite materials [191] and its increase with the substitution of lanthanides cations of higher atomic number, shown in Figure 36, is further evidence of a trend towards disordering, rather than amorphization. This peak is present, although of low intensity, even in compositions which, at the highest ion fluences achieved, are completely amorphous based on the XRD data (Figure 34). This suggests that, despite the loss of long-range order in these materials, domains of local fluorite-like structure are retained.

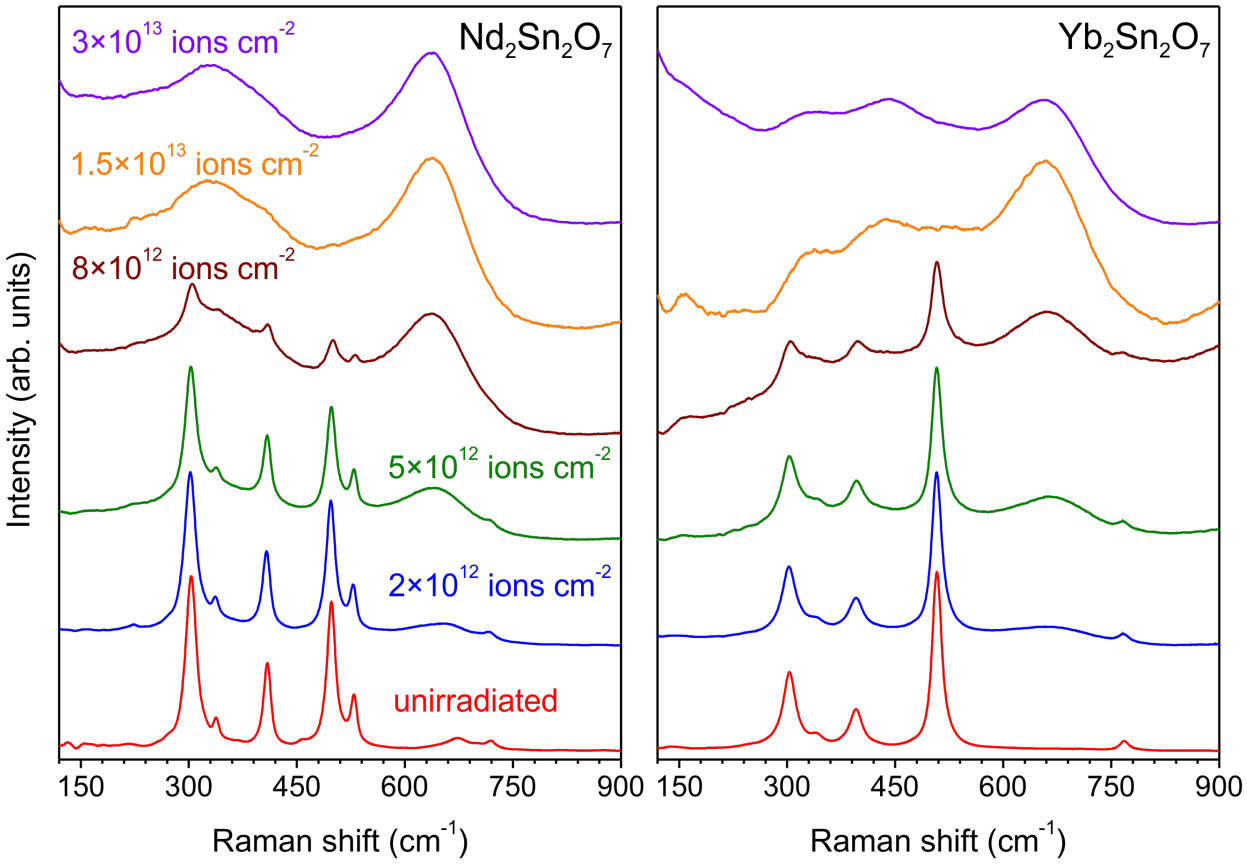

Figure 35: Raman spectra of the stannate pyrochlore compounds featuring the highest and lowest cation ionic radius ratio values of those compositions tested, $Nd_2Sn_2O_7$ and $Yb_2Sn_2O_7$, at various ion fluences. Similar spectrum evolution is seen for both compounds, despite their distinct ion track morphologies.

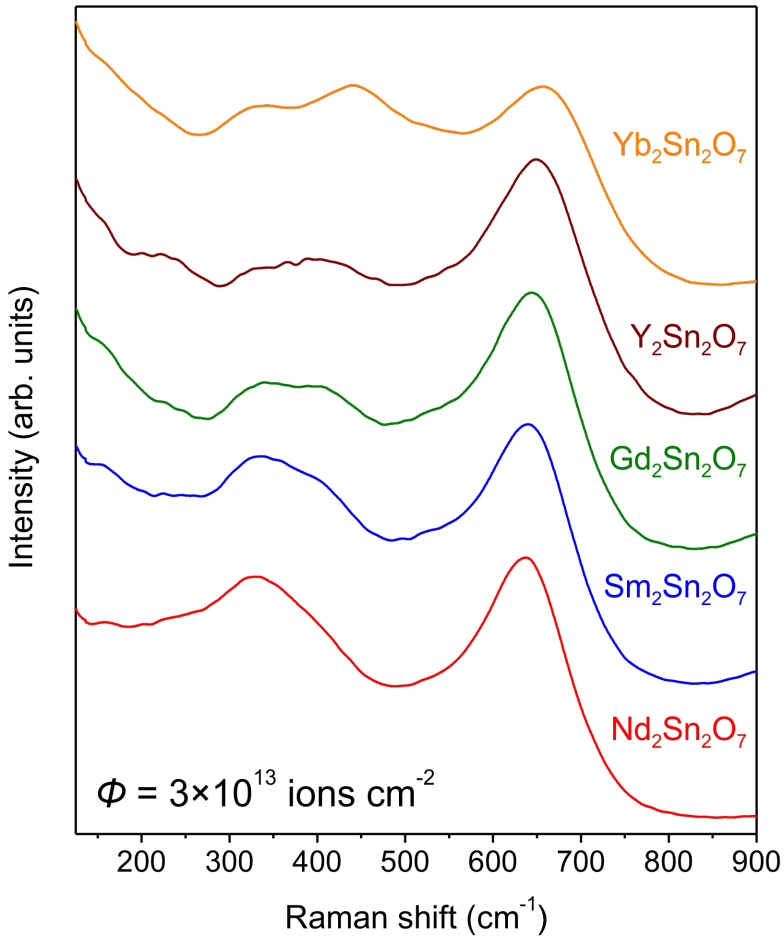

Figure 36: Raman spectra obtained from all compositions tested, irradiated to a high ion fluence of 3×10^{13} cm^{-2}. At this fluence all samples exhibit fully-modified defect fluorite or amorphous structures. Despite the different modifications induced, with $Nd_2Sn_2O_7$ showing complete amorphization and $Yb_2Sn_2O_7$ instead showing complete disordering to a defect fluorite phase, the Raman spectra are similar, with the exception of that corresponding to $Y_2Sn_2O_7$, which does not contain a lanthanide cation. With this exception, the only compositional variations in the spectra are minor changes in peak positions and intensities, along with the growth of a peak at around 450 cm^{-1} with increasing atomic number of the lanthanide cation. The growth of this peak, which is attributed to a fluorite structure T_{2g} mode, is accompanied by decreasing susceptibility of a material to amorphization and increasing susceptibility to disordering.

5. 3 Discussion

Data detailing the extent of a phase transformation as a function of ion fluence can be used to determine the volume of material in which a given transformation is induced, per incident ion. Because ion tracks in these compounds are continuous cylinders of relatively uniform diameter along the majority of the ion path, as verified by TEM results (Figure 33),

these values are typically reported as cross sectional areas or track diameters [159,238,250]. In materials for which a single phase transformation is observed, such as the easily amorphized, disordering-resistant titanate pyrochlores [114], and for which the volume within a particular ion track is completely modified after it is traversed by a single impinging ion, a single-impact damage accumulation model [146] is used (Eq. 1). However, in many of the stannate pyrochlores, two irradiation-induced phase modifications occur simultaneously: amorphization and disordering to a defect fluorite structure. Swift heavy ion damage in these materials is generated through atomic displacements and is mitigated via defect recovery and recrystallization at the interface between the high-energy, defect-rich volume in the interior of ion tracks and the surrounding crystalline material. Thus, the formation of the disordered defect fluorite phase in pyrochlores can be attributed to either direct production of this phase through the formation of cation antisite defects and anti-Frenkel pairs, without concurrent loss of fluorite-like ordering, or to post-amorphization recrystallization into defect fluorite phase, with favorable amorphous-to-defect fluorite transformation kinetics allowing for this transformation to occur prior to quenching of the excited ion track interior. In the former case, complete amorphization would be expected at high fluences, as eventually track overlap would lead to exposure of the entire volume of a sample to the high-damage track core region in which amorphization is induced. In contrast, a melting/recrystallization process would produce a steady state at high fluences in which amorphous and disordered crystalline volume fractions coexist. The XRD data collected here are consistent with this mechanism of damage accumulation as, with the exception of $Nd_2Sn_2O_7$ and $Sm_2Sn_2O_7$, the stannate pryochlores show both amorphous and defect fluorite domains at high fluences.

In the proposed damage accumulation mechanism, each impinging ion produces dense atomic displacement, destroying the initial structure of material inside an ion track. This produces a defect-rich, liquid-like state within the ion track over short timescales. As the associated energy diffuses into the surrounding matrix, recrystallization takes place, starting at the crystalline/liquid interface and proceeding towards the track centerline. Because such a transformation is most efficient at elevated temperature, rapid quenching of the ion track region will result in incomplete recrystallization. In the case of some pyrochlores, the disordered defect fluorite structure, the formation of which is kinetically favorable relative to formation of the highly ordered pyrochlore phase, is quenched to ambient conditions, under which it is metastable. This description of the transformation process is consistent with previous TEM observations of pyrochlore ion tracks in which amorphous track cores were found to be surrounded by concentric track shells of material with a defect fluorite structure [35,238].

Because the defect fluorite phase forms directly from the highly-damaged track interior, the initial structure within the ion track does not affect its final structure and morphology. Thus, if the outer track shell region overlaps with an initially amorphous volume, that volume will be transformed to the defect fluorite phase following quenching. In this manner, a dynamic phase fraction equilibrium is attained at high fluences, at which the volume fraction ratio of the two phases is proportional to the track cross-sectional area for a given modification (σ_a for the amorphous phase and σ_f for the fluorite phase). The single-impact model (Eq. 1) does not account for the pyrochlore-fluorite transformation and cannot model saturation of f_a at values below one. An accurate damage model for the stannate pyrochlores must incorporate the influence of disordering processes.

Modelling of such a process requires the use of a system of differential equations corresponding to the volume fraction evolution of each phase:

$$\frac{df_a}{dt} = \sigma_a(1 - f_a)\Phi - \sigma_f f_a(1 - f_a)\Phi \tag{7}$$

$$\frac{df_f}{dt} = \sigma_f f_a(1 - f_a)\Phi + \sigma_f f_p \Phi + \sigma_a f_f \Phi \tag{8}$$

$$\frac{df_p}{dt} = 1 - \sigma_f\left(1 - f_p\right)\Phi - \sigma_a\left(1 - f_p\right)\Phi \tag{9}$$

where f_f is the fluorite phase fraction, f_p is the pyrochlore phase fraction, and Φ is the ion flux. The solutions to these equations:

$$f_a(\Phi) = \frac{1 - e^{-\sigma_a\Phi + \sigma_f\Phi}}{1 - \left(\frac{\sigma_f}{\sigma_a}\right)e^{-\sigma_a\Phi + \sigma_f\Phi}} \tag{10}$$

$$f_f(\Phi) = \frac{\left(\sigma_a - \sigma_f\right)e^{\sigma_f\Phi}}{\sigma_a e^{\sigma_a\Phi} - \sigma_f e^{f\Phi}} - e^{-\sigma_a\Phi + \sigma_f\Phi} \tag{11}$$

give the phase fractions of both ion beam modification products as a function of fluence, with the cross-sectional areas of each modification as variables. By extracting phase fraction data from the XRD results for a range of fluences, fitting of this kinetic direct impact model can be used to obtain effective cross sections and track morphology information. Application of this technique to the amorphization data collected here yielded the curves shown in Figure 37. The effective cross-sectional areas for both amorphization and disordering extracted from this fitting procedure (Figure 38) illustrate a dramatic change in track morphology as a function of the A-site cation and, therefore, of the cation ionic radius ratio. The smaller, heavier lanthanides yield low r_A/r_B values, resulting in a more stable fluorite phase and ion tracks with extensive disordering and

only minor amorphization. As the ionic radius of the A-site lanthanide cation increases, the tracks contain larger amorphization cross sections and less defect fluorite production, with $Sm_2Sn_2O_7$ and $Nd_2Sn_2O_7$ exhibiting fully amorphous ion tracks and no evidence of transformation to the fluorite phase. These results are consistent with those previously obtained on titanate and zirconate pryochlores [114,238,240].

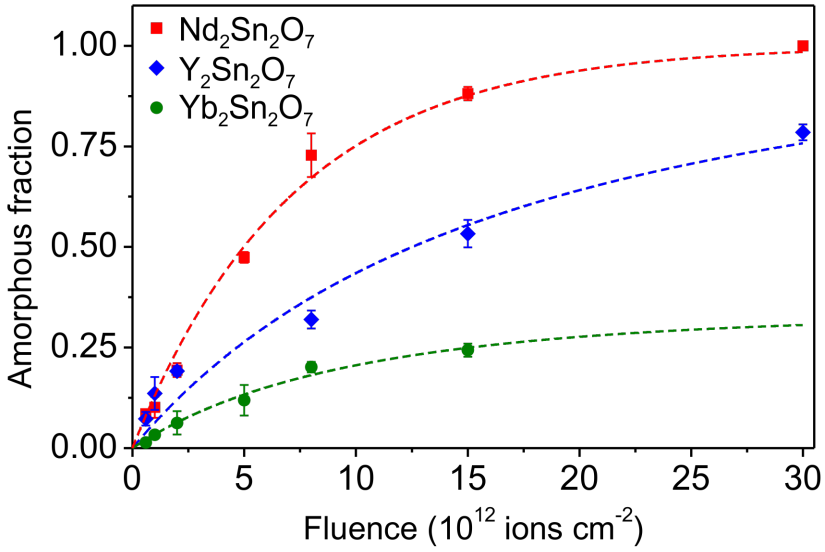

Figure 37: Evolution of the amorphous fraction in representative stannate pyrochlores as a function of ion fluence. While $Nd_2Sn_2O_7$ follows single-impact model behavior, the compounds containing smaller lanthanide cations do not fully amorphize due to the formation of disordered ion track shells.

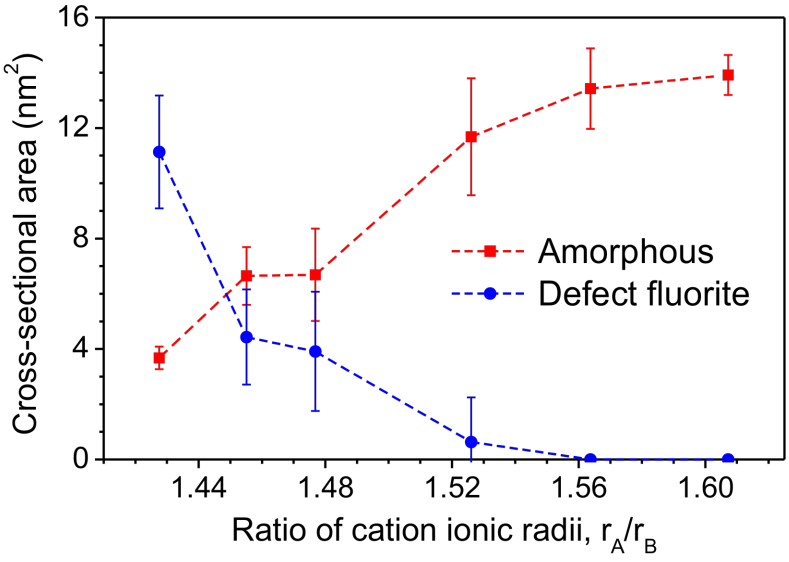

Figure 38: Ion track cross-sectional areas corresponding to the two phase modifications observed in ion irradiated stannate pyrochlores: disordering to a defect fluorite phase and amorphization. As the cation ionic radius ratio decreases with the substitution of lanthanide cations of higher atomic number, ion tracks tend to exhibit a larger fluorite fraction, with less amorphization in the track core region.

5.4 Conclusions

The responses of the stannate pyrochlores to highly-ionizing radiation confirm that cation ionic radius effects associated with phase systematics control the radiation response of materials in this system. Despite the strongly covalent character of the Sn-O bond, stannate pyrochlores with small r_A/r_B values, such as $Yb_2Sn_2O_7$, were shown to be highly resistant to irradiation-induced amorphization. Thus, the previously proposed bond covalency criterion for radiation tolerance [244–247] is not consistent with the behavior observed here, as the stability of the disordered fluorite phase, which possesses a low kinetic barrier to formation from an excited ion-solid interaction volume, counteracts the effects of the complex energy landscape associated with covalent networks. The kinetic accessibility of this disordered phase in the interior of newly-formed ion tracks leads to the remarkable resistance of some stannate pyrochlores to radiation-induced amorphization. However none of the pyrochlores investigated here retain their initial structures following ion irradiation. Ion tracks of all compositions show some degree of amorphization. As such, the radiation response of these complex oxides is governed primarily by the energetics of recrystallization and its extent. As the difference of the ionic radii of the two cations in a pyrochlore compound increases, so too does the energy of the antisite defect, which is a constitutional defect of the disordered fluorite phase. Thus, the formation enthalpy of the defect fluorite phase is proportional to this ionic radius mismatch, such that the driving force for recrystallization of a damaged region in the ion-solid interaction volume to this disordered phase is inversely proportional to r_A/r_B. The results presented here indicate that these defect fluorite

phase energetics determine the extent to which this phase is formed, in the place of an amorphous phase, under swift heavy ion irradiation. No evidence of electronic structure modification was observed, consistent with the behavior of lanthanide elements in binary oxides.

Chapter 6

Conclusions

This dissertation reports the results of investigation of swift heavy ion-induced modifications to three classes of materials: binary lanthanide sesquioxides, binary lanthanide and actinide dioxides and trioxides, and ternary lanthanide stannates. The nature of these modifications was found to depend strongly on composition within each system. As the atomic number of the lanthanide cation in Ln_2O_3 compounds increased (and its ionic radius decreased), these materials became more resistant to an irradiation-induced transformation from a C-type phase to a B-type phase. For materials that exhibited very high resistance to this transformation, an alternative transformation to an X-type phase was observed. Both this C-to-X transformation and amorphization became more prevalent, as a function of ion fluence, with decreasing ion velocity (and increasing deposited energy density in the ion-solid interaction region). This complex phase behavior under swift heavy ion irradiation showed that the radiation response of materials in this system is controlled largely by their phase systematics.

In contrast to the diversity of irradiation-induced phase transformations observed in the lanthanide sesquioxides, all lanthanide and actinide dioxides studied retained their fluorite structures during irradiation with swift heavy ions. However, most of the *f*-block elements with stable tetravalent oxides states, as are encountered in the dioxides, can also adopt stable trivalent oxidation states. Therefore, while irradiation-induced phase transformations are inaccessible to the non-polymorphic *f*-block dioxides, they can undergo irradiation-induced valence reduction. This redox effect was found to exhibit coupling with structural modifications such as unit cell

expansion and heterogeneous microstrain, which arise from changes to the ionic radii and bonding of cations concomitant with changes in their oxidation states. Because redox behavior and oxidation state stability vary among the *f*-block elements, compositional variation in the radiation response of materials in this system was observed. In materials with structures based on cation coordination complexes particular to a certain cation oxidation state, as α-phase uranium trioxide is based on corner-sharing of uranyl polyhedra, this irradiation-induced valence reduction was found to induce a simultaneous change in structure and cation valence. Due to this coupling of swift heavy ion irradiation-induced redox effects to structural modification of dioxides and trioxides, the radiation response of materials in this system is controlled largely by the valence variability of their constituent cations.

Like the behavior of the lanthanide sesquioxides, stannate pyrochlores incorporating lanthanide elements ($Ln_2Sn_2O_7$) exhibited both amorphization and polymorphic phase transformations in response to swift heavy ion irradiation. Many compositions in this system exhibited an order-disorder transformation to a defect fluorite phase. As the lanthanide cation ionic radius of these materials decreases, the stability of their disordered, high temperature defect fluorite polymorph increases. Consequently, the extent of amorphization at a specific ion fluence decreases with the substitution of smaller Ln cations into these materials, and the extent of disordering to the defect fluorite phase increases. This compositional variation in the susceptibility of these materials to swift heavy ion irradiation-induced structural modification is analogous to that observed in the lanthanide sesquioxides. Pyrochlore compounds containing actinide elements ($An_2Sn_2O_7$) were not studied in this work. However, in a previous investigation of the response of $Am_2Zr_2O_7$ and $Cf_2Zr_2O_7$ to irradiation with alpha particles, Sykora *et al.* [251] identified changes to the oxidation states of these actinide elements during

irradiation as an important factor in observed transformations from the initial pyrochlore phase to a defect fluorite phase. This suggests that the irradiation-induced redox effects that were found to play a major role in the radiation response of many actinide oxides also contribute to behavior of actinide pyrochlores that is distinct from that of the lanthanide pyrochlore compounds.

These results yield an improved understanding of the systematics of the *f*-block oxide radiation response. The effects of energy deposited to the electronic subsystems of these materials on their atomic subsystems are mediated by the energetics of valence changes and defect formation. In materials with constituent elements lacking valence variability, the energetics of defect formation and associated phase transformations govern their structural response to swift heavy ion irradiation. This results in the ionic radius dependence of the phase transformations induced in lanthanide-bearing sesquioxides and pyrochlores as, per Pauling's first rule [165], the cation ionic radius determines the stability of the cation coordination characteristic of a specific phase. Because the Ln_2O_3 C-to-B transformation and the $Ln_2Sn_2O_7$ pyrochlore-to-defect fluorite transformations involve changes in cation coordination from 6-fold to 7-fold and from 8-fold to 7-fold, respectively, the radiation responses of these materials show strong r_{Ln} dependence. Thus, compositional trends in the radiation responses of materials containing trivalent *f*-block cation can typically be predicted by consideration of the influence of the ionic radius of this cation on the polymorphism of the material. In contrast, irradiation-induced phase transformations are largely precluded in non-polymorphic materials, such as the *f*-block dioxides. Instead, many of these materials have accessible oxidation states below the tetravalent state, allowing them to undergo modification of the electron distribution as additional electrons localize on cations during relaxation of the electron-hole plasma. This results in modified bonding, such that the susceptibility of a material to these redox effects can be the main

determinant of their structural radiation response, as demonstrated for CeO_2. Finally, materials with variability in both accessible structures and cation oxidation states, such as UO_3, can show strong coupling between irradiation-induced phase and valence modification.

6.1 Implications

Actinide and lanthanide oxides are most commonly exposed to swift heavy ions during the operation of nuclear reactors. Dioxides of thorium, uranium, and plutonium are the primary components of most nuclear fuels, while lanthanide sesquioxides are often added to these fuels as neutron absorbers to control reactivity. Lanthanide and transuranic actinide elements are also produced in nuclear fuel during reactor operation, as nuclear fission and decay products. Thus, the findings presented here regarding the unique crystalline-to-crystalline phase transformations and redox reactions that these material undergo in response to swift heavy ion irradiation have important implications for the design and performance of nuclear fuels. These behaviors are particularly relevant to advanced, high burn-up fuel cycles wherein fuels are exposed to very high fission fragment doses to improve the efficiency of nuclear energy generation [106].

The phase transformations observed in the trivalent lanthanide sesquioxides are likely to occur also in the related actinide sesquioxides, which have similar polymorphism. Indeed, ionizing radiation-induced phase transformations have previously been observed in Am_2O_3 and Cf_2O_3 [139–141]. The C-to-B transformation of *f*-block sesquioxides, reported in Chapter 3, corresponds to a ~10% densification of these materials. The accompanying volume change will have dramatic effects on the bulk structural integrity of any nuclear fuel or wasteform in which these transuranic waste materials were a component. Likewise, the unit cell expansion and microstrain that accompany defect formation and valence changes in the actinide dioxides will influence the performance and safety of nuclear fuels. Because the extent of these modifications

were shown to depend strongly on composition and grain size (due to compositional and microstructural variation in redox efficiency), consideration of irradiation-induced valence changes in the design of advanced nuclear fuels can yield improved radiation tolerance and longer fuel operating lifetimes. For example, the use of ThO_2 as a fuel, rather than UO_2, might ameliorate performance degradation associated with the nuclear fuel rim effect, which has been related to the formation of anion dislocation loop networks associated with redox-driven anion segregation (see Section 4.3 of this dissertation). Furthermore, doping of nuclear fuels with, for example, trivalent lanthanide cations could allow for both the control of reactivity (through neutron absorption) and reduction of valence-change driven, irradiation-induced structural modifications, given the demonstrated resistance of these cations to such changes in oxidation state. A significant impact of Ln_2O_3 doping on the radiation response of CeO_2 has been demonstrated by Tahara *et al*. [176]. Finally, the results presented here indicate that nanocrystalline oxides, which have been proposed as potential advanced nuclear fuel forms [252], may be unsuitable for use in this application. While such materials generally show exceptional tolerance of irradiation in the nuclear energy loss regime [210], they are shown in Chapter 4 to be highly susceptible to dimensional changes induced by irradiation in the electronic stopping regime due to an enhanced redox response to ionizing radiation typical of fission fragment exposure.

In addition to their importance to nuclear energy generations, many Ln_2O_3 materials find use in high-κ gate dielectrics [253,83] or as passivation layers for III-V compound semiconductors in metal oxide-semiconductor field-effect transistors (MOSFETs) [82]. The resistance of microelectronic device materials to damage by swift heavy ion irradiation (a property referred to as “radiation hardness” in electronics design communities) is of great

importance for the long-term operation of spacecraft, as high-energy cosmic rays are ubiquitous is space environments. Irradiation-induced defect accumulation in these materials will influence the electronic properties critical to their applications. For example, vacancies associated with Frenkel defects can act as mid-band energy levels for charge carriers, while disorder can increase ionic mobility, leading to ionic conduction and current leakage [254]. Irradiation-induced phase transformations could also lead to component failure due to dimensional changes, particularly in the case of epitaxial films in MOSFET devices. Thus, understanding of the atomic-scale processes that govern irradiation-induced structure modification in these materials is of use for assessing their radiation tolerance and designing components with minimal susceptibility to radiation-induced failure. The findings presented in Chapter 3 indicate a strong dependence of defect formation energetics, and therefore irradiation-induced defect concentration, on the ionic radius of the cation in Ln_2O_3 compounds. Thus, the substitution of proposed Pr_2O_3 or Gd_2O_3 dielectric materials in electronic devices [253,83,82] with Lu_2O_3, which has similar structural and electronic properties yet is relatively resistant to swift heavy ion irradiation damage due to its small cation, will greatly enhance the performance of such devices in spacecraft applications. In this way, radiation hardening of electronics can be improved through consideration of the processes through which dense electronic excitation induces modification of a materials structure and the energetics involved, as elucidated by the systematic studies described here.

In contrast to nuclear and spacecraft electronics applications, in which the minimization of irradiation-induced modification is typically desirable, ion beam processing applications of swift heavy ion irradiation benefit from a high susceptibility of materials to such modifications. Ion irradiation is often useful for the controlled introduction of defects and disorder to materials [70]. The irradiation-induced C-to-X phase transformation in Tm_2O_3 and Lu_2O_3, described in

Chapter 3, and pyrochlore-to-defect fluorite transformation in $Yb_2Sn_2O_7$ described in Chapter 5, are of particular interest in this respect. The C-to-X transformation involves the recovery of a novel, far-from-equilibrium phase to ambient conditions. The structure of the X-type phase is of particular interest due to its combination of cation sublattice ordering and anion sublattice disordering, as indicated by its sharp x-ray diffraction maxima and broad Raman modes, characteristic of amorphous phases of this compound. Such anion sublattice-specific disordering is attractive for oxygen ion conduction applications, as it suggests high oxygen mobility coupled with bulk thermomechanical stability due to cation sublattice crystallinity [255]. These properties, along with prior observation of high ionic conductivity of X-type La_2O_3 [118], make these materials potential candidates for applications in solid oxide fuel cells. The production of this phase demonstrates the utility of swift heavy ion beam processing for the controlled introduction of disorder to a material system, leading to the formation of metastable, far-from-equilibrium phases that cannot be obtained through conventional processing techniques.

In addition to nuclear, spacecraft electronics, and materials processing applications, basic research on the influence of swift heavy ion irradiation on the crystal chemistry of oxides is of interest from an astrophysical perspective. A significant portion of the interstellar medium is composed of silicate dust grains, likely of similar composition to olivine, $Mg_xFe_{2-x}SiO_4$ [256]. These solid oxides catalyze the formation of gas phase molecules from the interstellar medium through surface adsorption of individual atoms [257–260]. The production of H_2 in this manner results in the cooling and collapse of molecular clouds, driving the early stages of planet and star formation [257–260,61]. The adsorption of atoms to silicate surfaces depends strongly on the crystal chemistry of these solids such that, the irradiation-induced redox behavior studied in Chapter 4 will likely influence this behavior. Iron in olivine materials, for example, exhibits

several stable oxidation states in oxides, similar to the light actinides that undergo irradiation-induced redox modification. Additionally, interstellar dust grains absorb a substantial fraction of photons emitted from stars and emit in the far-infrared, mediating various photochemical processes in the interstellar medium [256,261]. The spectroscopic behavior of these materials will change with irradiation-induced redox modifications of cations, which influence the energies of electronic transitions. Thus, the ionizing radiation-induced redox effect presented in this dissertation might have broad implications for the understanding of astrophysical processes and the interpretation of associated spectroscopic data.

6.2 Future work

The findings reported here demonstrate the diversity of swift heavy ion irradiation-induced modifications to oxides, and their dramatic dependence of composition. Comparison of these results on the *f*-block oxides to those obtained from study of transition metal oxides, for example, is needed to determine whether the redox effect described here is a general feature of the radiation response of redox active materials or if it is instead particular to materials featuring *f*-electrons. Naguib and Kelly have reported irradiation-induced stoichiometry changes similar to those seen in UO_3 in a number of transition metal oxides [244], suggesting that the radiation response systematics described here are relevant to the behavior of other oxide systems. The observed dependence of the susceptibility of Ln_2O_3 materials to radiation damage on cation ionic radius is also likely a general feature of the radiation response of ionic-covalent compounds. Other materials systems, such as the fluorite-structured alkaline earth halides (*e.g.* CaF_2, SrF_2, and BaF_2) show similar proportionality between cation ionic radius and defect energies [262]. Again, further systematic work on such materials systems would be useful to extend the trends

reported here, particularly with respect to materials with nuclear energy or spacecraft applications.

The application of additional, complementary experimental techniques to the study of swift heavy ion irradiation effects in the materials systems described here could help to further elucidate the electronic and atomic modification mechanisms described. Thermochemical techniques, such as calorimetry, can directly probe the energetics of irradiation-induced phase transformations. This would make such an investigation of the irradiation-induced lanthanide sesquioxides phases useful to confirm the conclusions drawn in Chapter 3 of this dissertation. Thermochemical data on the new Tm_2O_3 and Lu_2O_3 X-type phases, for example, would complement a large existing body of data on the thermodynamics of equilibrium phases in this system [116]. Annealing studies, which provide information on the energetics of defect recovery, can also be useful for characterization of the dependence of defect formation on composition, as has been demonstrated for swift heavy ion irradiated CeO_2 and ThO_2 [263]. Total scattering experiments and pair-distribution function analysis can provide local structure information that is complementary to the Raman spectroscopy data described throughout this dissertation. In particular, these techniques may be useful for studying the local defect aggregation and resulting collective atomic rearrangements to which the irradiation induced C-to-B transformation of the lanthanide sesquioxides was attributed (Chapter 3). Additionally, these techniques could provide information on the specific structural distortions produced by point defects and cations of modified valence in fluorite-structured dioxides (Chapter 4). Finally, comparison of the results described here with those of ultrafast laser irradiations of the same materials would be interesting, as such irradiations deposit energy to materials through electronic excitation, similar

to swift heavy ion irradiation. Laser irradiation has been shown to induce C-to-B transformations in Gd_2O_3 identical to those described in Chapter 3 of this dissertation [264].

References

[1] N. Itoh, D.M. Duffy, S. Khakshouri, A.M. Stoneham, Making tracks: electronic excitation roles in forming swift heavy ion tracks. *J. Phys.: Condens. Matter* **21**, 474205 (2009).

[2] H. Bethe, Zur theorie des durchgangs schneller korpuskularstrahlen durch materie. *Ann. Phys.* **397**, 325 (1930).

[3] K. Schwartz, C. Trautmann, R. Neumann, Electronic excitations and heavy-ion-induced processes in ionic crystals. *Nucl. Instrum. Meth. B* **209**, 73 (2003).

[4] S. Klaumünzer, Thermal spike models for ion track physics: a critical examination. *Mat. Fys. Medd.* **52**, 293 (2006).

[5] D.M. Duffy, S.L. Daraszewicz, J. Mulroue, Modelling the effects of electronic excitations in ionic-covalent materials. *Nucl. Instrum. Meth. B* **277, 21** (2012).

[6] A.V. Lankin, I. V. Morozov, G.E. Norman, S.A. Pikuz, I.Y. Skobelev, Solid-density plasma nanochannel generated by a fast single ion in condensed matter. *Phys. Rev. E* **79**, 036407 (2009).

[7] G.E. Norman, S.V. Starikov, V.V. Stegailov, I.M. Saitov, P.A. Zhilyaev, Atomistic modeling of warm dense matter in the two-temperature state. *Contrib. to Plasma Phys.* **53**, 129 (2013).

[8] A. Rousse, C. Rischel, S. Fourmaux, I. Uschmann, S. Sebban, G. Grillon, P. Balcou, E. Förster, J.P. Geindre, P. Audebert, J.C. Gauthier, D. Hulin, Non-thermal melting in semiconductors measured at femtosecond resolution. *Nature* **410**, 65 (2001).

[9] N. Medvedev, Z. Li, B. Ziaja, Thermal and nonthermal melting of silicon under femtosecond x-ray irradiation. *Phys. Rev. B* **91**, 054113 (2015).

[10] K.H. Bennemann, Photoinduced phase transitions. *J. Phys.: Condens. Matter* **23**, 073202 (2011).

[11] J.-M. Costantini, F. Beuneu, D. Gourier, C. Trautmann, G. Calas, M. Toulemonde, Colour centre production in yttria-stabilized zirconia by swift charged particle irradiations. *J. Phys.: Condens. Matter* **16**, 3957 (2004).

[12] N.A. Medvedev, A.E. Volkov, K. Schwartz, C. Trautmann, Effect of spatial redistribution of valence holes on the formation of a defect halo of swift heavy-ion tracks in LiF. *Phys. Rev. B* **871**, 104103 (2013).

[13] A. Benyagoub, Mechanism of the monoclinic-to-tetragonal phase transition induced in zirconia and hafnia by swift heavy ions. *Phys. Rev. B* **72**, 094114 (2005).

[14] S. Hémon, V. Chailley, E. Dooryhée, C. Dufour, F. Gourbilleau, F. Levesque, E. Paumier, Phase transformation of polycrystalline Y_2O_3 under irradiation with swift heavy ions. *Nucl. Instrum. Meth. B* **122**, 563 (1997).

[15] M. Lang, R. Devanathan, M. Toulemonde, C. Trautmann, Advances in understanding of swift heavy-ion tracks in complex ceramics. *Curr. Opin. Solid State Mater. Sci.* **19**, 39 (2014).

[16] A. Meftah, F. Brisard, J.M. Costantini, E. Dooryhee, M. Hage-Ali, M. Hervieu, J.P. Stoquert, F. Studer, M. Toulemonde, Track formation in SiO_2 quartz and the thermal-spike mechanism. *Phys. Rev. B* **49**, 12457 (1994).
[17] J. Jensen, A. Dunlop, S. Della-Negra, Microscopic observations of metallic inclusions generated along the path of MeV clusters in CaF_2. *Nucl. Instrum. Meth. B* **146**, 399 (1998).
[18] C.L. Tracy, M. Lang, J.M. Pray, F. Zhang, D. Popov, C. Park, C. Trautmann, M. Bender, D. Severin, V.A. Skuratov, R.C. Ewing, Redox response of actinide materials to highly ionizing radiation. *Nat. Commun.* **6**, 6133 (2015).
[19] A. Hedler, S.L. Klaumünzer, W. Wesch, Amorphous silicon exhibits a glass transition. *Nat. Mater.* **3**, 804 (2004).
[20] C. Trautmann, S. Klaumünzer, H. Trinkaus, Effect of stress on track formation in amorphous iron boron alloy: ion tracks as elastic inclusions. *Phys. Rev. Lett.* **85**, 3648 (2000).
[21] J. Zhang, M. Lang, R.C. Ewing, R. Devanathan, W.J. Weber, M. Toulemonde, Nanoscale phase transitions under extreme conditions within an ion track. *J. Mater. Res.* **25**, 1344 (2011).
[22] M. Toulemonde, Defect creation by swift heavy ions: material modifications in the electronic stopping power regime. *Appl. Radiat. Isot.* **46**, 375 (1995).
[23] A. Barbu, A. Dunlop, D. Lesueur, R.S. Averback, Latent tracks do exist in metallic materials. *Europhys. Lett.* **15**, 37 (2007).
[24] A. Audouard, E. Balanzat, S. Bouffard, J.C. Jousset, A. Chamberod, A. Dunlop, D. Lesueur, G. Fuchs, R. Spohr, J. Vetter, L. Thomé, Evidence for amorphization of a metallic alloy by ion electronic energy loss. *Phys. Rev. Lett.* **65**, 875 (1990).
[25] A. Barbu, A. Dunlop, A. Hardouin Duparc, G. Jaskierowicz, N. Lorenzelli, Microstructural modifications induced by swift ions in the NiTi intermetallic compound. *Nucl. Instrum. Meth. B* **145**, 354 (1998).
[26] M. Ghidini, J.P. Nozières, D. Givord, M. Toulemonde, B. Gervais, Amorphization of rare earth-cobalt intermetallic alloys by swift heavy-ion irradiation. *J. Phys.: Condens. Matter* **8**, 8191 (1999).
[27] G. Sattonnay, M. Lahrichi, A. Benyagoub, J.M. Costantini, F. Garrido, L. Thomé, C. Trautmann, Structural modifications induced by swift heavy ions in cubic stabilized zirconia: an x-ray diffraction investigation *Nucl. Instrum. Meth. B* **257**, 476 (2007).
[28] G. Sattonnay, M. Lahrichi, M. Herbst-Ghysel, F. Garrido, L. Thomé, Stress field induced by swift heavy ion irradiation in cubic yttria stabilized zirconia. *J. Appl. Phys.* **101**, 103516 (2007).
[29] N. Ishikawa, Y. Chimi, O. Michikami, Y. Ohta, K. Ohhara, M. Lang, R. Neumann, Study of structural change in CeO_2 irradiated with high-energy ions by means of x-ray diffraction measurement. *Nucl. Instrum. Meth. B* **266**, 3033 (2008).
[30] Y. Tahara, B. Zhu, S. Kosugi, N. Ishikawa, Y. Okamoto, F. Hori, T. Matsui, A. Iwase, Study on effects of swift heavy ion irradiation on the crystal structure in CeO_2 doped with Gd_2O_3. *Nucl. Instrum. Meth. B* **269**, 886 (2011).
[31] C.L. Tracy, J.M Pray, M. Lang, D. Popov, C. Park, C. Trautmann, R.C. Ewing, Defect accumulation in ThO_2 irradiated with swift heavy ions. *Nucl. Instrum. Meth. B* **326**, 169 (2014).

[32] N. Ishikawa, T. Sonoda, Y. Okamoto, T. Sawabe, K. Takegahara, S. Kosugi, A. Iwase, X-ray study of radiation damage in UO_2 irradiated with high-energy heavy ions. *J. Nucl. Mater.* **419**, 392 (2011).
[33] K. Hayashi, H. Kikuchi, K. Fukuda, Radiation damage of UO_2 by high-energy heavy ions. *J. Nucl. Mater.* **248**, 191 (1997).
[34] J.F. Ziegler, M.D. Ziegler, J.P. Biersack, SRIM – The stopping and range of ions in matter (2010). *Nucl. Instrum. Meth. B* **268**, 1818 (2010).
[35] M. Lang, M. Toulemonde, J. Zhang, F. Zhang, C.L. Tracy, J. Lian, Z. Wang, W.J. Weber, D. Severin, M. Bender, C. Trautmann, R.C. Ewing, Swift heavy ion track formation in $Gd_2Zr_{2-x}Ti_xO_7$ pyrochlore: effect of electronic energy loss. *Nucl. Instrum. Meth. B* **336**, 102 (2014).
[36] M. Toulemonde, S. Bouffard, F. Studer, Swift heavy ions in insulating and conducting oxides: tracks and physical properties. *Nucl. Instrum. Meth. B* **91**, 108 (1994).
[37] F. Seitz, Radiation effects in solids. *Phys. Today* **5**, 6 (1952).
[38] C. Romano, Y. Danon, R. Block, J. Thompson, E. Blain, E. Bond, Fission fragment mass and energy distributions as a function of incident neutron energy measured in a lead slowing-down spectrometer. *Phys. Rev. C* **81**, 014607 (2010).
[39] T.S. Noggle, J.O. Stiegler, Electron microscope observations of fission fragment tracks in thin films of UO_2. *J. Appl. Phys.* **31**, 2199 (1960).
[40] D.A. Young, The discovery of solid-state nuclear tracks—A personal memoir from 1956-1959. *Radiat. Meas.* 44, 704 (2009).
[41] J.R. Macewan, R.L. Stoute, Annealing of irradiation-induced thermal conductivity changes in ThO_2-1.3 wt% UO_2. *J. Am. Ceram. Soc.* **52**, 160 (1969).
[42] K. Une, K. Nogita, S. Kashibe, M. Imamura, Microstructural change and its influence on fission gas release in high burnup UO_2 fuel. *J. Nucl. Mater.* **188**, 65 (1992).
[43] H. Matzke, J. Spino, Formation of the rim structure in high burnup fuel. *J. Nucl. Mater.* **248**, 170 (1997).
[44] R.L. Fleischer, P.B. Price, Tracks of charged particles in high polymers. *Science* **140**, 1221 (1963).
[45] K. Izui, F.E. Fujita, Electron microscopy study of fission fragment damage in molybdenite crystals. *J. Phys. Soc. Japan* **18**, 467 (1963)
[46] P.E. Caspar, Etching and enlarging of fission fragment tracks by atmospheric moisture. *Nature* **201**, 1203 (1964).
[47] P.B. Price, R.M. Walker, Observation of charged-particle tracks in solids. *J. Appl. Phys.* **33**, 3400 (1962).
[48] R.L. Fleischer, P.B. Price, R.M. Walker, Ion explosion spike mechanism for formation of charged-particle tracks in solids. *J. Appl. Phys.* **36**, 3645 (1965).
[49] E.C.H. Silk, R.S. Barnes, Examination of fission fragment tracks with an electron microscope. *Philos. Mag.* **4**, 970 (1959).
[50] P.B. Price, R.M. Walker, Fossil tracks of charged particles in mica and the age of minerals. *J. Geophys. Res.* **68**, 4847 (1963).
[51] R.L. Fleischer, Fission tracks in solids—production mechanisms and natural origins. *J. Mater. Sci.* **39**, 3901 (2004).
[52] T. Tagami, P.B. O'Sullivan, Fundamentals of fission-track thermochronology. *Rev. Mineral. Geochem.* **58**, 19 (2005).

[53] R.C. Ewing, A. Meldrum, L. Wang, S. Wang, Radiation-induced amorphization. *Rev. Mineral. Geochem.* **39**, 319 (2000).
[54] G.W. Clark, J. Earl, L. Kraushaar, J. Linsley, B.B. Rossi, F. Scherb, A.W. Scott, Cosmis-ray air showers at sea level. *Phys. Rev.* **122**, 637 (1961).
[55] J. Donnelly, A. Thompson, D. O'Sullivan, J. Daly, L. Drury, V. Domingo, K.-P. Wenzel, Actinide and ultra-heavy abundances in the local galactic cosmic rays: an analysis of the results from the LDEF ultra-heavy cosmic-ray experiment. *Astrophys. J.* **747**, 40 (2012).
[56] A.J. Westphal, P.B. Price, B.A. Weaver, V.G. Afanasiev, Evidence against stellar chromospheric origin of galactic cosmic rays. *Nature* **396**, 50 (1998).
[57] M. Maurette, P. Pellas, R.M. Walker, Cosmic-ray-induced particle tracks in a meteorite. *Nature* **204**, 821 (1964).
[58] R.L. Fleischer, P.B. Price, R.M. Walker, M. Maurette, G. Morgan, Tracks of heavy primary cosmic rays in meteorites. *J. Geophys. Res.* **72**, 355 (1957).
[59] P.B. Price, R.L. Fleischer, C.D. Moak, Identification of very heavy cosmic-ray tracks in meteorites. *Phys. Rev.* **167**, 277 (1968).
[60] P.B. Price, G. Gerbier, H.S. Park, M.H. Salamon, Systematics of annealing of tracks of relativistic nuclei in phosphate glass detectors. *Nucl. Instrum. Meth. B* **28**, 53 (1987).
[61] E.M. Bringa, S.O. Kucheyev, M.J. Loeffler, R.A. Baragiola, A.G.G.M. Tielens, Z.R. Dai, G. Graham, S. Bajt, J.P. Bradley, C.A. Dukes, T.E. Felter, D.F. Torres, W. van Breugel, Energetic processing of interstellar silicate grains by cosmic rays. *Astrophys. J.* **662**, 372 (2007).
[62] G. Szenes, V.K. Kovács, B. Pécz, V. Skuratov, The effect of heavy cosmic-ray ions on silicate grains in the interstellar dust. *Astrophys. J.* **708**, 288 (2010).
[63] L. Adams, Cosmic ray effects in microelectronics. *Microelectronics J.* **16**, 17 (1985).
[64] G.M. Comstock, R.L. Fleischer, W.R. Giard, H.R. Hart, G.E. Nichols, P.B. Price, Cosmic-ray tracks in plastics: the Apollo helmet dosimetry experiment. *Science* **172**, 154 (1971).
[65] H.A. Grunder, F.B. Selph, Heavy-ion accelerators. *Ann. Rev. Nucl. Sci.* **27**, 353 (1977).
[66] E. Akcöltekin, T. Peters, R. Meyer, A. Duvenbeck, M. Klusmann, I. Monnet, H. Lebius, M. Schleberger, Creation of multiple nanodots by single ions. *Nat. Nanotechnol.* **2**, 290 (2007).
[67] M.C. Ridgway, R. Giulian, D.J. Sprouster, P. Kluth, L.L. Araujo, D.J. Llewellyn, A.P. Byrne, F. Kremer, P.F.P. Fichtner, G. Rizza, H. Amekura, M. Toulemonde, Role of thermodynamics in the shape transformation of embedded metal nanoparticles induced by swift heavy-ion irradiation. *Phys. Rev. Lett.* **106**, 095505 (2011).
[68] I.P. Jain, G. Agarwal, Ion beam induced surface and interface engineering. *Surf. Sci. Rep.* **66**, 77 (2011).
[69] M.C. Ridgway, F. Djurabekova, K. Nordlund, Ion-solid interactions at the extremes of electronic energy loss: examples for amorphous semiconductors and embedded nanostructures. *Curr. Opin. Solid State Mater. Sci.* **19**, 29 (2015).
[70] S. Dhara, Formation, dynamics, and characterization of nanostructures by ion beam irradiation. *Crit. Rev. Solid State Mater. Sci.* **32**, 1 (2007).
[71] M. Jubera, J. Villarroel, A. García-Cabañes, M. Carrascosa, J. Olivares, F. Agullo-López, A. Méndez, J.B. Ramiro, Analysis and optimization of propagation losses in $LiNbO_3$ optical waveguides produced by swift heavy-ion irradiation. *Appl. Phys. B Lasers Opt.* **107**, 157 (2012).

[72] P. Kumaresan, S. Moorthy Babu, P.M. Anbarasan, Effect of irradiation of swift heavy ions on dyes-doped KDP crystals for laser applications. *J. Cryst. Growth* 310, 1999 (2008).
[73] A. García-Navarro, J. Olivares, G. García, F. Agulló-López, S. García-Blanco, C. Merchant, J.S. Aitchison, Fabrication of optical waveguides in KGW by swift heavy ion beam irradiation. *Nucl. Instrum. Meth. B* **249**, 177 (2006).
[74] S. Som, S. Dutta, V. Kumar, V. Kumar, H.C. Swart, S.K. Sharma, Swift heavy ion irradiation induced modification in structural, optical and luminescence properties of Y_2O_3:Tb^{3+} nanophosphor. *J. Lumin.* **146**, 162 (2014).
[75] R.C. Ewing, Safe management of actinides in the nuclear fuel cycle: role of mineralogy. *Comptes Rendus Geosci.* **343**, 219 (2011).
[76] M. Asou, J. Porta, Prospects for poisoning reactor cores of the future. *Nucl. Eng. Des.* **168**, 261 (1997).
[77] A. Sinha, B.P. Sharma, Development of dysprosium titanate based ceramics. *J. Am. Ceram. Soc.* **88**, 1064 (2005).
[78] V.D. Risovany, E.E. Varlashova, D.N. Suslov, Dysprosium titanate as an absorber material for control rods. *J. Nucl. Mater.* **281**, 84 (2000).
[79] A. Trovarelli, Catalytic properties of ceria and CeO_2-containing materials. *Catal. Rev. Sci. Eng.* **38**, 439 (1996).
[80] J.G. Nunan, H.J. Robota, M.J. Cohn, S.A. Bradley, Physicochemical properties of Ce-containing three-way catalysts and the effect of Ce on catalyst activity. *J. Catal.* **133**, 309 (1992).
[81] H.-J. Beie, A. Gnörich, Oxygen gas sensors based on CeO_2 thick and thin films. *Sensor. Actuator* **4**, 393 (1991).
[82] M. Hong, J. Kwo, A.R. Kortan, J.P. Mannaerts, A.M. Sergent, Epitaxial cubic gadolinium oxide as a dielectric for gallium arsenide passivation. *Science* **283**, 1897 (1999).
[83] H.J. Osten, J.P. Liu, H.J. Müssig, Band gap and band discontinuities at crystalline Pr_2O_3/Si (001) heterojunctions. *Appl. Phys. Lett.* **80**, 297 (2002).
[84] L. Zhou, Z. Gu, X. Liu, W. Yin, G. Tian, L. Yan, S. Jin, W. Ren, G. Xing, W. Li, X. Chang, Z. Hu, Y. Zhao, Size-tunable synthesis of lanthanide-doped Gd_2O_3 nanoparticles and their applications for optical and magnetic resonance imaging. *J. Mater. Chem.* **22**, 966 (2012).
[85] F. Druon, M. Velázquez, P. Veber, S. Janicot, O. Viraphong, G. Buşe, M.A. Ahmed, T. Graf, D. Rytz, P. Georges, Laser demonstration with highly doped Yb:Gd_2O_3 and Yb:Y_2O_3 crystals grown by an original flux method. *Opt. Lett.* **38**, 4146 (2013).
[86] A.A. Kaminskii, S.N. Bagaev, H.J. Eichler, K. Ueda, K. Takaichi, A. Shirakawa, H. Yagi, T. Yanagitani, H. Rhee, Observation of high-order Stokes and anti-Stokes $\chi^{(3)}$-generation in highly transparent laser-host Lu_2O_3 ceramics. *Laser Phys. Lett.* **3**, 310 (2006).
[87] A. Fukabori, V. Chani, K. Kamada, F. Moretti, A. Yoshikawa, Growth of Tm^{3+}-doped Y_2O_3, Sc_2O_3, and Lu_2O_3 crystals by the micropulling down technique and their optical and scintillation characteristics, *Crys. Growth Des.* **11**, 2404 (2011).
[88] C.R. Stanek, M.R. Levy, K.J. Mcclellan, B.P. Uberuaga, R.W. Grimes, Defect identification and compensation in rare earth oxide scintillators. *Nucl. Instrum. Meth. B* **266**, 2657 (2008).
[89] J.C. Krupa, High-energy optical absorption in *f*-compounds. *J. Solid State Chem.* **178**, 483 (2005).

[90] R.G. Haire, L. Eyring, Comparisons of the binary oxides. *Handbook on the Physics and Chemistry of Rare Earths Vol. 18 – Lanthanides/Actinides: Chemistry*, ed: K.A. Gschneider, L. Eyring, G.R. Choppin, G.R. Lander, Elsevier Science (1994).
[91] G. Adachi, N. Imanaka, The binary rare earth oxides. *Chem. Rev.* **98**, 1479 (1998).
[92] R.C. Ewing, W.J. Weber, J. Lian, Nuclear waste disposal—pyrochlore ($A_2B_2O_7$): nuclear waste form for the immobilization of plutonium and "minor" actinides. *J. Appl. Phys.* **95**, 5949 (2004).
[93] M. Lang, C.L. Tracy, R.I. Palomares, F. Zhang, D. Severin, M. Bender, C. Trautmann, C. Park, V.B. Prakapenka, V.A. Skuratov, R.C. Ewing, Characterization of ion-induced radiation effects in nuclear materials using synchrotron x-ray techniques. *J. Mater. Res.* **30**, 1366 (2015).
[94] D.N. Sah, U.K. Viswanathan, E. Ramadasan, K. Unnikrishnan, S. Anantharaman, Post irradiation examination of thermal reactor fuels. *J. Nucl. Mater.* **383**, 45 (2008).
[95] T. Fujino, T. Shiratori, N. Sato, K. Fukuda, K. Yamada, H. Serizawa, Post-irradiation examination of high burnup Mg doped UO_2 in comparison with undoped UO_2, Mg-Nb doped UO_2 and Ti doped UO_2. *J. Nucl. Mater.* **297**, 176 (2001).
[96] K. Tanaka, S. Miwa, S. Sekine, H. Yoshimochi, H. Obayashi, S. Koyama, Restructuring and redistribution of actinides in Am-MOX fuel during the first 24 h of irradiation. *J. Nucl. Mater.* **440**, 480 (2013).
[97] J. Noirot, L. Desgranges, J. Lamontagne, Detailed characterisations of high burn-up structures in oxide fuels. *J. Nucl. Mater.* **372**, 318 (2008).
[98] N. Nitani, K. Kuramoto, T. Yamashita, K. Ichise, K. Ono, Y. Nihei, Post-irradiation examination on particle dispersed rock-like oxide fuel. *J. Nucl. Mater.* **352**, 365 (2006).
[99] W.-Q. Shi, L.-Y. Yuan, C.-Z. Wang, L. Wang, L. Mei, C.-L. Xiao, L. Zhang, Z.-J. Li, Y.-L. Zhao, Z.-F. Chai, Exploring actinide materials through synchrotron radiation techniques. *Adv. Mater.* **26**, 7807 (2014).
[100] J. Rothe, S. Butorin, K. Dardenne, M.A. Denecke, B. Kienzler, M. Löble, V. Metz, A. Seibert, M. Steppert, T. Vitova, C. Walther, H. Geckeis, The INE-Beamline for actinide science at ANKA. *Rev. Sci. Instrum.* **83**, 043105 (2012).
[101] B. Brendebach, K. Dardenne, M.A. Denecke, J. Rothe, T. Vitova, New developments at the INE-Beamline for actinide research at ANKA. *Nucl. Instrum. Meth. A* 582, 80 (2007).
[102] P.L. Solari, S. Schlutig, H. Hermange, B. Sitaud, MARS, a new beamline for radioactive matter studies at SOLEIL. *J. Phys. Conf. Ser.* **190**, 012042 (2009).
[103] W. Matz, N. Schell, G. Bernhard, F. Prokert, T. Reich, J. Claußner, W. Oehme, R. Schlenk, S. Dienel, H. Funke, F. Eichhorn, M. Betzl, D. Pröhl, U. Strauch, G. Hüttig, H. Krug, W. Neumann, V. Brendler, P. Reichel, M.A. Denecke, H. Nitsche, ROBL – a CRG beamline for radiochemistry and materials research at the ESRF. *J. Synchrotron Radiat.* **6**, 1076 (1999).
[104] H. Konishi, A. Yokoya, H. Shiwaki, H. Motohashi, T. Makita, Y. Kashihara, S. Hashimoto, T. Harami, T.A. Sasaki, H. Maeta, H. Ohno, H. Maezawa, S. Asaoka, N. Kanaya, K. Ito, N. Usami, K. Kobayashi, Synchrotron radiation beamline to study radioactive materials at the Photon Factory. *Nucl. Instrum. Meth. A* **372**, 322 (1996).
[105] C. Mieszczynski, G. Kuri, C. Degueldre, M. Martin, J. Bertsch, C.N. Borca, D. Grolimund, Ch. Delafoy, E. Simoni, Irradiation effects and micro-structural changes in large grain uranium dioxide fuel investigated by micro-beam x-ray diffraction. *J. Nucl. Mater.* **444**, 274 (2014).

[106] C. Degueldre, J. Bertsch, G. Kuri, M. Martin, Nuclear fuel in generation II and III reactors: research issues related to high burn-up. *Energy Environ. Sci.* **4**, 1651 (2011).
[107] C. Degueldre, C. Mieszczynski, C. Borca, D. Grolimund, M. Martin, J. Bertsch, X-ray fluorescence and absorption analysis of krypton in irradiated nuclear fuel. *Nucl. Instrum. Meth. B* **336**, 116 (2014).
[108] G.E. Ice, E.D. Specht, Microbeam, timing and signal-resolved studies of nuclear materials with synchrotron X-ray sources. *J. Nucl. Mater.* **425**, 233 (2012).
[109] A. Jayaraman, Diamond anvil cell and high-pressure physical investigations. *Rev. Mod. Phys.* **55**, 65 (1983).
[110] A.P. Hammersley, S.O. Svensson, M. Hanfland, A.N. Fitch, D. Häusermann, Two-dimensional detector software: from real detector to idealised image or two-theta scan *High Press. Res.* **14**, 235 (1996).
[111] H.M. Rietveld, A profile refinement method for nuclear and magnetic structures. *J. Appl. Cryst.* **2**, 65 (1969).
[112] G. Williamson, W. Hall, X-ray line broadening from filed aluminium and wolfram. *Acta Metall.* **1**, 22 (1953).
[113] B.E. Warren, X-Ray determination of the structure of glass. *J. Am. Ceram. Soc.* **17**, 249 (1934).
[114] M. Lang, F.X. Zhang, R.C. Ewing, J. Lian, C. Trautmann, Z. Wang, Structural modifications of $Gd_2Zr_{2-x}Ti_xO_7$ pyrochlore induced by swift heavy ions: disordering and amorphization. *J. Mater. Res.* **24**, 1322 (2009).
[115] M. Durazzo, F.B.V. Oliveira, E.F. Urano de Carvalho, H.G. Riella, Phase studies in the UO_2–Gd_2O_3 system. *J. Nucl. Mater.* **400**, 183 (2010).
[116] M. Zinkevich, Thermodynamics of rare earth sesquioxides. *Prog. Mater. Sci.* **52**, 597 (2007).
[117] G. Chen, J.R. Peterson, Systematics of the phase behavior in lanthanide sesquioxides. *J. Alloys Comp.* **186**, 233 (2008).
[118] P. Aldebert, A.J. Dianoux, J.P. Traverse, Neutron scattering evidence for fast ionic oxygen diffusion in the high temperature phases of La_2O_3. *J. Phys.* **40**, 1005 (1979).
[119] J. Couture, A Rouanet, R. Verges, M. Foex, Etude a haute tempéreature des systémes formes par le sesquioxyde de lanthane et les sesquioxydes de lanthanides. I. diagrammes de phases (1400°C < *T* < *T* Liquide). *J. Solid State Chem.* **182**, 171 (1976).
[120] M. Rahm, N.V. Skorodumova, Phase stability of the rare-earth sesquioxides under pressure. *Phys. Rev. B* **80**, 104105 (2009).
[121] T. Atou, K. Kusaba, Y. Tsuchida, W. Utsumi, T. Yagi, Y. Syono, Reversible B-type-A-type transition of Sm_2O_3 under high pressure. *Mater. Res. Bull.* **24**, 1171 (1989).
[122] S. Jiang, J. Liu, C. Lin, L. Bai, W. Xiao, Y. Zhang, D. Zhang, X. Li, Y. Li, L. Tang, Pressure-induced phase transition in cubic Lu_2O_3. *J. Appl. Phys.* **108**, 083541 (2010).
[123] L. Bai, J. Liu, X. Li, S. Jiang, W. Xiao, Y. Li, L. Tang, Y. Zhang, D. Zhang, Pressure-induced phase transformations in cubic Gd_2O_3. *J. Appl. Phys.* **106**, 073507 (2009).
[124] S. Jiang, J. Liu, X. Li, L. Bai, W. Xiao, Y. Zhang, C. Lin, Y. Li, L. Tang, Phase transformation of Ho_2O_3 at high pressure. *J. Appl. Phys.* **110**, 013526 (2011).
[125] S. Jiang, J. Liu, C. Lin, L. Bai, Y. Zhang, X. Li, Y. Li, L. Tang, H. Wang, Structural transformations in cubic Dy_2O_3 at high pressures. *Solid State Commun.* **169**, 37 (2013).
[126] S. Jiang, J. Liu, C. Lin, X. Li, Y. Li, High-pressure x-ray diffraction and Raman spectroscopy of phase transitions in Sm_2O_3. *J. Appl. Phys.* **113**, 113502 (2013).

[127] J.O. Sawyer, B.G. Hyde, L. Eyring, Pressure and polymorphism in the rare earth sesquioxides. *Inorg. Chem.* **4**, 426 (1965).
[128] S. Hémon, A. Berthelot, Ch. Dufour, F. Gourbilleau, E Dooryhée, S. Bégin-Colin, E. Paumier. *Eur. Phys. J. B* **19**, 517 (2001).
[129] R.J. Gaboriaud, M. Jublot, F. Paumier, B. Lacroix, Phase transformations in Y_2O_3 thin films under swift Xe ions irradiation. *Nucl. Instrum. Meth. B* **310**, 6 (2013).
[130] M. Jublot, F. Paumier, F. Pailloux, B. Lacroix, E. Leau, P. Guérin, M. Marteau, M. Jaouen, R.J. Gaboriaud, D. Imhoff, Yttrium oxide thin films: influence of the oxygen vacancy network organization on the microstructure. *Thin Solid Films* **515**, 6385 (2007).
[131] M. Lang, F. Zhang, J. Zhang, C.L. Tracy, A.B. Cusick, J. VonEhr, Z. Chen, C. Trautmann, R.C. Ewing, Swift heavy ion-induced phase transformation in Gd_2O_3. *Nucl. Instrum. Meth. B* **326**, 121 (2014).
[132] M. Tang, P. Lu, J.A. Valdez, K.E. Sickafus, Heavy ion irradiation-induced phase transformation in polycrystalline Dy_2O_3. *Philos. Mag.* **86**, 1597 (2006).
[133] M. Tang, P. Lu, J.A. Valdez, K.E. Sickafus, Heavy ion irradiation effects in the rare-earth sesquioxide Dy_2O_3. *Nucl. Instrum. Meth.* B **250**, 142 (2006).
[134] M. Tang, J.A. Valdez, P. Lu, G.E. Gosnell, C.J. Wetteland, K.E. Sickafus, A cubic-to-monoclinic structural transformation in the sesquioxide Dy_2O_3 induced by ion irradiation. *J. Nucl. Mater.* **328**, 71 (2004).
[135] M. Tang, P. Lu, J.A. Valdez, K.E. Sickafus, Ion-irradiation-induced phase transformation in rare earth sesquioxides (Dy_2O_3, Er_2O_3, Lu_2O_3). *J. Appl. Phys.* **99**, 063514 (2006).
[136] B. Antic, A. Kremenovic, I. Draganic, Ph. Colomban, D. Vasiljevic-Radovic, J. Blanusa, M. Tadic, M. Mitric, Effects of O^{2+} ions beam irradiation on crystal structure of rare earth sesquioxides. *Appl. Surf. Sci.* **255**, 7601 (2009).
[137] T. Gouder, P. Oppeneer, F. Huber, F. Wastin, J. Rebizant, Photoemission study of the electronic structure of Am, AmN, AmSb, and Am_2O_3 films. *Phys. Rev. B* **72**, 115122 (2005).
[138] R.D. Baybarz, High-temperature phases, crystal structures and the melting points for several of the transplutonium sesquioxides. *J. Inorg. Nucl. Chem.* **35**, 4149 (1973).
[139] C. Hurtgen, J. Fuger, Self-irradiation effects in americium oxides. *Inorg. Nucl. Chem. Lett.* **13**, 179 (1977).
[140] J.C. Wallmann, A structural transformation of curium sesquioxides. *J. Inorg. Nucl. Chem.* **26**, 2053 (1964).
[141] W.C. Mosley, Self-radiation damage in curium-244 oxide and aluminate. *J. Am. Ceram. Soc.* **54**, 475 (1971).
[142] J. Rodríguez-Carvajal, Recent advances in magnetic structure determination by neutron powder diffraction. *Physica B* **192**, 55 (1993).
[143] J.-M. Costantini, C. Trautmann, L. Thomé, J. Jagielski, F. Beuneu, Swift heavy ion-induced swelling and damage in yttria-stabilized zirconia. *J. Appl. Phys.* **101**, 073501 (2007).
[144] D. Yan, P. Wu, S.P. Zhang, L. Liang, F. Yang, Y.L. Pei, S. Chen, Assignments of the Raman modes of monoclinic erbium oxide. J. *Appl. Phys.* **114**, 193502 (2013).
[145] J. Gouteron, D. Michel, A.M. Lejus, J. Zarembowitch, Raman spectra of lanthanide sesquioxide single crystals: correlation between A and B-type structures. *J. Solid State Chem.* **38**, 288 (1981).

[146] W.J. Weber, Models and mechanisms of irradiation-induced amorphization in ceramics. *Nucl. Instrum. Meth. B* **166-167**, 98 (2000).
[147] C. Le Luyer, A. García-Murillo, E. Bernstein, J. Mugnier, Waveguide Raman spectroscopy of sol-gel Gd_2O_3 thin films. *J. Raman Spectrosc.* **34**, 234 (2003).
[148] P. Aldebert, J.P. Traverse, Etude par diffraction neutronique des structures de haute temperature de La_2O_3 et Nd_2O_3. *Mater. Res. Bull.* **14**, 303 (1979).
[149] L. Kittiratanawasin, R. Smith, B.P. Uberuaga, K.E. Sickafus, A.R. Cleave, R.W. Grimes, Atomistic simulations of radiation induced defect formation in the Er_2O_3 sesquioxide. *Nucl. Instrum. Meth. B* **266**, 2691 (2008).
[150] A. Chroneos, M.R. Levy, C.R. Stanek, K. McClellan, R.W. Grimes, Intrinsic defect processes in bixbyite sesquioxides. *Phys. Status Solidi* **4**, 1213 (2007).
[151] B.G. Hyde, Crystallographic shear relations between the structure types α-UO_3, CaF_2, La_2O_3 and NaCl and a correlation of some lanthanide and actinide oxide structures. *Acta Cryst. A* **27**, 617 (1971).
[152] J.R. Rustad, Density functional calculations of the enthalpies of formation of rare-earth orthophosphates. *Am. Mineral.* **97**, 791 (2012) 791.
[153] Y. Li, N. Chen, J. Zhou, S. Song, L. Liu, Z. Yin, C. Cai, Effect of the oxygen concentration on the properties of Gd_2O_3 thin films. *J. Cryst. Growth* **265**, 548 (2004).
[154] L. Kittiratanawasin, R. Smith, B.P. Uberuaga, K.E.Sickafus, Radiation damage and evolution of radiation-induced defects in Er_2O_3 bixbyite. *J. Phys.: Cond. Matter* **21**, 115403 (2009).
[155] S.J. Zinkle, Microstructure of ion irradiated ceramic insulators. *Nucl. Instrum. Meth. B* **91**, 234 (1994).
[156] S. Zinkle, V. Skuratov, D. Hoelzer, On the conflicting roles of ionizing radiation in ceramics. *Nucl. Instrum. Meth. B* **191**, 758 (2002).
[157] B. Lacroix, F. Paumier, R.J. Gaboriaud, Crystal defects and related stress in Y_2O_3 thin films: origin, modeling, and consequence on the stability of the C-type structure. *Phys. Rev. B* **84**, 014104 (2011).
[158] R.J. Gaboriaud, B. Lacroix, F. Paumier, Ion irradiation-induced phase transformations in bixbyite-fluorite related oxides: the role of dislocation loop nucleation. *Nucl. Instrum. Meth. B* **277**, 18 (2012).
[159] A. Meftah, F. Brisard, J.M. Costantini, M. Hage-Ali, J.P. Stoquert, F. Studer, M. Toulemonde, Swift heavy ions in magnetic insulators: a damage-cross-section velocity effect. *Phys. Rev. B* **48**, 920 (1993).
[160] R. Shannon, Revised effective ionic radii and systematic studies of interatomic distances in halides and chalcogenides. *Acta Cryst. A* 32, 751 (1976).
[161] B. Wu, M. Zinkevich, F. Aldinger, D. Wen, L. Chen, Ab initio study on structure and phase transition of A- and B-type rare-earth sesquioxides Ln_2O_3 (Ln = La-Lu, Y, and Sc) based on density function theory. *J. Solid State Chem.* **180**, 3280 (2007).
[162] M.V. Ryzhkov, V.A. Gubanov, Y.A. Teterin, A.S. Baev, Electronic structure, chemical bonding and X-ray photoelectron spectra of light rare-earth oxides. *Z. Phys. B Condens. Matter* **59**, 7 (1985).
[163] B.M. Angelov, Lattice and binding energies of cubic lanthanide sesquioxides. *J. Phys. C Solid State* **15**, 239 (2000).
[164] E.H.P. Cordfunke, R.J.M. Konings, The enthalpies of formation of lanthanide compounds III. Ln_2O_3(cr) *Thermochim. Acta* **375**, 65 (2001).

[165] L. Pauling, The principles determining the structure of complex ionic crystals. *J. Am. Chem. Soc.* **51**, 1010 (1929) 1010.
[166] A. Benyagoub, F. Levesque, F. Couvreur, C. Gibert-Mougel, C. Dufour, E. Paumier, Evidence of a phase transition induced in zirconia by high energy heavy ions. *Appl. Phys. Lett.* **77**, 3197 (2000).
[167] A. Benyagoub, Phase transformations in oxides induced by swift heavy ions. *Nucl. Instrum. Meth. B* **245**, 225 (2006).
[168] B. Schuster, F. Fujara, B. Merk, R. Neumann, T. Seidl, C. Trautmann, Response behavior of ZrO_2 under swift heavy ion irradiation with and without external pressure. *Nucl. Instrum. Meth. B* **277**, 45 (2012).
[169] D.K. Smith, W. Newkirk, The crystal structure of baddeleyite (monoclinic ZrO_2) and its relation to the polymorphism of ZrO_2. *Acta Cryst.* **18**, 983 (1965).
[170] D. Simeone, G. Baldinozzi, D. Gosset, S. LeCaër, L. Mazerolles, Impact of radiation defects on the structural stability of pure zirconia. *Phys. Rev. B* **70**, 134116 (2004).
[171] X. Guo, Low temperature degradation mechanism of tetragonal zirconia ceramics in water: role of oxygen vacancies. *Solid State Ionics* **112**, 113 (1998).
[172] S. Shukla, S. Seal, Mechanisms of room temperature metastable tetragonal phase stabilisation in zirconia. *Int. Mater. Rev.* **50**, 45 (2005).
[173] J.-M. Costantini, F. Beuneu, K. Schwartz, C. Trautmann, Generation of colour centres in yttria-stabilized zirconia by heavy ion irradiations in the GeV range. *J. Phys.: Condens. Matter* **22**, 315402 (2010).
[174] M. Lang, F. Zhang, J. Zhang, J. Wang, B. Schuster, C. Trautmann, R. Neumann, U. Becker, R.C. Ewing, Nanoscale manipulation of the properties of solids at high pressure with relativistic heavy ions. *Nat. Mater.* **8**, 793 (2009).
[175] H. Ohno, A. Iwase, D. Matsumura, Y. Nishihata, J. Mizuki, N. Ishikawa, Y. Baba, N. Hirao, T. Sonoda, M. Kinoshita, Study on effects of swift heavy ion irradiation in cerium dioxide using synchrotron radiation x-ray absorption spectroscopy. *Nucl. Instrum. Meth. B* **266**, 3013 (2008).
[176] Y. Tahara, K. Shimizu, N. Ishikawa, Y. Okamoto, F. Hori, T. Matsui, A. Iwase, Study on effects of energetic ion irradiation in Gd_2O_3-doped CeO_2 by means of synchrotron radiation x-ray spectroscopy. *Nucl. Instrum. Meth. B* **277**, 53 (2012).
[177] C.A. Yablinsky, R. Devanathan, J. Pakarinen, J. Gan, D. Severin, C. Trautmann, T.R. Allen, Characterization of swift heavy ion irradiation damage in ceria. *J. Mater. Res.* **30**, 1473 (2015).
[178] S. Takaki, K. Yasuda, T. Yamamoto, S. Matsumura, N. Ishikawa, Atomic structure of ion tracks in ceria. *Nucl. Instrum. Meth. B* **326**, 140 (2014).
[179] K. Shimizu, S. Kosugi, Y. Tahara, K. Yasunaga, Y. Kaneta, N. Ishikawa, F. Hori, T. Matsui, A. Iwase, Change in magnetic properties induced by swift heavy ion irradiation in CeO_2. *Nucl. Instrum. Meth. B* **286**, 291 (2012).
[180] K. Hayashi, H. Kikuchi, K. Fukuda, Radiation damage of UO_2 implanted with 100 MeV iodine ions. *J. Alloys Comp.* **213-214**, 351 (1994).
[181] N. Nakae, T. Kirihara, S. Nasu, Irradiation induced volume change in UO_2. *J. Nucl. Mater.* **74**, 1 (1978).
[182] N. Nakae, A. Harada, T. Kirihara, S. Nasu, Irradiation induced lattice defects in UO_2. *J. Nucl. Mater.* **71**, 314 (1978).

[183] A. Iwase, H. Ohno, N. Ishikawa, Y. Baba, N. Hirao, T. Sonoda, M. Kinoshita, Study on the behavior of oxygen atoms in swift heavy ion irradiated CeO_2 by means of synchrotron radiation x-ray photoelectron spectroscopy. *Nucl. Instrum. Meth. B* **267**, 969 (2009).
[184] M.W. Blair, M.R. Levy, R.W. Grimes, B.P. Uberuaga, C. Jiang, J.A. Valdez, J.J. Williams, M. Tang, C.R. Stanek, K.E. Sickafus, Charge compensation in an irradiation-induced phase of δ-$Sc_4Zr_3O_{12}$. *J. Mater. Sci.* **44**, 4754 (2009).
[185] M. Ishimaru, Y. Hirotsu, M. Tang, J.A. Valdez, K.E. Sickafus, Ion-beam-induced phase transformations in δ-$Sc_4Zr_3O_{12}$. *J. Appl. Phys.* **102**, 063532 (2007).
[186] R.J. Finch, F.C. Hawthorne, R.C. Ewing, Structural relations among schoepite, metaschoepite and "dehydrated schoepite." *Can. Mineral.* **36**, 831 (1998).
[187] P.C. Burns, R.C. Ewing, A. Navrotsky, Nuclear fuel in a reactor accident. *Science* **335**, 1184 (2012).
[188] K. Syassen, DATLAB, version 1.29. MPI/FKF Stuttgart, Germany (2003).
[189] Y. Zhang, D.S. Aidhy, T. Varga, S. Moll, P.D. Edmondson, F. Namavar, K. Jin, C.N. Ostrouchov, W.J. Weber, The effect of electronic energy loss on irradiation-induced grain growth in nanocrystalline oxides. *Phys. Chem. Chem. Phys.* **16**, 8051 (2014).
[190] J.R. Walensky, R.L. Martin, J.W. Ziller, W.J. Evans, Importance of energy level matching for bonding in Th^{3+}-Am^{3+} actinide metallocene amidinates, $(C_5Me_5)_2[^iPrNC(Me)N^iPr]An$. *Inorg. Chem.* **49**, 10007 (2010).
[191] V.G. Keramidas, W.B. White, Raman spectra of oxides with the fluorite structure. *J. Chem. Phys.* **59**, 1561 (1973).
[192] G. Guimbretière, L. Desgranges, A. Canizarès, G. Carlot, R. Caraballo, C. Jégou, F. Duval, N. Raimboux, M.R. Ammar, P. Simon, Determination of in-depth damaged profile by Raman line scan in a pre-cut He^{2+} irradiated UO_2. *Appl. Phys. Lett.* **100**, 251914 (2012).
[193] T. Livneh, E. Sterer, Effect of pressure on the resonant multiphonon Raman scattering in UO_2. *Phys. Rev. B* **73**, 085118 (2006).
[194] P.R. Graves, Raman microprobe spectroscopy of uranium dioxide single crystals and ion implanted polycrystals. *Appl. Spectrosc.* **44**, 1665 (1990).
[195] S. Skanthakumar, L. Soderholm, Oxidation state of Ce in $Pb_2Sr_2Ce_{1-x}Ca_xCu_3O_8$. *Phys. Rev. B* **53**, 920 (1996).
[196] S. Tsunekawa, K. Ishikawa, Z.-Q. Li, Y. Kawazoe, A. Kasuya, Origin of anomalous lattice expansion in oxide nanoparticles. *Phys. Rev. Lett.* **85**, 3440 (2000).
[197] S.R. Bishop, D. Marrocchelli, C. Chatzichristodoulou, N.H. Perry, M.B. Mogensen, H.L. Tuller, E.D. Wachsman, Chemical expansion: implications for electrochemical energy storage and conversion devices. *Annu. Rev. Mater. Res.* **44**, 205 (2014).
[198] K. Yasuda, M. Etoh, K. Sawada, T. Yamamoto, K. Yasunaga, S. Matsumura, N. Ishikawa, Defect formation and accumulation in CeO_2 irradiated with swift heavy ions. *Nucl. Instrum. Meth. B* **314**, 185 (2013).
[199] K. Yasunaga, K. Yasuda, S. Matsumura, T. Sonoda, Electron energy-dependent formation of dislocation loops in CeO_2. *Nucl. Instrum. Meth. B* **266**, 2877 (2008).
[200] K. Yasunaga, K. Yasuda, S. Matsumura, T. Sonoda, Nucleation and growth of defect clusters in CeO_2 irradiated with electrons. *Nucl. Instrum. Meth. B* **250**, 114 (2006).
[201] M. Kinoshita, K. Yasunaga, T. Sonoda, A. Iwase, N. Ishikawa, M. Sataka, K. Yasuda, S. Matsumura, H.Y. Geng, T. Ichinomiya, Y. Chen, Y. Kaneta, M. Iwasawa, T. Ohnuma, Y.

Nishiura, J. Nakamura, Hj. Matzke, Recovery and restructuring induced by fission energy ions in high burnup nuclear fuel. *Nucl. Instrum. Meth. B* **267**, 960 (2009).
[202] T. Ichinomiya, B.P. Uberuaga, K.E. Sickafus, Y. Nishiura, M. Itakura, Y. Chen, Y. Kaneta, M. Kinoshita, Temperature accelerated dynamics study of migration process of oxygen defects in UO_2. *J. Nucl. Mater.* **384**, 315 (2009).
[203] J. Jensen, A. Dunlop, S. Della-Negra, Tracks induced in CaF_2 by MeV cluster irradiation *Nucl. Instrum. Meth. B* **141**, 753 (1998).
[204] E. Johnson, L.T. Chadderton, Anion voidage and the void superlattice in electron irradiated CaF_2. *Radiat. Eff.* **79**, 183 (1983).
[205] S. Abu Saleh, Y. Eyal, Morphologies of latent and etched heavy-ion tracks in {111} CaF_2. *Philos. Mag.* **87**, 1 (2007).
[206] S.D. Berger, I.G. Salisbury, R.H. Milne, D. Imeson, C.J. Humphreys, Electron energy-loss spectroscopy studies of nanometre-scale structures in alumina produced by intense electron-beam irradiation. *Philos. Mag. B* **55**, 341 (1987).
[207] A. Kabir, A. Meftah, J.P. Stoquert, M. Toulemonde, I. Monnet, M. Izerrouken, Structural disorder in sapphire induced by 90.3 MeV xenon ions. *Nucl. Instrum. Meth. B* **268**, 3195 (2010).
[208] A. Vailionis, E.G. Gamaly, V. Mizeikis, W. Yang, A. V Rode, S. Juodkazis, Evidence of superdense aluminium synthesized by ultrafast microexplosion. *Nat. Commun.* **2**, 445 (2011).
[209] S. Zec, S. Bošković, B. Kaluđerović, Ž. Bogdanov, N. Popović, Chemical reduction of nanocrystalline CeO_2. *Ceram. Int.* **35**, 195 (2009).
[210] X.-M. Bai, A.F. Voter, R.G. Hoagland, M. Nastasi, B.P. Uberuaga, Efficient annealing of radiation damage near grain boundaries via interstitial emission. *Science* **327**, 1631 (2010).
[211] K. Merkle, Fission-fragment tracks in metal and oxide films. *Phys. Rev. Lett.* **9**, 150 (1962).
[212] A. Berthelot, S. Hémon, F. Gourbilleau, C. Dufour, B. Domengès, E. Paumier, Behaviour of a nanometric SnO_2 powder under swift heavy-ion irradiation: from sputtering to splitting. *Philos. Mag.* A **80**, 2257 (2000).
[213] S. Hémon, Ch. Dufour, F. Gourbilleau, E. Paumier, E. Dooryhée, S. Bégin-Colin. Influence of the grain size: yttrium oxide irradiated with swift heavy ions. *Nucl. Instrum. Meth. B* 146, 443 (1998).
[214] S. Moll, L. Thomé, L. Vincent, F. Garrido, G. Sattonnay, T. Thomé, J. Jagielski, J.M. Costantini, Damage induced by electronic excitation in ion-irradiated yttria-stabilized zirconia. *J. Appl. Phys.* **105**, 023512 (2009).
[215] P.C. Burns, U^{6+} minerals and inorganic compounds: insights into an expanded structural hierarchy of crystal structures. *Can. Mineral.* **43**, 1839 (2005).
[216] F. Farges, C.W. Ponader, G. Calas, G.E. Brown, Structural environments of incompatible elements in silicate glass/melt systems: II. U^{IV}, U^{V}, and U^{VI}. *Geochim. Cosmochim. Acta* **56**, 4205 (2000).
[217] P.M. Bertsch, D.B. Hunter, S.R. Sutton, S. Bajt, M.L. Rivers, In situ chemical speciation of uranium in soils and sediments by micro x-ray absorption spectroscopy. *Environ. Sci. Technol.* **28**, 980 (1994).
[218] A. Rey, S. Utsunomiya, J. Giménez, I. Casas, J. de Pablo, R.C. Ewing, Stability of uranium (VI) peroxide hydrates under ionizing radiation. *Am. Mineral.* **94**, 229 (2009).

[219] R. Sureda, I. Casas, J. Giménez, J. de Pablo, J. Quiñones, J. Zhang, R.C. Ewing, Effects of ionizing radiation and temperature on uranyl silicates: soddyite $(UO_2)_2(SiO_4)(H_2O)_2$ and uranophane $Ca(UO_2)_2(SiO_3OH)_2{\bullet}5H_2O$. *Environ. Sci. Technol.* **45**, 2510 (2011).
[220] S.R. Bishop, T. Nakamura, K. Amezawa, Chemically-induced expansion of $Zr_{0.2}Ce_{0.8}O_{2-\delta}$. *Solid State Ionics* **261**, 1 (2014).
[221] J.M. Haschke, T.H. Allen, L.A. Morales, Reaction of plutonium dioxide with water: formation and properties of PuO_{2+x}. *Science* **287**, 285 (2000).
[222] Hj. Matzke, P.G. Lucuta, T. Wiss, Swift heavy ion and fission damage effects in UO_2. *Nucl. Instrum. Meth. B* **166-167**, 920 (2000).
[223] T. Wiss, Hj. Matzke, C. Trautmann, M. Toulemonde, S. Klaumünzer, Radiation damage in UO_2 by swift heavy ions. *Nucl. Instrum. Meth. B* **122**, 583 (1997).
[224] T. Sonoda, M. Kinoshita, N. Ishikawa, M. Sataka, Y. Chimi, N. Okubo, A. Iwase, K. Yasunaga, Clarification of the properties and accumulation effects of ion tracks in CeO_2. *Nucl. Instrum. Meth. B* **266**, 2882 (2008).
[225] T. Sonoda, M. Kinoshita, Y. Chimi, N. Ishikawa, M. Sataka, A. Iwase, Electronic excitation effects in CeO_2 under irradiations with high-energy ions of typical fission products. *Nucl. Instrum. Meth. B* **250**, 254 (2006).
[226] T. Sonoda, M. Kinoshita, N. Ishikawa, M. Sataka, A. Iwase, K. Yasunaga, Clarification of high density electronic excitation effects on the microstructural evolution in UO_2 *Nucl. Instrum. Meth. B* **268**, 3277 (2010).
[227] K. Shiiyama, T. Yamamoto, T. Takahashi, A. Guglielmetti, A. Chartier, K. Yasuda, S. Matsumura, K. Yasunaga, C. Meis, Molecular dynamics simulations of oxygen Frenkel pairs in cerium dioxide. *Nucl. Instrum. Meth. B* **268**, 2980 (2010).
[228] N. Ishikawa, T. Sonoda, T. Sawabe, H. Sugai, M. Sataka, Electronic stopping power dependence of ion-track size in UO_2 irradiated with heavy ions in the energy range of ~1 MeV/u. *Nucl. Instrum. Meth. B* **314**, 180 (2013).
[229] H.Y. Xiao, Y. Zhang, W.J. Weber, Stability and migration of charged oxygen interstitials in ThO_2 and CeO_2. *Acta Mater.* **61** 7639 (2013).
[230] W.J. Weber, R.C. Ewing, C.R.A Catlow, T. Diaz de al Rubia, L.W. Hobbs, C. Kinoshita, Hj. Matzke, A.T. Motta, M. Nastasi, E.K.H. Salje, E.R. Vance, S.J. Zinkle, Radiation effects in crystalline ceramics for the immobilization of high-level nuclear waste and plutonium. *J. Mater. Res.* **13**, 1434 (1998).
[231] S. Lutique, D. Staicu. R.J.M. Konings, V.V. Rondinella, J. Somers, T. Wiss, Zirconate pyrochlore as a transmutation target: thermal behaviour and radiation resistance against fission fragment impact. *J. Nucl. Mater.* **319**, 59 (2003).
[232] S.X. Wang, B. Begg, L.M. Wang, R.C. Ewing, W.J. Weber, K.V Govidan Kutty, Radiation stability of gadolinium zirconate: a waste form for plutonium disposition. *J. Mater. Res.* **14**, 4470 (1999).
[233] M.A Subramanian, G. Aravamudan, G.V. Subba Rao, Oxide pyrochlores–a review. *Prog. Solid State Chem.* **15**, 55 (1983).
[234] B.C. Chakoumakos, Systematics of the pyrochlore structure type, ideal $A_2B_2X_6Y$. *J. Solid State Chem.* **53**, 120 (1984).
[235] A.V. Shlyakhtina, L.G. Shcherbakova, Polymorphism and high-temperature conductivity of $Ln_2M_2O_7$ (Ln = Sm-Lu; M = Ti, Zr, Hf) pyrochlores. *Solid State Ionics* **192**, 200 (2011).

[236] R.C. Ewing, J. Lian, L.M. Wang, Ion beam-induced amorphization of the pyrochlore structure-type: a review. *Mat. Res. Soc. Proc.* **792**, 37 (2003).
[237] K.E. Sickafus, L. Minervini, R.W. Grimes, J.A. Valdez, M. Ishimaru, F. Li, K.J. McClellan, T. Hartmann, Radiation tolerance of complex oxides. *Science* **289**, 748 (2000).
[238] M. Lang, J. Lian, J. Zhang, F. Zhang, W.J. Weber, C. Trautmann, R.C. Ewing, Single-ion tracks in $Gd_2Zr_{2-x}Ti_xO7$ pyrochlores irradiated with swift heavy ions. *Phys. Rev. B* **79**, 224105 (2009).
[239] G. Sattonnay, S. Moll, L. Thomé, C. Legros, A. Calvo, M. Herbst-Ghysel, C. Decorse, I. Monnet, Effect of composition on the behavior of pyrochlores irradiated with swift heavy ions. *Nucl. Instrum. Meth. B* **272**, 261 (2012).
[240] G. Sattonnay, C. Grygiel, I. Monnet, C. Legros, M. Herbst-Ghysel, L. Thomé, Phenomenological model for the formation of heterogeneous tracks in pyrochlores irradiated with swift heavy ions. *Acta Mater.* **60**, 22 (2012).
[241] K.E. Sickafus, R.W. Grimes, J.A. Valdez, A. Cleave, M. Tang, M. Ishimaru, S.M. Corish, C.R. Stanek, B.P. Uberuaga, Radiation-induced amorphization resistance and radiation tolerance in structurally related oxides. *Nat. Mater.* **6**, 217 (2007).
[242] J. Lian, K.B. Helean, B.J. Kennedy, L.M. Wang, A. Navrotsky, R.C. Ewing, Effect of structure and thermodynamic stability on the response of lanthanide stannate pyrochlores to ion beam irradiation. *J. Phys. Chem. B* **110**, 2343 (2006).
[243] W. Panero, L. Stixrude, R.C. Ewing, First-principles calculation of defect-formation energies in the $Y_2(Ti,Sn,Zr)_2O_7$ pyrochlore. *Phys. Rev. B* **70**, 0541100 (2004).
[244] H.M. Naguib, R. Kelly, Criteria for bombardment-induced structural changes in non-metallic solids. *Radiat. Eff.* **25**, 1(1975).
[245] R.K. Eby, R.C. Ewing, R.C. Birtcher, The amorphization of complex silicates by ion-beam irradiation. *J. Mater. Res.* **7**, 3080 (1992).
[246] K. Trachenko, J.M. Pruneda, E. Artacho, M.T. Dove, How the nature of the chemical bond governs resistance to amorphization by radiation damage. *Phys. Rev. B* **71**, 184104 (2005).
[247] K. Trachenko, Understanding resistance to amorphization by radiation damage. *J. Phys.: Condens. Matter* **16**, 1491 (2004).
[248] M.T. Vandenborre, E. Husson, J.P. Chatry, D. Michel, Rare-earth titanates and stannates of pyrochlore structure; vibrational spectra and force fields. *J. Raman Spectrosc.* **14**, 63 (1983).
[249] M.L. Sanjuán, C. Guglieri, S. Díaz-Moreno, G. Aquilanti, A.F. Fuentes, L. Olivi, J. Chaboy, Raman and x-ray absorption spectroscopy study of the phase evolution induced by mechanical milling and thermal treatments in $R_2Ti_2O_7$ pyrochlores. *Phys. Rev. B* **84**, 104207 (2011).
[250] M. Lang, J. Lian, F. Zhang, B.W.H. Hendriks, C. Trautmann, R. Neumann, R.C. Ewing, Fission tracks simulated by swift heavy ions at crustal pressures and temperatures. *Earth Planet. Sci. Lett.* **274**, 355 (2008).
[251] R.E. Sykora, P.E. Raison, R.G. Haire, Self-irradiation induced structural changes in the transplutonium pyrochlores $An_2Zr_2O_7$ (An = Am, Cf). *J. Solid State Chem.* **178**, 578 (2005).
[252] J. Spino, H. Santa Cruz, R. Jovani-Abril, R. Birtcher, C. Ferrero, Bulk-nanocrystalline oxide nuclear fuels – An innovative material option for increasing fission gas retention, plasticity and radiation-tolerance. *J. Nucl. Mater.* **422**, 27 (2012).

[253] J. Kwo, M. Hong, A.R. Kortan, K.L. Queeney, Y.J. Chabal, R.L. Opila Jr., D.A. Muller, S.N.G. Chu, B.J. Sapjeta, T.S. Lay, J.P. Mannaerts, T. Boone, H.W. Krautter, J.J. Krajewski, A.M. Sergnt, J.M. Rosamilia, Properties of high κ gate dielectrics Gd_2O_3 and Y_2O_3 for Si. *J. Appl. Phys.* **89**, 3920 (2001).
[254] M. Li, M.J. Pietrowski, R.A. De Souza, H. Zhang, I.M. Reaney, S.N. Cook, J.A. Kilner, D.C. Sinclair, A family of oxide ion conductors based on the ferroelectric perovskite $Na_{0.5}Bi_{0.5}TiO_3$. *Nat. Mater.* **13**, 31 (2014).
[255] S. Hull, Superionics: crystal structures and conduction processes. *Rep. Prog. Phys.* **67**, 1233 (2004).
[256] B.T. Draine, Interstellar dust grains. Annu. Rev. Astron. Astrophys. **41**, 241 (2003).
[257] D. Hollenbach, E.E. Salpeter, Surface recombination of hydrogen molecules. *Astrophys. J.* **163**, 155 (1971).
[258] O. Biham, I. Furman, N. Katz, V. Pirronello, G. Vidali, H_2 formation on interstellar grains in different physical regimes. *Mon. Not. R. Astron. Soc.* **196**, 869 (1998).
[259] S. Cazaux, A.G.G.M. Tielens, Molecular hydrogen formation in the interstellar medium. *Astrophys. J.* **575**, 29 (2002).
[260] N. Katz, I. Furman, O. Biham, V. Pirronello, G. Vidali, Molecular hydrogen formation on astrophysically relevant surfaces. *Astrophys. J.* **522**, 305 (1999).
[261] B.T. Draine, A.A. Fraisse, Polarized far-infrared and submillimeter emission from interstellar dust. *Astrophys. J.* **696**, 1 (2008).
[262] C.R.A. Catlow, M.J. Norgett, Shell model calculations of the energies of formation of point defects in alkaline earth fluorides. *J. Phys. C: Solid State Phys.* **6**, 1325 (1973).
[263] R.I. Palomares, C.L. Tracy, F. Zhang, C. Park, D. Popov, C. Trautmann, R.C. Ewing, M. Lang, *In situ* defect annealing of swift heavy ion irradiated CeO_2 and ThO_2 using synchrotron x-ray diffraction and a hydrothermal diamond anvil cell. *J. Appl. Cryst.* **48**, 711 (2015).
[264] D.R. Rittman, C.L. Tracy, A.B. Cusick, M.J. Abere, B. Torralva, R.C. Ewing, S.M. Yalisove, Ultrafast laser and swift heavy ion irradiation: response of Gd_2O_3 and ZrO_2 to intense electronic excitation. *Appl. Phys. Lett.* **106**, 171914 (2015).